
Ultrafast Dynamics on Nanostructures in Strong Fields

Philipp Rupp



München 2019

Ultrafast Dynamics on Nanostructures in Strong Fields

Philipp Rupp

Dissertation
an der Fakultät für Physik
der Ludwig-Maximilians-Universität
München

vorgelegt von
Philipp Rupp
aus Aalen

München, den 18. Januar 2019

Erstgutachter: Prof. Dr. Matthias F. Kling
Zweitgutachter: Prof. Dr. Francesca Calegari
Tag der mündlichen Prüfung: 25. März 2019

Zusammenfassung

Die Wechselwirkung zwischen Licht und Materie bestimmt in unserem Alltag viele fundamentale Vorgänge. Die für dieses Phänomen verantwortlichen physikalischen Grundlagen helfen dabei, Moleküleigenschaften, chemische Reaktionen und biologische Abläufe nicht nur besser zu verstehen, sondern auch zu kontrollieren. Um die ultraschnellen Ladungsbewegungen im Femtosekundenbereich zu untersuchen, werden in dieser Arbeit Wenig-Zyklen-Pulse benutzt, die Intensitäten im Starkfeldregime erreichen. Alle beschriebenen Experimente untersuchen Nanostrukturen, die Laserfelder auf Längenskalen verändern, die kleiner als die Wellenlänge sind. Dazu gehören beispielsweise die Modifikation der elektrischen Feldverteilung und die Erhöhung der Feldstärken.

Kugelförmige Nanopartikel werden verwendet, um das einfallende Laserlicht an ausgewählten Stellen auf der Teilchenoberfläche zu konzentrieren, wodurch dort laserinduzierte Dissoziationen ausgelöst werden. Im Anschluss agieren die dabei herausgelösten Protonen als Testteilchen der so erzeugten inhomogenen Oberflächenladungen. Um diese Protonen gemeinsam mit den ionisierten Nanoteilchen zu detektieren, wird ein neuartiger experimenteller Aufbau (nanoTRIMS) verwendet. Mithilfe numerischer Simulationen wird ein einfaches Modell präsentiert, das die gemessenen Protonenimpulse mit den charakteristischen Oberflächenladungsverteilungen verknüpft. Diese spezielle Verknüpfung gilt voraussichtlich auch für komplexere Strukturen und könnte zukünftig als Hilfsmittel dienen, um zeitabhängige Reaktionen von Oberflächenadsorbaten zu untersuchen.

Der zweite Teil der Arbeit behandelt die Plasmaexpansion von Nanoteilchen, die mit Starkfeld-Lasern bestrahlt werden. Nach der Plasmaerzeugung entwickelt sich die Dichte der Elektronen und Ionen nach einer bestimmten Dynamik. Die Untersuchung der radialen Plasmadichte erfolgt mittels Streuung von Röntgenpulsen aus einem Freielektronen-Laser. Anschließend erfolgt ein Vergleich der gemessenen Dichte mit theoretischen Vorhersagen. Die Ergebnisse bestätigen die Annahme, dass der Abtragungs- und der Ausdehnungsprozess der runden Nanoteilchen von den äußeren Schichten ausgeht und später in den inneren Kern vordringt. Mithilfe der vorliegenden Studie lassen sich Fragen zu fundamentalen Plasmamodellen beantworten, die nicht nur in der Starkfeldphysik, sondern auch in technischen Anwendungen, in der Fusionsphysik und in der Astrophysik Verwendung finden.

Ein aus 60 Kohlenstoffatomen bestehendes Molekül – das Buckminsterfulleren – ist die kleinste in dieser Arbeit untersuchte Nanostruktur. Aufgrund des geringen Durchmessers von nur 7 Ångström laufen die Elektronenbewegungen im C₆₀-Molekül im Attosekundenbereich ab. So kann Licht im extrem ultravioletten Spektrum eine gemeinsame Schwingung

der Valenzelektronen in C_{60} mit einer Periodendauer von ungefähr 210 Attosekunden anregen. Darüber hinaus interagieren die emittierten Photoelektronen mit den plasmonischen Nahfeldern, die von den Wenig-Zyklen-Pulsen erzeugt werden. In einem Anregungs-Abfrage-Experiment wird die Attosekunden-Verzögerung bei der Photoionisation gemessen und mit Monte-Carlo-Simulationen verglichen, die auf Ergebnissen aus Dichtefunktionaltheorie Rechnungen aufbauen.

Im Rahmen dieser Arbeit wird Licht untersucht, das mit nanometergroßen Strukturen in Wechselwirkung steht und diese Systeme ionisiert. Die Auflösung der nachfolgenden ultraschnellen Dynamik mithilfe von Femtosekunden-Laserpulsen erweitert den aktuellen Kenntnisstand dieses Mehrkörperprozesses und regt weitere zukünftige Experimente auf diesem Gebiet an.

Abstract

Light-matter interaction is a fundamental process governing many aspects of our daily life. The physics behind this phenomenon helps to understand and ultimately control molecular properties, chemical reactions and biological mechanisms. In order to investigate ultrafast motions of charges on femtosecond scales, this work utilizes few-cycle laser pulses with intensities in the strong-field regime. All presented experiments rely on nanostructures with the ability to alter laser fields on sub-wavelength dimensions, such as the modification of the electric field distribution and the enhancement of the field strengths.

Here, spherical nanoparticles are exploited to concentrate the incoming laser fields to selective regions on the particle surface, which triggers laser-induced dissociation processes. Subsequently, the released protons serve as a probe of the inhomogeneous surface charges. In order to detect these probing protons in coincidence with ionized nanoparticles, a novel detection scheme (nanoTRIMS) is introduced. With the help of numerical simulations, a simple model is presented that links the final proton momenta to the characteristic surface charge distribution. This prototypical relation is expected to hold for more complex structures and may also serve as a tool to investigate time-dependent reactions of surface adsorbates.

The second part of this thesis covers the plasma expansion of nanoparticles irradiated by strong-field laser pulses. After the plasma generation, the electron and ion density follows a specific temporal evolution. The radial plasma density is probed by x-ray free-electron laser pulses and compared to theoretical predictions. The results confirm that the ablation and expansion of the spherical nanoparticle starts from the outer shell and later penetrates the inner core layers. This study answers questions about fundamental plasma models that are used not only in the scope of strong-field physics but also for technical applications, fusion physics and astrophysical subjects.

The smallest nanostructure presented in the current work is the buckminsterfullerene which is a molecule consisting of 60 carbon atoms. Due to its small diameter of 7 ångströms, the electron motions in this C_{60} molecule occur on timescales of attoseconds. Light in the extreme ultraviolet spectral range excites a collective valence electron motion in C_{60} with a period of around 210 attoseconds. Furthermore, the emitted photoelectrons interact with plasmonic near-fields induced by few-cycle laser pulses. The photoionization delay of the electrons is retrieved by an attosecond streaking experiment and compared to Monte-Carlo simulations utilizing density functional theory.

This thesis investigates instances of light interfering with nanosized structures and ionizing these systems. The subsequent ultrafast dynamics are resolved by femtosecond

laser pulses, which improves our knowledge of the many-body process and can stimulate future experiments in this field.

Table of Contents

Zusammenfassung	v
Abstract	vii
1 Introduction	1
2 Theory	7
2.1 Ultrashort laser pulses	7
2.2 Ionization mechanism	9
2.3 Attosecond Streaking	11
2.4 Photoemission time delay	12
2.4.1 Time delays in atoms	13
2.4.2 Time delays in molecules	17
2.4.3 Numerical methods	17
2.5 Theoretical description of C_{60}	18
2.5.1 Plasmons	18
2.5.2 Numerical treatment of C_{60}	19
3 nanoTRIMS	23
3.1 Introduction	23
3.2 Experimental Setup	24
3.2.1 Ion detection	26
3.2.2 Electron detection	27
3.2.3 Nanoparticle preparation	29
3.3 Experimental results	29
3.4 Theoretical results	32
3.4.1 Simulation details	32
3.5 Discussion	34
3.5.1 Analytical 1D model	35
3.5.2 Probing of the surface charges	37
3.5.3 Iterative optimization algorithm	38
3.6 Conclusion	39

4	Plasma expansion of nanoparticles	43
4.1	Introduction to x-ray free-electron laser experiments	43
4.2	Interaction of strong fields with nanoparticles	44
4.2.1	Previous theoretical work	44
4.2.2	Elastic scattering	45
4.3	Experimental Results	47
4.3.1	Setup	47
4.3.2	Comparison with MicPIC model	48
4.3.3	Analysis of scattering images	49
4.4	Conclusion	50
5	Photoemission time delays of C₆₀	53
5.1	Introduction	53
5.2	Experimental setup for attosecond streaking measurements	53
5.3	Extraction of time delays	56
5.3.1	Spectrograms	56
5.4	Theoretical model of C ₆₀	59
5.4.1	TDLDA calculations	59
5.4.2	Monte Carlo simulation	60
5.4.3	Implementation of intrinsic ionization delay	64
5.4.4	Simulation results of neon	67
5.4.5	Results C ₆₀	68
5.5	Discussion	69
5.5.1	Plasmonic near-field	69
5.5.2	Comparison between experiment and simulation	70
5.6	Conclusion	73
6	Conclusion and Outlook	75
A	Appendix	77
A.1	nanoTRIMS	77
A.1.1	Resolution of spectrometer	77
A.1.2	Focal averaging	77
A.1.3	Nanoparticle preparation	78
A.1.4	Iterative optimization algorithm	79
A.2	Plasma expansion of nanoparticles	80
A.2.1	Scattering images of nanoparticles	80
A.3	Photoemission time delays of C ₆₀	81
A.3.1	Analytical formula for neon cross section	81
A.3.2	Linear extrapolation in neon	82
A.3.3	Effect of linear chirp on streaking delay	82

Acronyms

a.u.	atomic units
ADC	analog-to-digital converter
ADK	Ammosov-Delone-Krainov
arb. units	arbitrary units
ATI	above-threshold ionization
CEP	carrier-envelope phase
CLC	Coulomb-laser coupling
CPA	chirped pulse amplification
CTMC	classical trajectory Monte Carlo
CW	continuous wave
DFT	density functional theory
DLC	dipole-laser coupling
DLD	delay-line detector
EWS	Eisenbud, Wigner and Smith
FEL	free-electron laser
FWHM	full width at half maximum
GDD	group delay dispersion
HHG	high harmonic generation
HOMO	highest occupied molecular orbital
IR	infrared
KFR	Keldysh-Faisal-Reiss
LCLS	Linac Coherent Light Source
LDA	local-density approximation
MCP	micro-channel plate

MicPIC	microscopic particle-in-cell
MPI	multi-photon ionization
pnCCD	pn-junction charge-coupled device
PPT	Perelomov-Popov-Terent'ev
RPA	random-phase approximation
RPAE	random-phase approximation with exchange
SASE	self-amplified spontaneous emission
SLAC	SLAC National Accelerator Laboratory, originally: Stanford Linear Accelerator Center
TDC	time to digital converter
TDLDA	time-dependent local-density approximation
TDSE	time-dependent Schrödinger equation
TEM	transmission electron microscopy
TOF	time-of-flight
TT	Time-Tool
VMI	velocity map imaging
XFEL	x-ray free-electron laser
XUV	extreme ultraviolet

1 Introduction

In our daily life we notelessly experience various phenomena governed by electron motion on atomic scales, for example illumination by light emitting diodes, semiconductor electronics in cell phones or computers as well as biological processes such as photosynthesis. Naturally, the dynamics on such small dimensions happen on femto- and attosecond time scales ($1 \text{ fs} = 1000 \text{ as} = 10^{-15} \text{ s}$) and, thus, require observation methods with similar time resolution. In this work, ultrashort laser pulses with pulse durations on the order of the electron motion in atoms were used to study the light-matter interaction and the electron and ion motion on nanometer scale.

The invention of the laser in the 1960s laid the foundation for the observation techniques of molecular, atomic and electronic motion [1]. The tremendous decrease of laser pulse durations during the following years were enabled by different techniques including Q-switching [2], mode locking [3–5] and the introduction of broadband Ti:sapphire solid state lasers [6]. At the same time, laser amplifiers and especially the method of chirped pulse amplification (CPA) [7], awarded with the Nobel prize in Physics in 2018, drastically increased the achievable pulse energies and peak intensities to new levels. As a result, current laser systems offer strong-field few-cycle pulses reaching intensities sufficient to manipulate atomic potentials [8]. With the precise control over the transient of the electric field [9], it is possible to observe electron motion [10–13], to control molecular reactions [14] and to trigger tunneling ionization [15, 16]. Moreover, non-linear processes are necessary to create coherent, broadband radiation in the extreme ultraviolet (XUV) spectrum [17, 18] utilized for the generation of isolated attosecond pulses. Nowadays, these pulses are used in pump-probe experiments with unprecedented time resolution [19], as for example in attosecond streaking. These experiments reveal time delays during the ionization process in crystalline metals [11], gases [20, 21] or dielectrics [22]. Furthermore, they offer the possibility to link high-precision experiments with theoretical time-dependent Schrödinger equation (TDSE) calculations [23].

The targets investigated in this work exhibit a size of 1–300 nanometers, representing an intermediate range between single atoms and systems with billions of particles. On the one hand, quantum mechanical effects play a role, whereas on the other hand, solid state phenomena emerge due to the high number of involved atoms. The theoretical description of the observed phenomena is particularly challenging since many models are optimized for either low particle numbers or macroscopic effects in solids. Despite the complexity of the problem, the aim of this thesis was to find suitable approximations in the applied models

and learn about the intrinsic physics from the comparison between theory and experiment.

Furthermore, nanostructures offer the unique possibility to control and concentrate laser light to volumes much smaller than the applied wavelength [24]. This sub-wavelength localization causes an enhancement of the peak intensity enabling nonlinear processes in confined and well-defined volumes [12, 25]. The combination of confinement and enhancement of laser intensities opens the door to numerous applications in various fields, for example, optoelectronics [26, 27], biosensors [28] or photovoltaics [29]. Sharp tips with nanometer radii are an especially promising source of ultrafast localized electron emitters, especially when illuminated with few-cycle laser pulses [30–32]. Ultrafast electron sources offer great potential in the field of time-resolved electron diffraction of solids [33].

In the framework of this thesis, strong fields provided by few-cycle laser pulses as well as the localization in nanostructures are used to explore collective dynamics on nanometer scales with time resolutions below femtoseconds. One femtosecond is on the same order of magnitude as the oscillation period of the utilized laser light in the visible part of the spectrum ($T_{600\text{nm}} = 2\text{ fs}$).

The first part of the thesis (Chapter 3) covers the interaction of spherical nanoparticles with few-cycle laser pulses and the ionization of molecules on the particle's surface. Nanoparticles are of great interest in nanochemistry since they offer unique properties as photo-catalysts due to their large surface area [34, 35]. Moreover, enhanced near-fields, induced on the nanoparticle's surface under irradiation with light, can be used to control molecular reactions on the nanoscale. So far, however, there is no simple method available to spatially resolve near-field induced reactions on the surface of nanoparticles. In the present work, reaction nanoscopy is introduced to investigate photoionization of surface molecules, via resolving the momenta of ionic fragments in three-dimensions. The technique is demonstrated for laser-induced proton generation in dissociative ionization of ethanol and water on SiO_2 nanoparticles. This method enables the measurement of spatially dependent reaction yields on the surface. The experimental results are modelled and reproduced by electrostatic and quasi-classical Mean-field Mie Monte-Carlo (M^3C) calculations.

Besides the investigation of molecular reactions, this work addresses the plasma dynamics of strongly ionized nanoparticles. The plasma state of matter occurs in a variety of environments including astrophysical objects [36], technical applications [37, 38], nuclear fusion physics [39] and strong laser fields [40]. The theoretical treatment of plasma expansion needs to consider the non-equilibrium process and many-particle interactions. In Chapter 4, an experiment is presented that utilizes strong-field laser pulses ionizing nanoparticles into an expanding plasma. The plasma dynamics is monitored by a short x-ray free-electron laser (XFEL) pulse and compared to numerical calculations.

The third example for light-matter interaction is presented in Chapter 5. As a molecule consisting of dozens of atoms, C_{60} offers another possibility to investigate the collective motion of charged particles in photoionized systems. In the experiment, an attosecond laser pulse triggers the ionization process in the highly-symmetric molecule.

Simultaneously, this external XUV laser field excites a plasma oscillation of the valence electrons. So far, most measurements of the absorption spectrum are performed in the frequency domain. In this work, the dynamics of the C_{60} plasmon is revealed by a time-domain approach. The released electrons from the ionized C_{60} are probed in an infrared (IR) laser field, while enhanced near-fields additionally influence this probing process. The measured electron spectra contain temporal information about the photoionization process, which is used to obtain time-domain information about the collective dynamics at the plasmon resonance.

Publications

- F. Süßmann, L. Seiffert, S. Zherebtsov, V. Mondes, J. Stierle, M. Arbeiter, J. Plenge, P. Rupp, C. Peltz, A. Kessel, S. A. Trushin, B. Ahn, D. Kim, C. Graf, E. Rühl, M. F. Kling, and T. Fennel. Field propagation-induced directionality of carrier-envelope phase-controlled photoemission from nanospheres. *Nat. Commun.*, **6**:7944, 2015.
- L. Seiffert, F. Süßmann, S. Zherebtsov, P. Rupp, C. Peltz, E. Rühl, M. F. Kling, and T. Fennel. Competition of single and double rescattering in the strong-field photoemission from dielectric nanospheres. *Appl. Phys. B*, **122**:1–9, 2016.
- P. Rupp, L. Seiffert, Q. Liu, F. Süßmann, B. Ahn, B. Förg, C. G. Schäfer, M. Gallei, V. Mondes, A. Kessel, S. Trushin, C. Graf, E. Rühl, J. Lee, M. S. Kim, D. E. Kim, T. Fennel, M. F. Kling, and S. Zherebtsov. Quenching of material dependence in few-cycle driven electron acceleration from nanoparticles under many-particle charge interaction. *J. Mod. Opt.*, **64**:995–1003, 2016.
- L. Seiffert, P. Henning, P. Rupp, S. Zherebtsov, P. Hommelhoff, M. F. Kling, and T. Fennel. Trapping field assisted backscattering in the strong-field photoemission from dielectric nanospheres. *J. Mod. Opt.*, **64**:1–8, 2016.
- L. Seiffert, Q. Liu, S. Zherebtsov, A. Trabattoni, P. Rupp, M. C. Castrovilli, M. Galli, F. Süßmann, K. Wintersperger, J. Stierle, G. Sansone, L. Poletto, F. Frassetto, I. Halfpap, V. Mondes, C. Graf, E. Rühl, F. Krausz, M. Nisoli, T. Fennel, F. Calegari, and M. F. Kling. Attosecond chronoscopy of electron scattering in dielectric nanoparticles. *Nat. Phys.*, **13**:766–770, 2017.
- Q. Liu, L. Seiffert, A. Trabattoni, M. C. Castrovilli, M. Galli, P. Rupp, F. Frassetto, L. Poletto, M. Nisoli, E. Rühl, F. Krausz, T. Fennel, S. Zherebtsov, F. Calegari, and M. F. Kling. Attosecond streaking metrology with isolated nanotargets. *J. Opt.*, **20**:024002, 2018.
- Y. H. Lai, C. I. Blaga, J. Xu, H. Fuest, P. Rupp, M. F. Kling, P. Agostini, and L. F. DiMauro. Polarizability effect in strong-field ionization: Quenching of the low-energy structure in C_{60} . *Phys. Rev. A*, **accepted**, 2018.
- H. Fuest, Y. H. Lai, C. I. Blaga, K. Suzuki, J. Xu, P. Rupp, H. Li, P. Wnuk, P. Agostini, K. Yamazaki, M. Kanno, H. Kono, M. F. Kling, and L. F. DiMauro. Diffractive imaging of C_{60} structural deformations induced by intense femtosecond midinfrared laser fields. *Phys. Rev. Lett.*, **accepted**, 2018
- P. Rupp, C. Burger, N. G. Kling, M. Kübel, S. Mitra, P. Rosenberger, T. Weatherby, N. Saito, J. Itatani, A. Alnaser, M. Raschke, E. Rühl, A. Schlander, M. Gallei, L.

Seiffert, T. Fennel, B. Bergues, and M. F. Kling. Few-cycle laser driven reaction nanoscopy on isolated nanoparticles. *Nat. Comm.*, **submitted**.

- Q. Liu, S. Zherebtsov, L. Seiffert, S. Skruszewicz, D. Zietlow, S. Ahn, P. Rupp, P. Wnuk, A. Kessel, S. Trushin, A. Schlander, D. Kim., E. Rühl, M. F. Ciappinai, J. Tiggesbäumker, M. Gallei, T. Fennel, and M. F. Kling. All-optical spatio-temporal control of electron emission from SiO₂ nanospheres with femtosecond two-color laser fields. **in preparation**

2 Theory

This chapter addresses the basics of light-matter interaction and gives an overview of the photoionization which is the underlying principle of all experiments presented in the following chapters. The first part consists of a general description of ultrashort pulses and the effects caused by the propagation through matter. The next part discusses the different mechanisms of photoionizations in strong fields. Furthermore, the attosecond streaking technique and its special application to the measurement of photoemission time delays is introduced. The theoretical description of atoms and especially C_{60} during the streaking process is covered in more detail by introducing models for many-electron systems.

2.1 Ultrashort laser pulses

Ultrashort laser pulses are utilized in all experiments throughout this work. The electric field \vec{E} of a linearly polarized laser pulse can be described as an oscillation with the carrier frequency ω_L and a Gaussian envelope (see Fig. 2.1):

$$\vec{E}(x, t) = \vec{E}_0 \exp\left(-2 \ln(2) \left(\frac{t}{\sigma}\right)^2\right) \cos\left(\omega_L \left(t - \frac{x}{c}\right) - \phi(t)\right). \quad (2.1)$$

The intensity full width at half maximum (FWHM) is denoted as σ and for Fourier-limited pulses σ is related to the necessary frequency bandwidth $\Delta\nu$ by the condition

$$\sigma \cdot \Delta\nu = 0.44. \quad (2.2)$$

In order to achieve femtosecond pulses in the visible regime, the spectrum has to span almost one octave. Especially when pulse lengths of only a few optical cycles are used, the temporal phase $\phi(t)$ is of major importance for the evolution of the electric field. The temporal phase is usually expanded into a Taylor-Series as

$$\phi(t) = \phi_0 + \phi_1(t - t_0) + \frac{1}{2}\phi_2(t - t_0)^2 + \dots \quad (2.3)$$

with the derivatives defined as $\phi_n = \frac{d^n \phi}{dt^n} |_{t_0}$. The constant offset ϕ_0 is called the carrier-envelope phase (CEP) and shifts the carrier wave with respect to the envelope. The linear

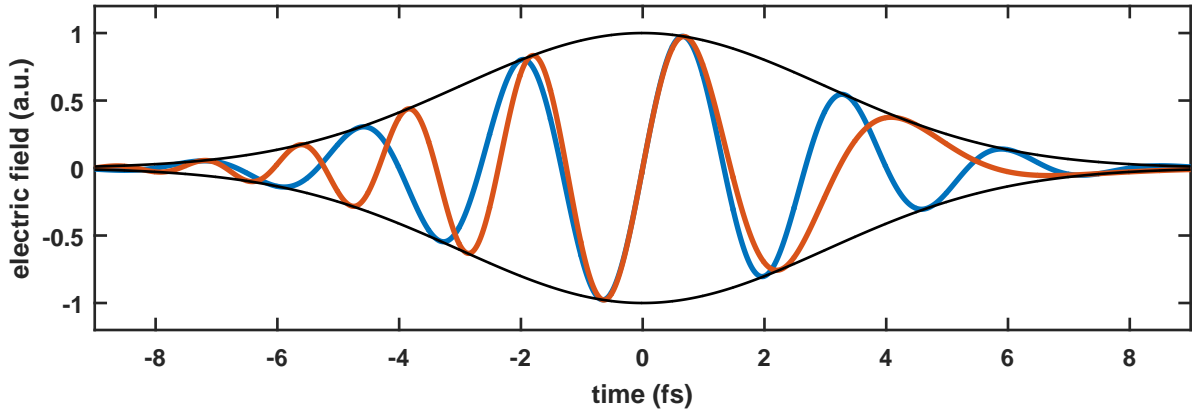


Figure 2.1: Temporal evolution of the electric field of a few-cycle laser pulse. The electric field of a 5 fs FWHM laser pulse without chirp is illustrated in blue. The shift with respect to the envelope (black) is defined by $\phi_0 = 0.5\pi$. A pulse with an additional temporal chirp $\phi_2 = 0.25 \text{ fs}^{-2}$ is shown in red. The instantaneous frequency of this chirped pulse is changing over time.

term ϕ_1 describes a shift in central frequency and can be included in ω_L . On the contrary, the quadratic term ϕ_2 is leading to a change of frequency with time. This effect is called linear chirp.

The electric field of a short laser pulse can be described in the spectral domain similar to the representation in the temporal domain. A simple Fourier-transform gives

$$E(\omega) = \int_{-\infty}^{\infty} E(t) \exp(-i\omega t) dt = \sqrt{S(\omega)} \exp(-i\varphi(\omega)). \quad (2.4)$$

The temporal phase $\phi(t)$ is converted into the spectral phase $\varphi(\omega)$ with the analogous definition: $\varphi_n = \frac{d^n \varphi}{d\omega^n} |_{\omega_0}$. Similar to the temporal case, φ_0 is responsible for the shift of the CEP and φ_1 is a shift in time, which is neglected for simplicity. The second order phase φ_2 describes the linear chirp and shows the same effect as a second order temporal phase. For a positive chirp, i.e. increasing frequency with time the parameter φ_2 is positive, which is opposite to the parameter β used in other publications [41, 42].

Few-cycle laser pulses and focusing optics enable intensities exceeding 10^{14} W/cm^2 by concentrating the optical power to a very short timescale and a small focal volume. The short pulse duration ensures both an excellent time resolution and high intensities while keeping the pulse energies below 1 mJ, avoiding the damage of optical components. Nonlinear optics usually deals with electric field strengths that occur between different atoms. This work, however, covers light-matter interaction with laser fields that have sufficient strength to manipulate the atomic potentials and bound electrons. In this regime, the exact time evolution of the electric field is of fundamental importance and can be used to control molecular dynamics on an attosecond timescale [10, 43].

2.2 Ionization mechanism

The ionization mechanisms described in this work are based on the interaction of light with matter. The exact type of mechanism and the ionization yield vastly depend on the electric fields and ionization potential during the interaction which can be described by the Keldysh parameter [44]

$$\gamma = \sqrt{\frac{I_p}{2U_p}} = \frac{\omega_L \sqrt{2mI_p}}{eE_0}, \quad (2.5)$$

which is determined by the ratio between the ionization potential I_p and the average quiver energy of an electron in an electric field E_0 , namely the ponderomotive potential

$$U_p = \frac{e^2 E_0^2}{4m\omega_L^2}. \quad (2.6)$$

If the ponderomotive potential is small compared to the ionization potential ($U_p \ll I_p$), the atomic potential is almost unaffected by the laser field and the ionization process can be treated perturbatively ($\gamma \gg 1$). To ionize from the bound state, $n \geq \frac{I_p}{\hbar\omega}$ photons are necessary and the ionization yield in the multi-photon ionization (MPI) regime scales as $Y_{\text{MPI}} \propto I^n$ (see Fig. 2.2a), with the intensity $I = \frac{1}{2}c\epsilon_0 E_0^2$.

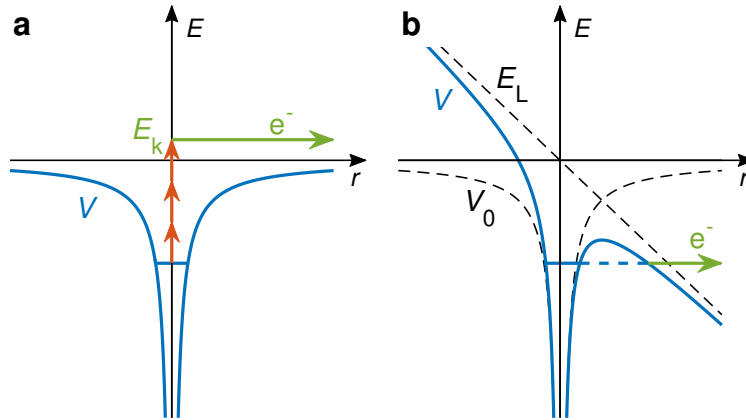


Figure 2.2: Illustration of possible ionization mechanisms. a) At least three photons are necessary to ionize from the bound state into the continuum by MPI. The electron has the kinetic energy E_k . The electric laser field is weak compared to the atomic potential V (blue). b) Tunnel ionization occurs for electric field strengths E_L that are comparable to the atomic fields V_0 . The resulting potential V is distorted each half-cycle and allows the electron to tunnel through the remaining barrier (dashed line).

In the limit $\gamma \ll 1$, the electric field is comparable to the atomic field strengths and

allows the bound electron to tunnel out into the continuum (see Fig. 2.2b). The yield in this case can be approximated by the tunneling probability through the residual potential barrier.

The calculation of ionization rates in strong fields has been subject to theoretical studies for almost one hundred years. The ionization rate for the hydrogen atom in a static electric field was first calculated by Landau and Lifshitz [45] based on the work of Oppenheimer [46]. For oscillating laser fields different approximations exist in the strong field limit: the Keldysh-Faisal-Reiss (KFR) theory [44, 47, 48] and the Ammosov-Delone-Krainov (ADK) theory [49]. Both theories are originally applied to atoms but can be extended for molecules as well [50–56]. Especially ADK theory is widely used due to its simple applicability to a wide range of cases in the tunneling regime. However, in the multiphoton regime ($\gamma > 1$) the more general Perelomov-Popov-Terent'ev (PPT) model should be applied [57, 58]. The ADK theory can be understood as a special case of PPT theory in the quasistatic limit.

The three step model or simple man's model describes the pathway of an electron in strong fields [59]. Upon ionization, in the first step, the emitted electron propagates in the laser field away from the parent ion and can be driven back to the core depending on the exact ionization time, which is denoted as the second step. In case the electron returns to the core with a kinetic energy of $3.17 U_p$, there are four possibilities (a–d) of interaction with the ion (step three):

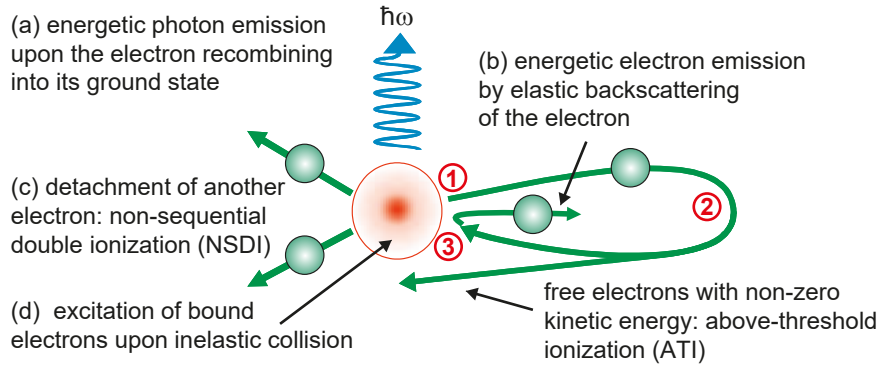


Figure 2.3: Three step model. The three steps (1–3) are indicated with red encircled numbers: Ionization, propagation and interaction with parent ion. The possible pathways of interaction are indicated (a–d). The illustration is modified after Ref. [60].

- a) The electron recombines with the ion and releases its energy in form of a photon. This process is called high harmonic generation (HHG) and occurs at each half cycle of the driving laser field in symmetric systems such as atoms [17, 18, 61]. The emitted photons have energies of the odd numbered harmonics up to $3.17 U_p + I_p$ [62, 63]. In case of solids or tips, the inversion symmetry is broken and the recollision is limited

to every second half cycle which results in the additional appearance of the even numbered harmonics. For a coherent and efficient creation of HHG radiation, the macroscopic conditions in the target need to be matched. The focusing condition together with the target pressure are absolutely essential to achieve phase matching in the short and long trajectories [64]. For the creation of single pulses, it becomes crucial to restrict the recollision process to a single half cycle [65]. All possible techniques act as a type of gating in a certain domain. Amplitude gating limits the spectrum to the cutoff energies [66, 67], polarization gating limits the recollision process by introduction of circular polarization before and after the peak of the pulse [68], double optical gating utilizes the second harmonic in the driving field [69], ionization gating makes use of depletion in the target [70] and with spatial gating the single pulses can be separated by tilting the phase front in the focus [71–73]. Each gating mechanism affects the spectrum causing a continuous shape with a fast decline at low energies and a flat plateau up to the cutoff region. The resulting temporal profile is a single attosecond pulse.

- b) The electron scatters elastically without a change of kinetic energy. Depending on the exact ionization time the final rescattered electron reaches kinetic energies up to $10.007U_p + 0.538I_p$ [74].
- c) The electron releases a second electron by impact ionization after returning to the atom. This mechanism leaves a doubly charged ion behind and is called non sequential double ionization [75–78].
- d) The electron scatters inelastically and leaves an excited ion behind [79, 80]. This excited ion relaxes or dissociates subsequently or may be probed by a second laser pulse.

Besides those four described interactions with the parent ion, the electron has a chance to get ionized by more photons than required to overcome the ionization potential [81]. This above-threshold ionization (ATI) results in peaks in the photoelectron spectrum that are separated by the photon energy.

2.3 Attosecond Streaking

A classical streak camera uses a fast varying electric field to deflect electrons that have been released by a photocathode. The electrons can be detected on a phosphor screen and translate any temporal information from the incoming optical pulse into spatial information on the screen. Typical optoelectronic streak cameras reach resolutions on the order of a picosecond. In this work, the same approach is applied with fully optical instead of electronic methods. Here, the deflecting electrical field is provided by a few-cycle laser pulse.

Attosecond streaking can be understood as a pump-probe experiment [65, 82–84]. The XUV pump is a single attosecond pulse generated by HHG and releases electrons from the sample with the initial kinetic energy $E_{\text{kin},0} = \frac{p_0}{2m} = \hbar\omega_{\text{XUV}} - I_p$ which is the XUV photon energy reduced by the ionization potential I_p . The probe is a few-cycle laser pulse with a defined delay τ relative to the pump and modulates the momentum of the electron depending on the delay. For the electric field component $E(t)$ parallel to the electron momentum the final momentum p_f can be calculated as

$$p_f(\tau) = p_0 + e \int_{\tau}^{\infty} E(t) dt = p_0 - eA(\tau). \quad (2.7)$$

A spectrogram $S(\tau, E)$ consists of several photoelectron spectra measured for different delays τ . It allows the full reconstruction of both the attosecond and the streaking femtosecond pulse, including the chirp of both pulses [85, 86]. Once those two pulses are characterized, they can be used to measure streaking from samples that reveal unknown physics, such as tunneling times in atoms [15], photoemission time delays from different atomic orbitals [21], inner-shell lifetimes measured by the Auger effect [20], Fano resonances in the autoionization process [87], the time delay between electrons from different bands in a metal [11], or the inelastic scattering process in dielectrics [22].

In this work, attosecond streaking is used to investigate the formation of collective electron dynamics in a C_{60} -molecule – the C_{60} plasmon (see Chapter 5).

2.4 Photoemission time delay

In streaking measurements, the direct relation between the pump-probe delay and the streaking laser field (Eq. 2.7) has to be extended for the intrinsic delays induced by the ionization process. During the ionization process, the motion of the emitted electron is delayed or accelerated by various electric fields and thus contains information about the underlying physical system. For example, the ionizing XUV pulse modifies the electronic state of the ionized atom or molecule and the residual potential interacts with the emitted electron and gets imprinted on its phase.

The first experiment that allowed the investigation of the attosecond ionization delays was performed in 2001 by Paul and coworkers [61], who performed the reconstruction of attosecond beating by interference of two photon transitions (RABBITT) [88–91]. As already mentioned, the HHG spectrum from atoms contains the odd numbered harmonics. In the target medium of a RABBITT measurement each absorption of one XUV photon can be followed by the absorption or stimulated emission of an IR photon (Fig. 2.4a). The additional interaction with the IR pulse leads to the appearance of even numbered harmonics, that can be reached by (at least) two possible pathways: for example $20 \hbar\omega = 19 \hbar\omega + 1 \hbar\omega = 21 \hbar\omega - 1 \hbar\omega$, i.e. 19th XUV harmonic plus IR absorption results in the same final energy as the 21st XUV harmonic plus IR emission.

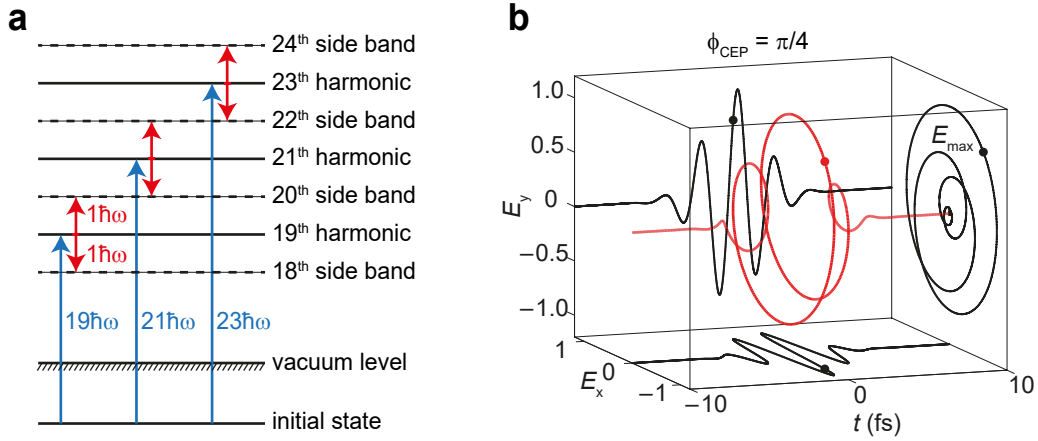


Figure 2.4: RABBITT and attoclock. a) Illustration of the RABBITT technique. One XUV photon is absorbed (blue) that corresponds to the uneven numbered harmonics (solid lines). Subsequently, an additional IR photon is absorbed or emitted, which form the side bands at even multiples of the IR photon energy (dashed lines). Adapted from Ref. [92]. b) The temporal evolution of a circularly polarized few-cycle laser pulse is shown in red. The projections on different planes (black) illustrate, how the maximum fields (dots) given by $\phi_{\text{CEP}} = \pi/4$ are converted to an angle in the polarization plane. Taken from Ref. [93].

The attoclock technique is a method making use of circularly polarized few-cycle pulses in order to resolve attosecond processes [93, 94]. The ionization process occurs at the maximum of the electric field E_{max} , that is oriented at a certain angle in the polarization plane (Fig. 2.4b). Subsequently, the photoelectron propagates in the electric field and the angle of the final momentum is measured in the polarization plane.

The emergence of CEP-stable few-cycle laser pulses and the generation of synchronized single attosecond pulses allows the measurement of the emitted electrons by attosecond streaking. This technique enables the investigation of the fundamental ionization processes with unprecedented resolution [60, 95–97]. Since the measurement unavoidably comprises the interaction with the streaking IR field, the effect of the probe pulse on the measured delays has to be taken into account.

2.4.1 Time delays in atoms

Ionization process

According to Eisenbud [98], Wigner [99] and Smith [100], the emission from an atom can be considered as one half of a scattering process. During scattering, the emitted electron accumulates a phase shift of $\delta(E)$ depending on the kinetic energy E which corresponds

to an Eisenbud, Wigner and Smith (EWS) time delay of

$$t_{\text{EWS}}(E) = \frac{d}{dE} \delta(E). \quad (2.8)$$

The description in the scattering picture is completely analogue to the classical picture of an electron at the distance $r(t)$ moving away with the velocity v at time $t \rightarrow \infty$:

$$r(t) = v(t - t_{\text{EWS}}). \quad (2.9)$$

In the large distance limit, the motion of the electron appears as a continuous movement with velocity v , delayed by the time t_{EWS} [101]. It is obvious that this free-particle approximation holds just for short-ranged potentials and becomes inaccurate when Coulomb potentials ($\sim \frac{1}{r}$) are involved. Since Coulomb potentials occur in most investigated systems, the EWS delay is not exactly defined [102].

As seen in Fig. 2.5, the extracted time delay depends on the chosen time for linear extrapolation. Due to the long-ranging potential, the electron stays under the influence of the central field and prohibits a defined extraction of time delays. The same problem arises in Eq. 2.8, since the phase shift between the emitted electron and an electron in free space is not defined. The emitted electron experiences a logarithmic phase distortion, in equivalence to the accelerated classical electron motion.

However, the logarithmic phase distortion can be disentangled into the intrinsic EWS delay and the time delay associated with the long range of the Coulomb potential. The main steps and final equations are as follows, for a more detailed derivation refer to Ref. [103]. The total time delay $t_{\text{Coul}}(E, l, r)$ is given by

$$\begin{aligned} t_{\text{Coul}}(E, l, r) &= \frac{\partial}{\partial E} \phi_{\text{Coul}}(E, l, r) = \frac{\partial}{\partial E} \left[\arg \Gamma \left(1 + l - i \frac{Z}{k} \right) + \frac{Z}{k} \ln(2kr) \right] \\ &= \frac{\partial}{\partial E} \arg \Gamma \left(1 + l - i \frac{Z}{k} \right) + \frac{Z}{(2E)^{3/2}} (1 - \ln(4Et)) \\ &= t_{\text{EWS}}(E, l) + \Delta t_{\text{Coul}}(E, r) \end{aligned} \quad (2.10)$$

and split into intrinsic delay which is independent from the propagation time and the Coulomb correction evaluated at $r = kt$ which is independent of the angular quantum number l . Once more the same result is obtained by propagating the electron classically in the Coulomb potential and applying Eq. 2.9 to the trajectory [104]. Note that the term associated with the attractive Coulomb potential results in a negative delay.

Interaction with streaking laser field

Eq. 2.10 considers the effect of the residual potential on the outgoing electron. In this section, an additional implication of the streaking IR pulse for the electron propagation is discussed. For *instantaneous* streaking as described by Eq. 2.7, the electron reaches

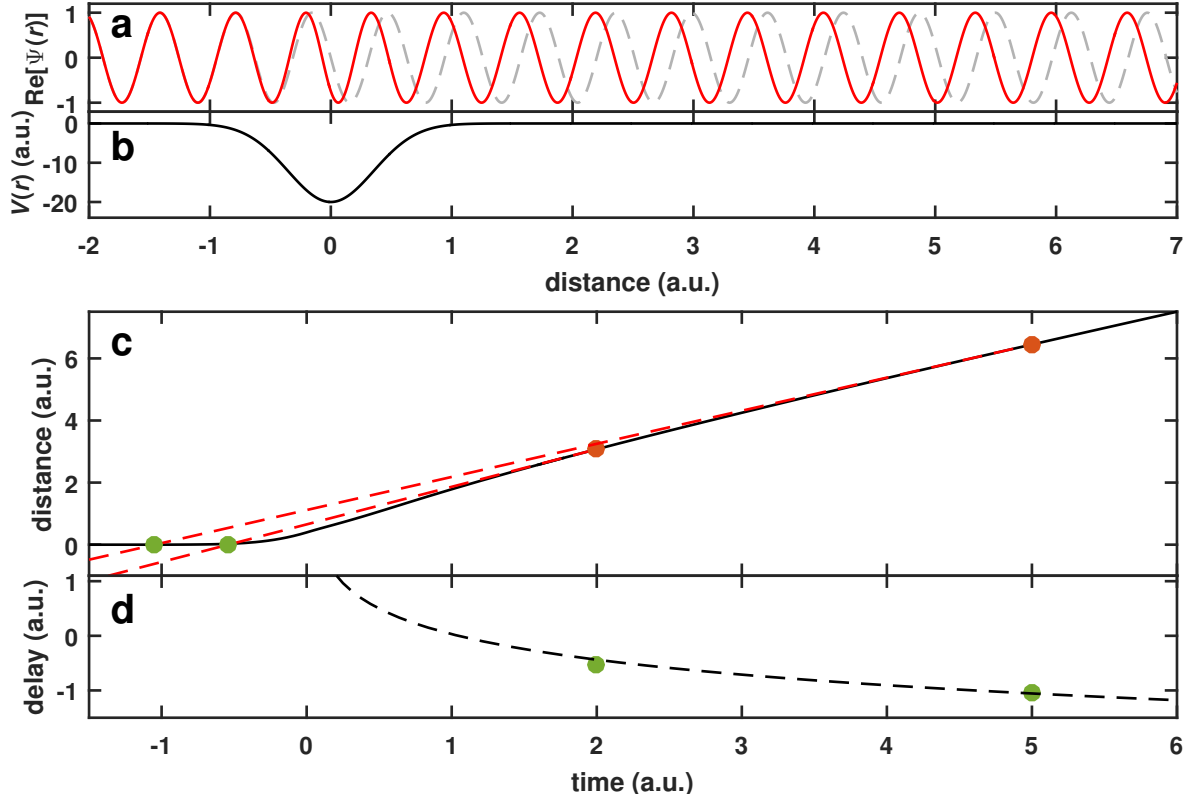


Figure 2.5: Electron scattering, Coulomb-laser coupling and EWS-delay. a) The wave function of a free electron is shown in grey as a reference. An electron, travelling through a potential well (b), experiences a change of the phase (red curve). c) In the classical picture the electron is moving away from an ion in a Coulomb potential (trajectory in black). At different time steps after the ionization (red points) the current position and velocity is evaluated and t_{EWS} calculated after Eq. 2.9. d) The retrieved delays are plotted in dependence of the propagation time (green points). The dashed line illustrates the delay given by Equation 2.10.

the momentum p_0 instantaneously and is driven by the pure laser field $E(t)$. Including effects from induced electric fields, the streaking equation is modified to account for any additional delays:

$$p_f(\tau) = p_0 - eA(\tau + t_S). \quad (2.11)$$

The temporal shift t_S may contain several components depending on the contributing effects. In all generality it is of the form

$$t_S = t_{\text{EWS}} + t_{\text{CLC}} + t_{\text{DLC}}^{(e-i)} + t_{\text{DLC}}^{(e-e)}. \quad (2.12)$$

First, the EWS and Coulomb-laser coupling (CLC) terms are discussed (Fig. 2.6). A comparison between TDSE calculations and a classical trajectory Monte Carlo (CTMC) simulation [105, 106] reveals, that similar to the plain ionization case, the intrinsic delay t_{EWS} (black) can be separated from the delay t_{CLC} (blue) associated with the long range of the Coulomb potential [107–109]. With this information, t_{CLC} is calculated classically and serves to extract the EWS delay from a measured streaking shift t_{S} (red) [110]. It is worth noting that t_{CLC} is independent of the IR probe intensity for a reasonable parameter range.

The last term in Eq. 2.10 is associated with the propagation of the electron in the Coulomb field which is probed after time t_0 . An analysis of CTMC simulations reveals that in case of streaking with a IR laser field the electron behaves exactly as being probed at a time $t_0 = 0.092 T_{\text{IR}}$, linked to the period T_{IR} of the IR field [103]. The delay associated with CLC results in:

$$t_{\text{CLC}} = \Delta t_{\text{Coul}}(E, r = kt_0) = \frac{Z}{(2E)^{3/2}}(1 - \ln(4Et_0)) = \frac{Z}{(2E)^{3/2}}(1 - \ln(0.37ET_{\text{IR}})). \quad (2.13)$$

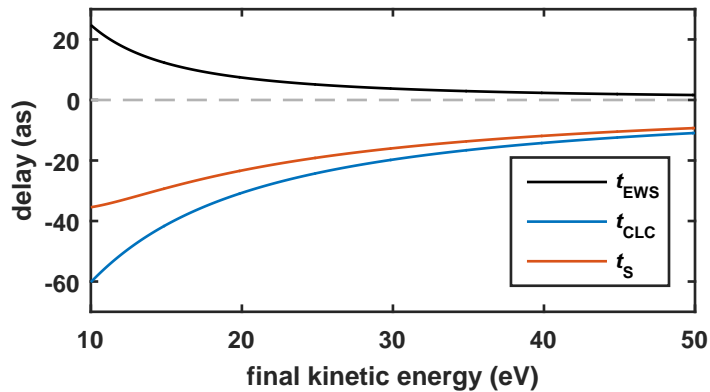


Figure 2.6: Delays in atomic hydrogen. The EWS delay (black line) from the ionization of hydrogen ($l = 1$) is shown in dependency of the final kinetic energy according to Equation 2.10. The CLC term (blue) is calculated for a 700 nm probing laser pulse (Eq. 2.13) and the resulting sum is shown in red.

The third dipole-laser coupling (DLC) term in Eq. 2.12 attributes to the interaction of the laser field with a dipole moment d_i of the initial state [111, 112]:

$$t_{\text{DLC}}^{(e-i)} = \frac{1}{\omega_{\text{IR}}} \tan^{-1} \left(-\frac{d_i \omega_{\text{IR}}}{p_0} \right). \quad (2.14)$$

Electron correlations

The model discussed in the previous section contained a single electron interacting with the electric fields and the residual ion. Now the interactions of electrons between each other

will be included. TDSE calculations reveal that electron interactions have to be treated as a coupling between the emitted electron and the dipole moment d_f of the final state of the ion [113–115]. The analogy to the coupling with the initial state becomes evident in the analytical terms as well (note the different sign):

$$t_{\text{DLC}}^{(e-e)} = \frac{1}{\omega_{\text{IR}}} \tan^{-1} \left(\frac{d_f \omega_{\text{IR}}}{p_0} \right). \quad (2.15)$$

The precisely known delays calculated for neon are used later as a reference for our experiments [116].

2.4.2 Time delays in molecules

In large atoms and especially in molecules, a high number of electrons interacts not only with each other but also with the ionic core during and after the ionization process. However, the numerical treatment becomes challenging due to the manifold of degrees of freedom. Since TDSE calculations are unfeasible for such complex systems more advanced methods need to be implemented, for example density functional theory (DFT) or random-phase approximation (RPA) [117]. Despite the numerical challenges due to the many-body interactions, the electron correlations open the path to investigate new effects arising from collective electron motions. The correlated electron motion in the reasonably complex molecule C_{60} will be discussed in Chapter 5. The measured time delays serve as a measure to access the ultrafast dynamics related to plasmonic excitations.

2.4.3 Numerical methods

A common variation of DFT is the local-density approximation (LDA) which is employed to quantum mechanically calculate many-electron systems. It was developed in 1964 [118, 119] and got awarded with the Nobel prize in 1998. The idea is based on the calculation of the electron ground state density n_e from which all relevant observables may be extracted. The density n_e is varied in such a way to achieve the lowest possible total energy of the system. The single electron wave functions $\varphi_j(\vec{r})$ each satisfy the Schrödinger equation (Kohn-Sham equations)

$$\left(-\frac{1}{2} \nabla^2 + V_{\text{eff}}(\vec{r}) \right) \varphi_j(\vec{r}) = \epsilon_j \varphi_j(\vec{r}) \quad (2.16)$$

and give the total electron density summed over all N electrons

$$n_e(\vec{r}) = \sum_{j=1}^N |\varphi_j(\vec{r})|^2. \quad (2.17)$$

The effective potential V_{eff} for each electron depends on the density itself

$$V_{\text{eff}}(\vec{r}) = V_{\text{ext}}(\vec{r}) + \int \frac{n_e(\vec{r}')}{|\vec{r} - \vec{r}'|} d^3r' + V_{\text{xc}}(\vec{r}) \quad (2.18)$$

and contains information about the complex interactions between the electrons. The external potential is given by $V_{\text{ext}}(\vec{r})$ and the electron-correlation potential is denoted as $V_{\text{xc}}(\vec{r})$. The essential information in this approach is contained in a useful choice of the term $V_{\text{xc}}(\vec{r})$. In the framework of LDA, the exchange-correlation potential is assumed to be a function of the electron density at the exact same position, which motivates the term *local-density approximation*. Since the effective potential depends on the electron density (Eq. 2.18), but is also needed to solve the Kohn-Sham equations for $\varphi_j(\vec{r})$ (Eq. 2.16), the set of equations have to be solved iteratively until a self-consistent solution of V_{eff} and $n_e(\vec{r})$ is found.

While the original DFT is completely static, the Kohn-Sham equations may be extended by the use of the Runge-Gross theorem [120] towards time-dependent local-density approximation (TDLDA) [121]. The exchange-correlation potential is still assumed to be *local*, but becomes a time-dependent function. With the advancing progress in computational power, DFT is utilized to calculate physical properties of complex systems [122], such as bulk solids, molecules, metallic clusters [123] and fullerenes [124, 125].

2.5 Theoretical description of C_{60}

The C_{60} molecule was first discovered in 1985 [126] and rewarded with the Nobel prize in Chemistry eleven years later. Even though many other fullerenes with even numbers of carbon atoms ($n = 20, 60, 70, 76, \dots$) are known, the most stable and most investigated representative is the buckminsterfullerene with $n = 60$ carbon atoms. Those atoms are regularly arranged at the vertices of 20 hexagons and 12 pentagons, which resembles the shape of a football.

2.5.1 Plasmons

A plasma oscillation describes the collective motion of an electron cloud with respect to an ionic background [127–129]. The quantized quasiparticle of this oscillation is called a plasmon. First experiments investigated the electron scattering from thin metallic films [130], where the observed peaks in the scattering spectrum are multiples of a distinct plasma frequency ω_p . A simple model of this plasma oscillation is represented by a thin electron gas with density n_e that is located around a fixed positive sheet of ions [131]. The electrons

are able to freely oscillate perpendicular to the surface with a frequency

$$\omega = \omega_p = \sqrt{\frac{n_e e^2}{\epsilon_0 m_e}}. \quad (2.19)$$

The overall charge of the systems stays 0, while the top and the bottom part of the system appear positive and negative periodically. Usually, the electronic states have lower excitation energies compared to the plasmon energy $E_p = \hbar\omega_p$.

The model of a flat conducting sheet may be modified to a hollow ionic sphere with a electron cloud that is displaced with respect to the positive background. This system behaves very similar to the flat model and serves as a simple approximation of the C₆₀ molecule.

2.5.2 Numerical treatment of C₆₀

Since the first theoretical prediction [132] and the experimental confirmation [124, 133] of a plasmon at 20 eV in C₆₀, there has been great progress in theoretical modeling and numerical calculations of the collective electron response in C₆₀ to electromagnetic fields. The static ground state is described by various types of jellium models with great precision [124, 134–136]. In the present work, a spherical shell of 60 C⁴⁺ carbon ions with a radius $R = 3.54 \text{ \AA}$ is utilized as a model. The 1s electrons are assumed to be tightly bound and the wave functions of the 240 valence electrons are obtained by solving the single-electron orbitals in the LDA for the exchange potential [118, 119, 137]. The thickness Δ of the electron shell is approximately 1.5 Å. The most important parameters modeling the C₆₀ molecule are shown in Table 2.1. Fig. 2.7a shows the potential averaged over all subshells and the energy level of the calculated electronic ground states.

C ₆₀ Parameter	Value
Mean radius R	3.54 Å
Thickness electron shell Δ	1.5 Å
Mean valence electron density n_e	1.0 Å ⁻³
Plasma energy $E_p = \hbar\omega_p$	37.1 eV

Table 2.1: Parameters of C₆₀ used throughout this thesis. The radius R , the thickness Δ [138] and the electron density n_e are calculated in the framework of a LDA jellium model. The derivation of the plasma energy is given in Chapter 2.5.1.

Electron correlations are indispensable for the description of plasmon effects due to the interaction with external electric fields. To treat many-body interactions, different approaches may be used, for example the RPA [140–145]. However, in the current work, all theoretical C₆₀ calculations for the analysis of C₆₀ streaking experiments (Chapter 5)

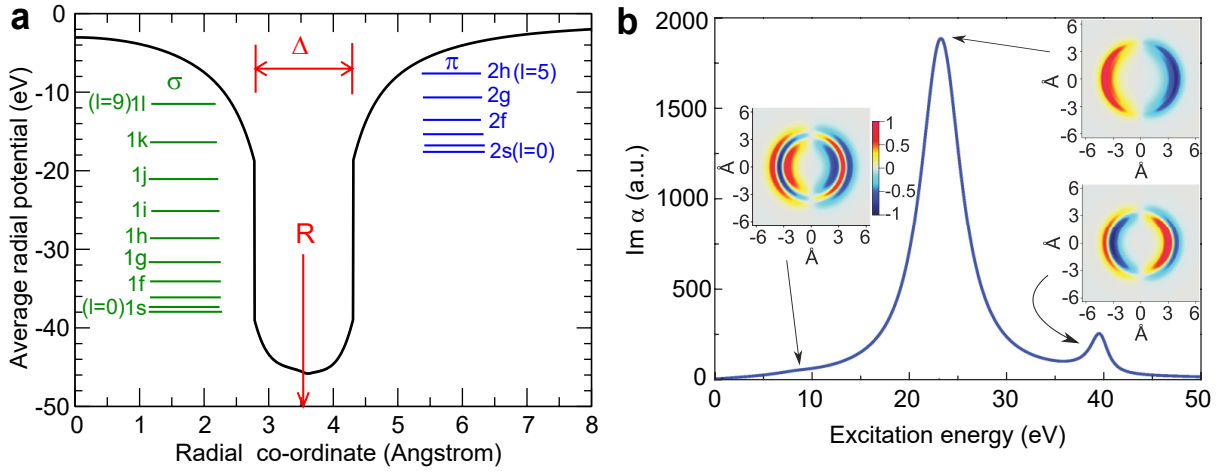


Figure 2.7: Radial potential and plasmon resonance. a) Radial potential averaged over all subshells. The main parameters are denoted as R and Δ (compare Table 2.1). The occupied σ ($n = 1$) and π ($n = 2$) ground state energy levels are shown in green and blue, respectively. b) The blue line shows the imaginary part of the polarizability. The three insets show the electron density changes in planes crossing the C_{60} molecule at selected excitation energies. The polarization direction is horizontal. The figures are taken from Refs. [125, 139].

are done in the framework of TDLDA [132, 135, 146–148]. Numerous comparative studies between the two mentioned methods have been performed [149, 150].

The principle behind TDLDA is the calculation of the dynamic response of the molecule to an external field on the basis of a DFT method. The susceptibility χ describes the frequency-dependent change of electron density $\delta\rho$ with respect to an external perturbation. Based thereupon the complex polarizability $\alpha(\omega)$ and the cross section $\sigma(\omega)$ are calculated. Two peaks in the cross section curves reveal a plasmonic response of the valence electrons at 16.5 eV and 38 eV [125]. The stronger peak is associated with a coherent oscillation of the electron cloud along the polarization axis [139, 151]. This mode is based on a varying electron distribution oscillating between the poles of the molecule. The weaker peak at about twice the frequency corresponds to a displacement of the electrons cloud with respect to the ionic shell. This mode is closely related to the simple model introduced for plasmons (Chapter 2.5.1), hence, the oscillation energy of 38 eV is almost identical to the calculated plasma energy of 37.1 eV. The terminology of those two modes was subject of an ongoing discussion [124, 152, 153], but the physical concept is found in the valence electron densities on the inner and outer shell surfaces, that oscillate with an in-phase and out-of-phase coupling. The resulting electron densities are illustrated as insets in Fig. 2.7b. Note that due to the single-electron origin of the calculated ground states, the individual subshells induce resonances for the autoionization of the collective states. Since the wavefunctions in the jellium model are more delocalized than in reality, the resulting

peaks in the cross sections are sharper than in experimental data [125]. Another effect is the finite temperature that broadens the experimental peaks.

The theoretical model is able to retrieve the overall oscillator strength in good agreement with the experimental value, even though it lacks a precise prediction of the resonance peak positions and widths. Due to the calculation of the wavefunction in local density approximation, the self-interaction of electrons is not included which neglects the Coulomb-part of the self-consistent potential. This approximation lowers (red-shifts) the calculated energies of the bound states compared to the experiment [140].

3 nanoTRIMS

3.1 Introduction

Nanomaterials exhibit a characteristic optical response, dependent on their size, material, composition and environment [154–156]. They feature a large surface to volume ratio and catalyze chemical reactions [157, 158], as, for example, in atmospheric photochemistry [159, 160]. The concentration and enhancement of electromagnetic fields on the nanoscale is important for various applications including detection of trace substances [161], single-molecule spectroscopy and microscopy [162, 163], as well as nanofocusing and modification of surfaces beyond the optical diffraction limit [164, 165]. The intrinsic ultrafast (collective) electron dynamics is crucial for opto-electronic applications with devices operating at PHz frequencies [166]. In all of these applications, the nanoscale, light-induced near-fields play a critical role. Electron emission and scattering in strong laser fields have shown to provide nanometer-resolved information about light-induced near-fields by mapping of the local near-fields onto the final electron momentum distributions [167–171]. Electron emission in extreme ultraviolet fields even permits sampling the near-field with sub-cycle (attosecond) temporal resolution [22, 172]. Despite this progress, unraveling the impact of near-fields on photo-induced reaction yields for molecular adsorbates remains challenging [173]. In this chapter, a solution is provided by implementing reaction nanoscopy, which permits accessing the nanoscale reaction yield landscape via 3-dimensional momentum spectroscopy of charged molecular fragments.

In the present proof-of-principle experiment, the proton generation from dissociative ionization of ethanol and water molecules adsorbed on SiO_2 nanoparticles is inspected. The yield shows an anisotropy regarding the emission direction, which reflects the spatial variability of the reaction on the particle surface following the near-field distribution at the particle. The experimental results are modelled by semi-classical Monte-Carlo trajectory simulations [172], including Mie near-fields, molecular ionization, and charged particle interactions. Laser-generated ions from isolated nanoparticles have been studied before to probe plasma generation in high-intensity laser fields and provide nanoscale information about the creation of the plasma [174]. In this work, much lower intensities are employed, yet with pulse durations of only a few optical cycles, which suppresses plasma formation [175] and the expansion of the particle during the interaction with the laser field. Under these conditions, molecular fragments emitted from the nanoparticle serve as

a sensitive probe of the local yield of light-induced reactions.

3.2 Experimental Setup

In order to detect laser-generated charges, a reaction nanoscope is designed (Fig. 3.1), which advances **R**ecoil **I**on **M**omentum **S**pectroscopy [176] towards **n**anosized **T**argets (nanoTRIMS). Linearly polarized laser pulses with a central wavelength of 720 nm, an energy of 300 μJ and a FWHM of the temporal intensity envelope of 4 fs are generated at a repetition rate of 10 kHz in an amplified Ti:sapphire laser system (Femtopower Compact Pro HR, Spectra Physics) with subsequent spectral broadening in an argon filled hollow core fiber. The broadened pulses are compressed by a set of chirped mirrors. A fraction of the beam is focused ($f = 12.5\text{ cm}$) to an intensity of $\sim 5 \times 10^{13}\text{ W/cm}^2$ in the interaction region of the reaction nanoscope (Fig. 3.1), which permits coincident detection of both ions and electrons, resulting from the interaction of the light pulses with a jet of free nanoparticles.

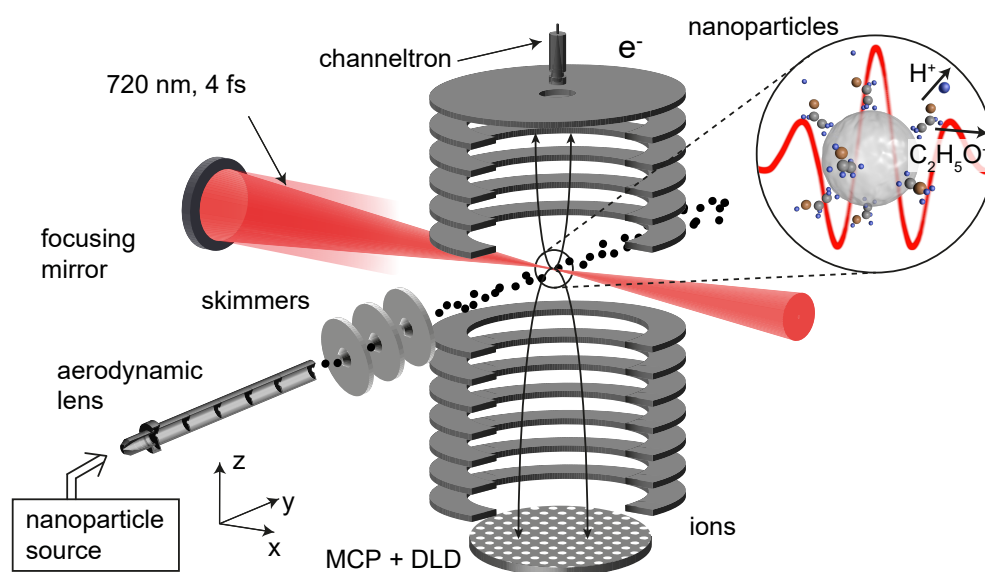


Figure 3.1: Reaction nanoscope. The few-cycle laser pulses cross the focused nanoparticle beam in the center of the reaction nanoscope. The SiO_2 nanoparticles and molecular surface adsorbates are ionized during the interaction. Fragments arising from molecular photodissociation are accelerated towards the ion detector (bottom: micro-channel plate (MCP) and delay-line detector (DLD)) by a homogeneous electric field. Electrons are accelerated towards the opposite side of the spectrometer and detected with a channeltron (top). Electrons and ions are recorded in coincidence.

The nanoparticles are generated in a source that has been described in detail in Refs. [177, 178]. The particles, dispersed in ethanol or water, are aerosolized using a fast

argon gas stream. A countercurrent dryer (Nafion, PermaPure, USA) [179] removes the solvent molecules from the carrier gas and the nanoparticle surface. Nanoparticle clusters are eliminated from the gas stream by an impactor unit. An aerodynamic lens focuses the nanoparticle beam to a spot size of approximately 0.5 mm in diameter in the center of the reaction nanoscope, where ultra-high vacuum (10^{-9} mbar) conditions are maintained.

Electrons and ions created in the interaction region are accelerated within a homogeneous electrostatic field (up to 150 V/cm) towards their respective detectors, i.e. an MCP for the ions and a channeltron for the electrons (see Fig. 3.2). The main volume of the spectrometer is confined by uniformly spaced electrodes on the sides and electroformed meshes (Precision Eforming, USA) [180] towards the detectors, that let the charged particles through and provide a flat electric field distribution. Even though the grounded nanoparticle source is within a few millimeters of the electrodes to achieve optimal target density, the electric field is almost perfectly homogeneous inside the spectrometer. The gradient between the mesh and the MCP is increased to accelerate the ions and achieve a high detection efficiency. The front of the channeltron is floating on a positive voltage for the same reason, but has a smaller detection angle compared to the MCP due to its smaller dimensions.

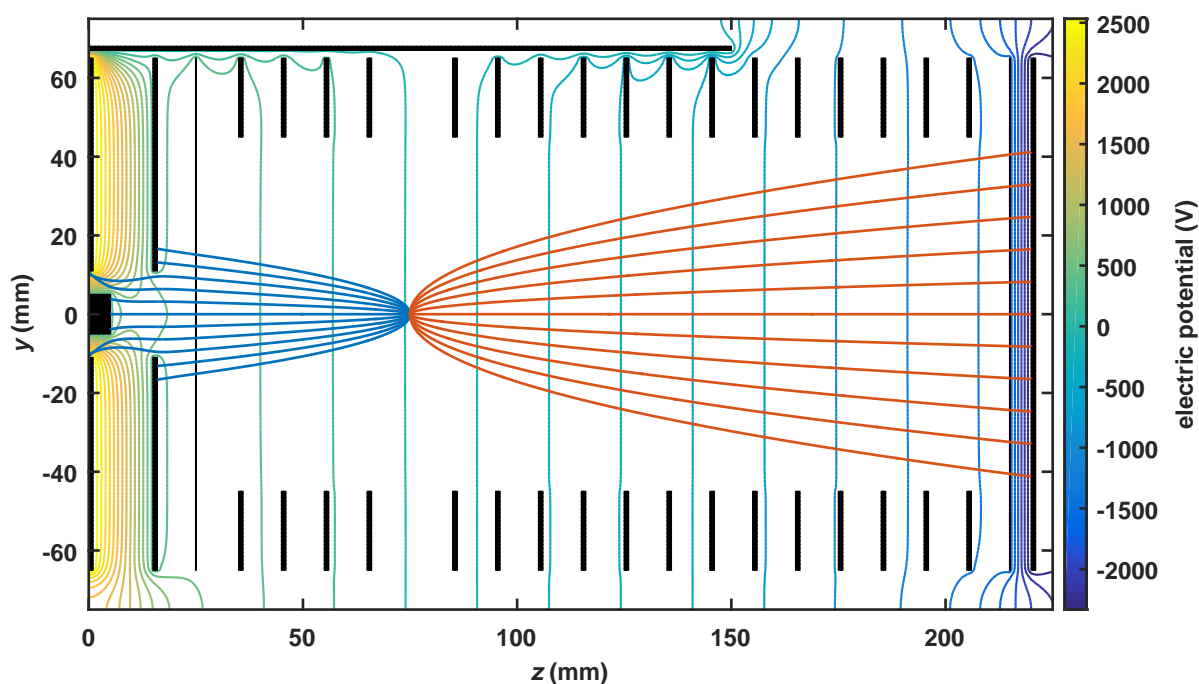


Figure 3.2: Electrostatic potentials in the spectrometer. All black lines are electrodes with a fixed electric potential. The thin lines ($z = 25$ mm and $z = 215$ mm) are meshes that are transmissive for ions and electrons and the central block on the left is the channeltron for electron detection. The horizontal line ($y = 67$ mm) illustrates the nanoparticle source. Typical trajectories for electrons and ions are shown in blue and red, respectively.

The contour lines in Fig. 3.2 illustrate the electric potential in the yz -plane calculated in SIMION 8.1 [181, 182]. In order to record ions with high momenta in the detector plane, high voltages are applied to the spectrometer. For a more detailed evaluation of the spectrometer design, particle trajectories are calculated for these high voltage conditions. The red lines represent H^+ ions starting in the focus with an initial momentum in y direction between -63 a.u. and $+63$ a.u., corresponding to a kinetic energy of 29 eV. This value also corresponds to the maximum detectable H^+ momentum in the detector plane.

For a given voltage, the maximum momentum along the spectrometer axis is in any case limited by the length of the spectrometer on the side opposing the detector. Furthermore, very high momenta in the time-of-flight (TOF) direction result in an overlap between neighbouring species. For example, under the experimental conditions the time-of-flight of H^+ with approximately 150 a.u. momentum would coincide with the time-of-flight of H_2^+ .

The shown electron trajectories in blue cover a momentum range between -0.9 a.u. and $+0.9$ a.u., corresponding to kinetic energies up to 11.4 eV.

3.2.1 Ion detection

Ions are detected with a time- and position-sensitive detector consisting of a multichannel plate (MCP) and a delay line detector (DLD). From the time-of-flight and position, the three-dimensional initial momenta of the fragment ions are retrieved. Due to the processing electronics, a dead time of ~ 10 ns occurs for the ion detection. The resolution of the retrieved momenta is influenced by various effects:

- Fig. 3.2 shows that the field inside the spectrometer is homogeneous and thus analytical formulas can be used to calculate the particle trajectories. Due to these well-behaved fields the relationship between the initial momenta and the measured time-of-flights is linearized and sufficient for precise momentum retrieval. In our case, distortions in the electric fields play no significant role for the resolution of the spectrometer.
- The finite size of the laser focus and the initial position of the charged particle translates to an uncertainty in the momentum determination. The extent of this effect is discussed in more detail in Chapter A.1.1. The resulting error in momentum is approximately 0.1 a.u. perpendicular to and 0.5 a.u. along the laser propagation axis.
- Ultimately, the momentum resolution is limited by the time resolution of the time to digital converter (TDC). Even though the bin size is 25 ps, the resolution achieved under experimental conditions is around 150 ps, corresponding to a resolution of 0.12 a.u. for H^+ in direction of the spectrometer axis. In the detector plane the spatial resolution of ~ 0.1 mm translates to about 0.16 a.u. momentum resolution. In summary, the expected uncertainties on the proton momentum due to detector system are on the same order as the uncertainties induced by the focus size.

In all time-of-flight experiments with a given spectrometer length, the applied voltages underly two major constraints: A small field strength reduces the momentum uncertainty induced by the time resolution of the detector but at the same time increases the maximum detectable momenta. Due to the latter effect, a comparably large gradient is chosen to measure high energy protons in this work. The resulting detector momentum resolution is on the same order of magnitude as the error induced by a finite focus size. Independently of the detector characteristics, the temperature of the investigated target broadens the measured momentum distributions. For example, the target temperature in this work is around room temperature resulting in $k_B T = k_B \cdot 293 \text{ K} \approx 25 \text{ meV}$, which is well below the investigated energies at tens of eV.

3.2.2 Electron detection

The electron side is equipped with a channeltron (MAGNUM 5901, Photonis, USA), enabling counting the number of released electrons. The channeltron signal is capacitively decoupled from its anode and further averaged in a boxcar integrator (SR250, Stanford Research Systems, USA) over a predefined gate window for each shot. The averaged signal is recorded by an analog-to-digital converter (ADC). In order to reveal the relation between the number of electrons and the integrated signal, histograms are calculated that show the number of laser shots with a specific channeltron signal (Fig. 3.3a). In the first measurement the spectrometer voltages are about ten times lower compared to Fig. 3.2 to improve the electron sensitivity. However, this would not allow the detection of high energy protons. Most laser shots do not contain any detected electrons, which shows up as a sharp peak at the background level of the channeltron. At higher signals individual peaks appear that are assigned to additional single electrons in each shot. It is confirmed that for up to three electrons the integrated signal scales linear with the number of electrons. Since the count rate for four or more electrons is very low, the peak position can not be determined.

A more elaborate evaluation of the channeltron response was done by increasing the background pressure in the interaction region and monitoring the resulting channeltron signal k . For each pressure value p a histogram was recorded and compared to an empirical fit function $P(k)$ (Fig. 3.3b):

$$\begin{aligned}
 P(k) &= \sum_{n=0}^{\infty} A_{\lambda}(n) \frac{1}{\sqrt{2\pi\sigma_n^2}} e^{-\frac{1}{2}\left(\frac{k-\eta n}{\sigma_n}\right)^2} \\
 \text{with } A_{\lambda}(n) &= \sum_{i \geq n/2}^n \frac{\lambda^i}{i!} e^{-\lambda} \binom{i}{n-i} p_{\text{sec}}^{n-i} (1-p_{\text{sec}})^{2i-n}, \\
 \text{and } \sigma_n &= \begin{cases} \sigma_0, & n = 0 \\ \sigma_c, & n > 0 \end{cases}.
 \end{aligned} \tag{3.1}$$

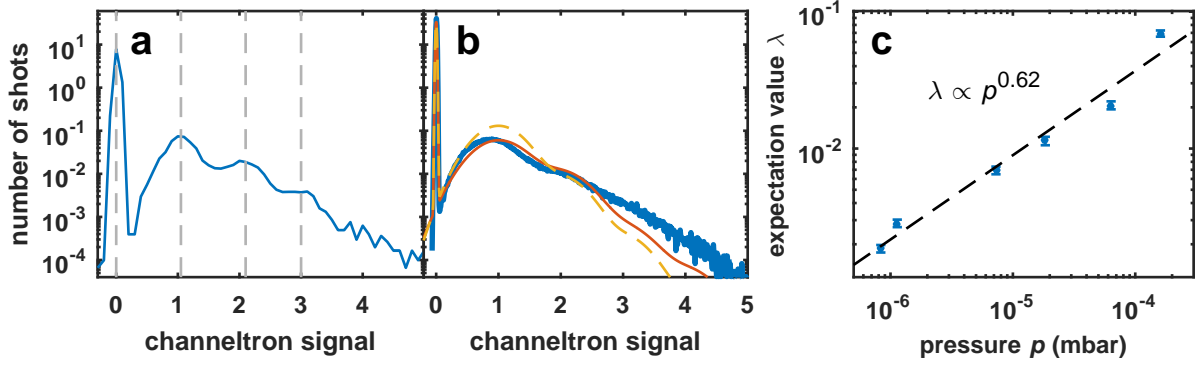


Figure 3.3: Channeltron calibration. a) The histogram shows the occurrence for each channeltron signal on a logarithmic scale. The spectrometer voltages are comparably low (explanation in text). b) The histogram (blue) shows one measurement of the background pressure scan for channeltron calibration. The spectrometer voltages are the same as in usual nanoparticle experiments. The yellow dashed line is a fit to the histogram with a plain Poisson distribution of Gaussian functions ($p_{\text{sec}} = 0$). The red line is a fit using the modified Poisson distribution. c) The fitted number of expected electrons λ per shot are plotted against the background pressure p . The black line is an exponential fit to the data points (formula indicated).

The concept behind the function $P(k)$ is a Poisson distribution with λ expected electrons per laser shot. Each number of electrons causes a Gaussian shaped signal with a width σ_0 for the zeroth peak and a width σ_c for all other peaks. The width of the zeroth peak is narrower because it is caused by noise coupled into the coaxial cables summed up in the boxcar integrator. All other peaks are broadened due to noise amplified in the channeltron. The relative scaling between the channeltron output and the number of electrons is encoded in the parameter η . The yellow dashed line in Fig. 3.3b shows a fit for a Poisson distribution of Gaussian functions, i.e. the function $P(k)$ with ($p_{\text{sec}} = 0$). This perfect Poisson distribution shows a faster decay towards higher number of electrons than the experimentally measured histogram. This behaviour indicates an increased probability for multiple electrons per laser shot. Therefore, the Poisson distribution is modified by a binomial distribution. This modification can be understood as follows: Each electron has a chance p_{sec} to release a secondary electron from the mesh or the electrodes, which is detected simultaneously. Even though the exact mechanism is not investigated further, the empirical formula is in good agreement with the measured data (red line). The fit of $P(k)$ is performed on logarithmic scale for all pressures. Most fit parameters are independent of the pressure, for example the average widths $\sigma_0 = 0.011$ and $\sigma_c = 0.42$ and the scattering probability $p_{\text{sec}} = 0.13$ is found for all fits. In contrast, the parameter λ clearly increases with the pressure p (Fig. 3.3c). The electron per shot expectation value is a sub-linear function of the background pressure with an exponent of ~ 0.62 . The calibration of the

channeltron confirms that the relation between the channeltron signal and the number of electrons is not perfectly linear but – more importantly – follows a monotonic behaviour. A large number of detected electrons is expressed in a high channeltron signal and vice versa, which is used later for the nanoparticle detection.

The data for electrons and ions is collected in coincidence for each laser shot up to the full repetition rate of 10 kHz. To preserve coincidence conditions, the total count rate in the experiment is maintained at ~ 0.3 ionization events per shot, resulting in about 30 laser-nanoparticle interactions per second due to the dilute nanoparticle beam.

3.2.3 Nanoparticle preparation

Silica nanoparticles with diameters of 110 nm and 300 nm were prepared with a narrow size distribution by wet chemistry approaches. The synthesis was performed at the Technical University Darmstadt by the group of Dr. Markus Gallei. First of all, small seed nanoparticles were prepared by the Stöber method [183]. In a typical seed preparation procedure 21 g of TEOS¹, 28 ml of ammonia solution (25 wt% in water) and 1 ml of water were added to 530 ml of ethanol and stirred for 12 h. A further shell was grown on the silica nanoparticles by the seeded growth method [184] until the desired particle size was reached. All samples were stored in ultrapure ethanol after cleaning. Characterization by transmission electron microscopy as well as dynamic light scattering yielded a polydispersity of about 4.9% for the 110 nm and 2.9% for the 300 nm particles, respectively (see Chapter A.1.3). The surface of silica nanoparticles prepared by the Stöber method are typically covered by silanols, i.e. Si-OH groups [185].

3.3 Experimental results

First, the measurement results from the channeltron are investigated. The signal is recorded for each shot and the occurrence of each signal value is visualized in a histogram. The ionization of background gas produces by itself a low electron signal at the channeltron, see red curve in Fig. 3.4a for the measurement of a target consisting of solvent without nanoparticles. The background gas in this case consists of argon with traces of residual solvent ethanol/water molecules. In contrast, the nanoparticle ionization gives rise to a much higher and well discriminated electron signal, as seen from the blue curve in Fig. 3.4a. A high electron count measured in coincidence with the ion momenta is therefore a distinct marker to identify nanoparticle ionization events, which occur in only 0.3% of all laser shots. The main contribution to the ion TOF spectrum obtained for nanoparticle hits (Fig. 3.4b) results from solvent molecules adsorbed on the nanoparticle surface, in this case mostly C₂H₅OH (46 u), which mainly fragments into H⁺, CH₃⁺, CH₂OH⁺, and C₂H₅O⁺, and some traces of H₂O (18 u), which fragments into H⁺, and OH⁺. The peak

¹tetraethyl orthosilicate or tetraethoxysilane

intensity in the focus $8 \times 10^{13} \text{ W/cm}^2$ is determined from the $\text{Ar}^{2+}/\text{Ar}^+$ yield ratio with an estimated accuracy of 20% [186].

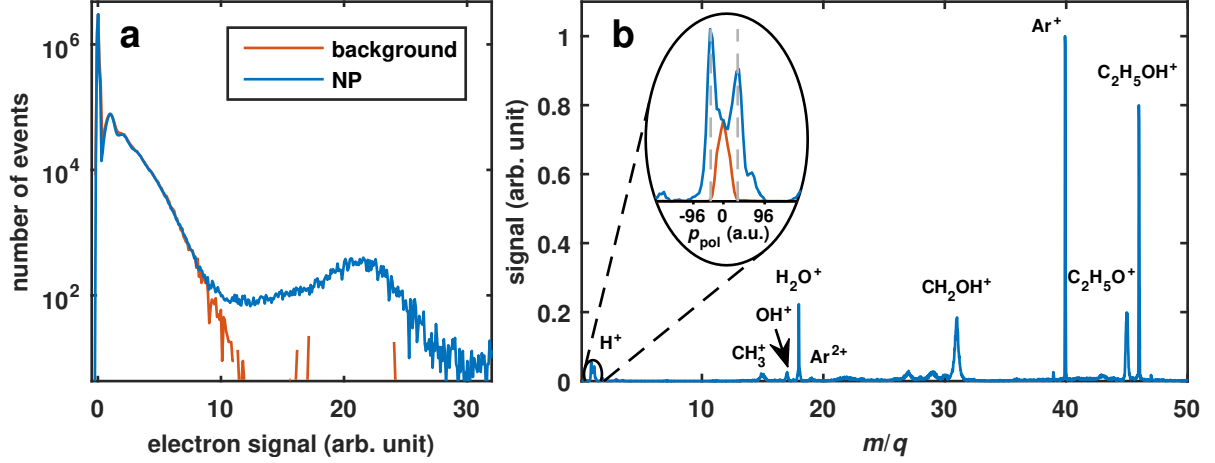


Figure 3.4: Experimental data. a) Histogram of the number of detected electrons from the interaction of few-cycle pulses with background gas only (red) and with 110 nm SiO_2 particles (blue). b) Average ion TOF spectrum of shots containing nanoparticle hits. The indicated ionic fragments arise from ionization of argon and dissociative ionization of ethanol and water. The inset shows the enlarged peak of H^+ on a momentum scale along the polarization direction (p_{pol}), for events with SiO_2 particles (blue) and with just background gas (red). The grey dashed lines indicate a momentum of ± 40 a.u. The Ar^{2+} peak is just indicated but is not visible on a linear scale.

Careful inspection of the average TOF spectrum recorded for nanoparticle hits reveals a sensitive dependence of the H^+ peak to the presence of nanoparticles, evident by the appearance of two satellite peaks in the momentum along the polarization direction (p_{pol} , see inset in Fig. 3.4b). We note that peaks for higher masses in the TOF spectrum do not permit to resolve this feature due to the low momentum difference. The TOF spectra indicate that the protons are mainly generated from the dissociation of water or ethanol molecules (or to some extent also silanols) on the nanoparticle surface.

In order to elucidate the origin of the proton peak splitting in the TOF spectra, the angular resolved density maps of final proton momenta are inspected (Fig. 3.5). We have carried out experiments for SiO_2 nanoparticles with a diameter of $d = 110$ nm and $d = 300$ nm. Selecting the events that were coincident with a high electron signal facilitates the efficient suppression of the proton signal from the background gas. For both sizes, the final proton momentum distribution cannot be explained by strong field dissociative ionization of ethanol or water alone [187]. Indeed, protons from the background gas, which are generated in the absence of nanoparticles, have a narrower momentum distribution with a single peak at zero momentum (inset Fig. 3.4b). This comparison indicates that energetic protons in the nanoparticle experiments originate from solvent molecules adsorbed on the nanoparticle

surface. The strong dependence of the observed proton momentum distribution on the nanoparticle size corroborates this hypothesis. As seen in Fig. 3.5, the angular proton distribution has a dipolar shape for 110 nm particles (Fig. 3.5a), while it exhibits a strong asymmetry for 300 nm particles (Fig. 3.5c). It is intuitive to compare the observed proton distribution to the laser induced near-fields for the investigated nanoparticles. For particle sizes that are small compared to the wavelength, the near-field spatial distribution exhibits a dipolar character, while for particle sizes approaching the wavelength, the maximum of the distribution shifts toward the light propagation direction [167]. In the following sections, it is shown how the local near-fields induce a transient charge distribution on the particle surface, which in turn determines the final proton momentum distribution.

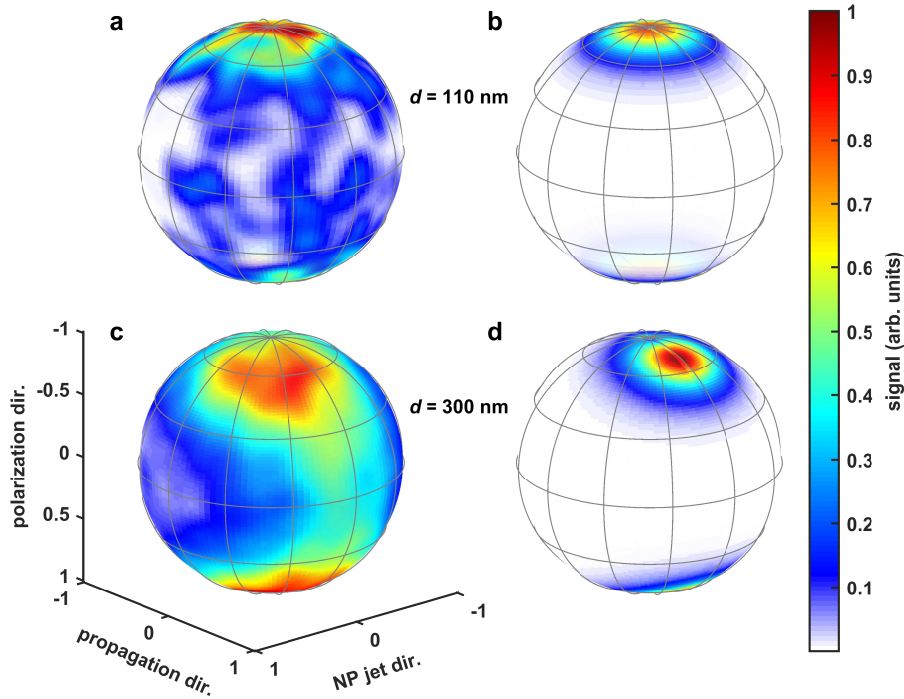


Figure 3.5: Comparison of measured and simulated angular proton distributions. The 3D (φ, θ, r) momentum distributions of protons are integrated along the radial coordinate and the retrieved two dimensional (φ, θ) density map is spanned over a unit sphere. The number of protons per solid angle is encoded in the color scale: a) and b) show, for the 110 nm particles, the measurement and Monte-Carlo trajectory simulations, respectively, and c) and d) the analogues for the 300 nm particles.

3.4 Theoretical results

To shed light on the mechanisms that govern the experimental proton momentum distributions, we performed three-dimensional semi-classical simulations of the charged particle (electrons and ions) dynamics.

3.4.1 Simulation details

Numerical model for electrons

The electron trajectories are calculated using the M³C-code described in Refs. [167, 168], which has shown to quantitatively agree with experimentally measured electron momentum distributions for few-cycle ionization of nanoparticles [167]. In our model, electrons are liberated via tunnel ionization under the action of the total electric field consisting of the laser field, the dielectric response of the nanosphere approximated by the Mie-solution and the mean field of all charged particles. At each time step, a Monte-Carlo method is used to launch electron trajectories weighted according to an ADK-type tunneling rate [49]. Elastic and inelastic collisions of electrons with the nanoparticle are included in the propagation [167].

The ionization of a nanoparticle releases many electrons of which a large fraction stays inside the particle due to a positive trapping potential. The total number of emitted electrons scales approximately linear with intensity (logarithmic blue line in Fig. 3.6a) because of the counter-acting effect of the mean field [167]. The geometry of the spectrometer, the size of the channeltron and its inherent detection efficiency restrict the number of detected electrons (red line). The ratio between the detected and emitted electrons decays for larger intensities since the broader electron momentum distribution reduces the fraction of low energy electrons that are able to reach the channeltron.

Figure 3.6b illustrates how the electron signal histogram is obtained. Even though the simulated curves may deviate in some details from the measured data, they reflect the experimental conditions and help to understand the main principles. The red line from Fig. 3.6a is plotted on switched axes, i.e. intensity is plotted over the number of electrons. An analytic fit function is introduced in order to obtain smooth curves instead of discrete data points.

In order to create a histogram of the number of electrons per shot, the number of nanoparticle hits per intensity has to be included. This number is proportional to the inverse of the intensity due to focal averaging (yellow line, for details see Chapter A.1.2). The resulting histogram is presented in Fig. 3.6c in blue. As expected, the small volume with the highest intensities leads to an overall decrease of occurrence towards higher electron numbers. Notably, a flat curve in Fig. 3.6a leads to an accumulation of many intensity values on a small *number-of-electron-range*, which becomes visible as a pronounced peak. This mechanism is illustrated by the grey lines directed towards ~50 electrons. Vice versa

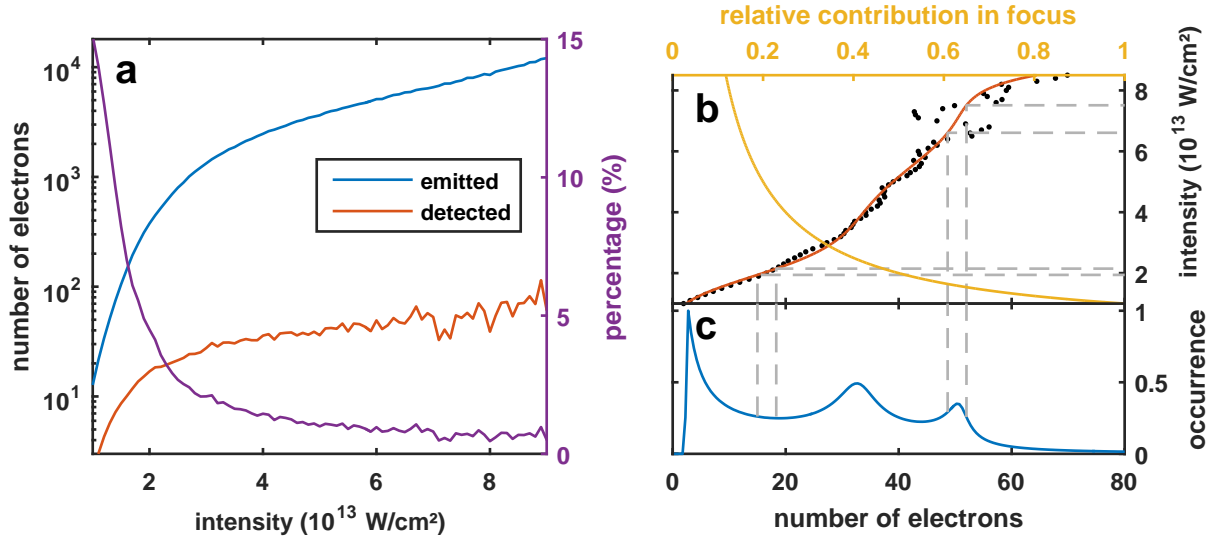


Figure 3.6: Simulated electron statistics. a) The blue curves reflect the simulated number of emitted electrons from a 300 nm SiO $_2$ particle. Under typical spectrometer voltages, a fraction (purple) of the electrons is detected by the channeltron (red). b) The black dots show the required intensities for each number of electrons. The data is smoothed for clarity (red). The yellow line indicates the weights due to the focal averaging. c) For each number of electrons the expected number of shots is integrated and plotted as a histogram (blue). The grey dashed lines are for visual guidance (explanation see text).

around 18 electrons the number of contributing intensity bins is comparably low, resulting in a minimum of the histogram. The exact positions of peaks may not coincide with the measured histograms, since they are very sensitive to the precise slope in the shown curves. Therefore, the simulated histogram does not exactly match the experimental result in Fig. 3.4a. However, the model succeeds to explain the most prominent features of the channeltron signal qualitatively and allows to utilize it for further investigation.

Numerical model for ions

In addition to ionization and propagation of electrons, we simulate the yield for the dissociative ionization, and calculate the trajectories of protons emerging from the strong-field dissociation of solvent molecules adsorbed on the nanoparticle surface. Protons are released at the peak of the laser pulse with zero initial momentum. We assume an I^n intensity-dependence for the dissociation rate to account for the spatial dependence of the ionization probability at the nanosphere surface. Here, $n = 6$ is the minimum number of photons needed to reach a dissociation channel into H $^+$ [188]. An adaptive time-step scheme is used to facilitate the propagation of protons up to 3 ns, where we find the momenta to be

converged. The calculation results for 110 nm and 300 nm particles (Fig. 3.5b, d) reproduce the experimental observations, in particular the observed change in proton momentum distributions with nanoparticle size. Based on the good agreement, we use the simulations to disentangle the different effects leading to the observed momentum distributions.

The proton momentum distributions incorporate the same averaging over the intensity distribution in the focal volume as the electron simulations for the channeltron. The weighting assumes a Gaussian beam profile. Low intensities leading to a low number of electrons are neglected in order to be consistent with the analysis of the experimental data, where those shots are filtered out. These laser intensities only affect the very central part of the momentum distribution.

3.5 Discussion

Earlier work on the interaction of few-cycle pulses with nanoparticles has concentrated on the mechanism of electron acceleration after photoemission from a solid. Süßmann et al. have revealed that electrons are generated on the nanoparticle surface in the regions of maximum field enhancement, and subsequently accelerated in the local near-fields [167]. It was experimentally and theoretically shown that released electrons gain most of their final energy from a combination of the dielectrically enhanced laser field and a local trapping potential induced by ionization [167, 168, 189]. In contrast, in the present studies on molecular adsorbates, we find that the much heavier protons do not gain significant energy by the enhanced field around the nanoparticle (see Fig. 3.7, inset). The simulations indicate that the final proton momenta are mainly determined by the potential on the nanoparticle surface (Fig. 3.7).

The surface potential arises from released electrons and the bound ions in the nanoparticle [190], which is repulsive for the protons. Coulomb attraction between the fast escaping electrons and created ions on the nanoparticle is negligible and has no significant effect on the final proton momenta. In contrast, the proton dynamics is dominated by electrostatic interactions with charges remaining on the nanoparticle surface. These charges form an inhomogeneous surface potential that traps electrons in a layer close to the surface and screens the inside of the nanoparticle. Due to the nonlinear nature of the ionization process, the surface charges are generated in the regions with the highest total field strengths. Their distribution has a similar shape as the H^+ momentum distribution: a dipolar shape for 110 nm particles and an asymmetric shape for 300 nm particles (see Fig. 3.5). In contrast to the much faster emission of electrons, protons efficiently probe the nanosphere surface on a picosecond time scale, which results in a mapping of the surface charge density landscape onto their final momentum distribution. This relation is a major difference compared to earlier work [167] and forms the basis for the mapping of reaction yields with the reaction nanoscope.

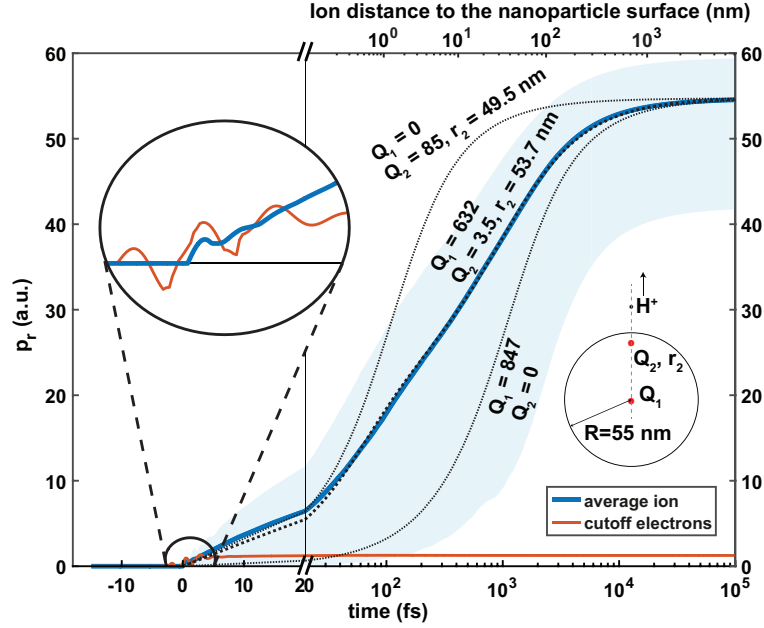


Figure 3.7: Analysis of proton and electron trajectories. The simulations are performed for 110 nm SiO_2 particles. The radial momentum $p_r = |\vec{p}|$ of the cutoff electrons (red) represents an average over the highest 10% of the electron momenta. The radial proton momentum (blue) is averaged over the initial spatial proton distribution on the surface. The blue shaded region indicates the spread between fastest and slowest protons. The axis on the top indicates the average distance of the proton from the nanoparticle surface at the respective times shown on the bottom. The left inset is a magnification of the region where the dynamics is laser-field driven. The right inset is an illustration of a simple model describing the 1D trajectory of a proton in the static field of two point charges, representing the (asymmetric) surface potential. The three dotted lines in the main graph show the trajectories for the model parameters indicated in the inset.

3.5.1 Analytical 1D model

The essence of the proton dynamics can be captured with a one-dimensional model along a radial axis (see green line in sketch in Fig. 3.7), where the electrostatic repulsion from two positive point charges is considered. A description by two point charges reflects the initial asymmetric surface potential around the sphere. A first charge Q_1 is situated in the center of the sphere and another charge Q_2 is placed at r_2 , below the nanosphere surface. A proton is launched from the surface on the axis defined by Q_1 and Q_2 .

Analytic solution for one charge

First, an analytical solution is presented for a special case of the one dimensional model. If only one of the charges Q_1 or Q_2 is taken into account and the other charge is set to zero, the equations of motion for this simplified situation can be derived analytically. It assumes a positive charge Q at position $r = 0$ for all times. The positive probe charge q of mass m is at position $r(t = 0) = R$ with $v(t = 0) = 0$. The equations of motion are solved in one dimension and result in:

$$\begin{aligned} t(r) &= \sqrt{\frac{2\pi m \epsilon_0}{Qq}} \left[\sqrt{Rr(r-R)} + R^{3/2} \log \left(\sqrt{\frac{r}{R}} - 1 + \sqrt{\frac{r}{R}} \right) \right], \\ p(r) &= \sqrt{\frac{mQq}{2\pi\epsilon_0} \left(\frac{1}{R} - \frac{1}{r} \right)}. \end{aligned} \quad (3.2)$$

The two characteristic quantities are

$$\begin{aligned} p_f(t \rightarrow \infty) &= \sqrt{\frac{mQq}{2\pi\epsilon_0 R}} \sim \sqrt{\frac{Q}{R}} \text{ and} \\ t_c &= \sqrt{\frac{2\pi m \epsilon_0 R^3}{Qq}} \left[\sqrt{2} + \log \left(1 + \sqrt{2} \right) \right] \sim \sqrt{\frac{R^3}{Q}} \text{ with } t_c \text{ defined by } E(t_c) = 0.5E(t \rightarrow \infty). \end{aligned} \quad (3.3)$$

The only free parameters here are the position R and the number Q of elementary charges. The final momentum is determined by the ratio $p_f \sim Q/R$. The number of charges ($Q \approx 850$) obtained from the analytical model for the measured final momentum of ~ 55 a.u. is comparable to that obtained with the numerical M³C simulations. However, an accurate fit of the temporal dynamics predicted by the M³C simulations with the simple model requires the inclusion of two charges, i.e. a non-spherically symmetric charge distribution and resulting surface potential.

Numerical solution for two charges

In the case of two charges, the trajectory is calculated numerically by integrating the differential equations. The position of the first charge is fixed to $r_1 = 0$ while the second position r_2 and the charges Q_1 and Q_2 are used as fit parameters. The fit of the two-charge model (see central dotted line in Fig. 3.7) to the full M³C simulations reveals a slightly reduced charge in the center ($Q_1 \approx 630$) and a very small charge ($Q_2 \approx 3.5$) located just 1 nm below the surface. Three free parameters (charges Q_1 , Q_2 and radius r_2) in total are enough to reproduce the correct dynamics of a proton in a Coulombic field. The large charge Q_1 in the center is necessary to model the correct final momentum while the second charge Q_2 at radius r_2 , introduced to represent the asymmetry in the charge distribution, ensures good agreement in the dynamic behavior.

3.5.2 Probing of the surface charges

The different time scales of the process allow the separation of the dynamics into two phases: A first phase, occurring on femtosecond scales, during which the surface charge distribution and the probe charges are generated in the laser-induced near-field, and a second phase, occurring on the picosecond scale, in which the probe charges are accelerated away from the now charged nanoparticle surface.

The final proton momentum distribution is determined by both the laser-induced surface charge density and the deprotonation rate of the surface molecules. It thus seems reasonable to retrieve both quantities from the measured proton momentum distributions. To solve this inverse problem, we use our simulations to find a quantitative description of the mapping between the initial proton position and the final proton momentum.

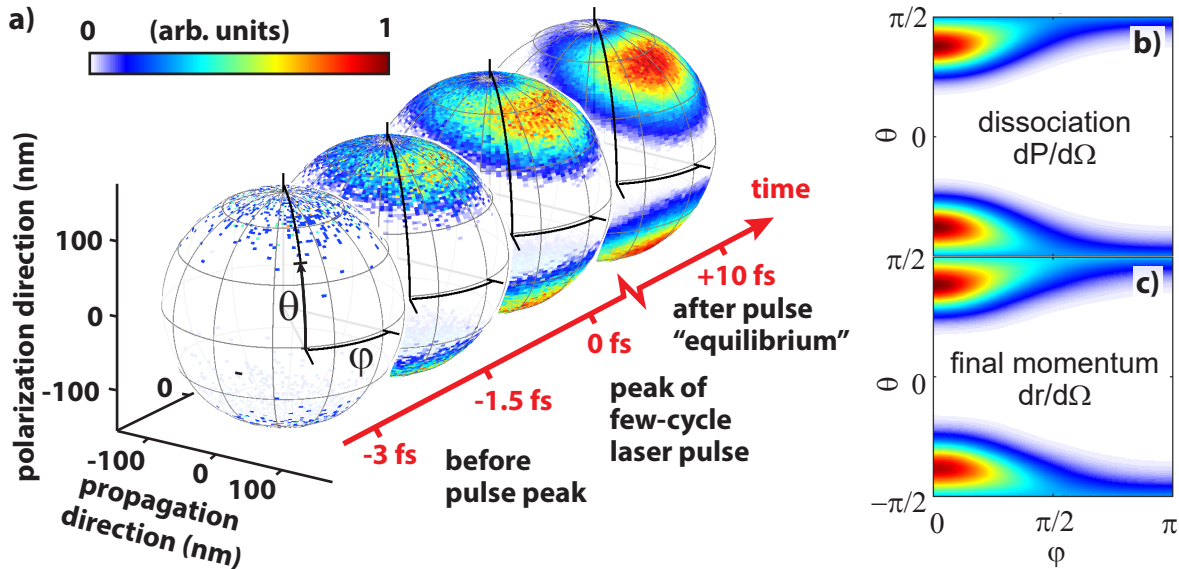


Figure 3.8: Dissociation yields on the nanoparticle surface. a) Time evolution of the surface charge distribution simulated for the 300 nm particle at a single intensity and averaged over the CEP. Two snapshots are shown during the rising edge of the laser pulse, one at the peak electric field and one 10 fs after the interaction with the laser pulse. Each point on the sphere is defined by the polar angle θ and the azimuthal angle φ , in the intervals $[-\pi/2; \pi/2]$ and $[0; 2\pi]$, respectively. The angle φ is only shown from 0 to π in the following plots due to the mirror symmetry with respect to the polarization-propagation-plane. b) Differential probability distribution $dP/d\Omega$ for the deprotonation reaction as a function of θ and φ . c) Experimentally accessible momentum distribution of the final proton momenta as a function of θ and φ . All distributions or rates are normalized to a maximum value of 1 and use the shown color scale.

Figure 3.8a illustrates the dynamics of the charge distribution on the surface of the nanoparticle. The spherical particle is ionized by the laser pulse on a timescale of a few femtoseconds. After this initial laser interaction the surface charge distribution reaches a quasi-equilibrium which governs the motion of the measured hydrogen ions. The initial spatial distribution of protons depends on the strength of the laser electric field and is shown in Fig. 3.8b as a function of the polar and azimuthal angles θ and φ . The resulting final proton momentum distribution is depicted in Fig. 3.8c. The two distributions are almost indistinguishable, stressing the close relation between position-space and momentum-space.

3.5.3 Iterative optimization algorithm

In order to retrieve the surface charge distribution quantitatively, an iterative optimization procedure was implemented. For a hypothetical completely spherically symmetric charge distribution, all protons are pushed away radially from the nanoparticle independent of the initial position. The final momentum direction coincides with the initial position and the final absolute value is the same for all protons. Therefore, the final distribution matches exactly the initial dissociation yield.

However, the polarization direction and the propagation induced asymmetries for larger particles, break the spherical symmetry and distort the ideal 1:1 mapping from initial position to final momentum. A higher charge density in certain regions leads to a higher accelerating Coulomb force, which increases the absolute value of the final momentum (Fig. 3.8b,c). At the same time, inhomogeneous charge distributions accelerate the protons tangentially to the surface and alter the direction in the (θ, φ) -plane (Fig. 3.8a,b). In the case of complex charge distributions, the retrieval of the initial proton densities from the measured distribution is challenging since trajectories that originate from different spots on the surface may result in the same final momentum direction. In mathematical terms, the function between initial position and final momentum is not injective. However, in the case of the investigated nanoparticles this anomaly only occurs for regions with a low ionization yield, thus having a very small influence on the final momentum distribution.

The present description of the problem is based on the surface charge distribution. Here, this distribution is approximated by a linear combination of spherical harmonics $Y_l^m(\theta, \varphi)$ with order $l = [0; L]$. Since spherical harmonics in general are complex valued while the linear combination has to yield a real valued charge distribution, certain constraints are applied to the coefficients. Furthermore, the model assumes a symmetry plane spanned by the polarization and propagation axes. Due to those two conditions, $L(L + 1)$ coefficients are sufficient for a complete description of the surface charges. For simplicity we assume that the H^+ density ρ_{H^+} on the surface scales as $|E(\theta, \varphi)|^k$, where E is the electric field created by the surface charges and k is used as an additional fitting parameter. The electrostatic field E and the initial H^+ density ρ_{H^+} can be calculated from the nanoparticle surface charges and a trajectory analysis gives the final momenta of all probing ions. Finally, the momenta are projected onto the propagation and polarization

plane and compared with measured distributions. The Nelder-Mead simplex fitting algorithm [191, 192] is used to optimize all $L(L + 1) + 1$ variables in order to minimize the deviations between the measured momenta distributions and the ones calculated from the spherical harmonics model. The measure for the deviation is the sum over the squared differences in the momentum distribution.

For well-behaved problems, the surface charge distribution can be approximated by a linear combination of spherical harmonics up to the order L . With this approach the full charge distribution is expanded into multipoles. The iterative optimization algorithm retrieves the initial charge distributions and the order of the ionization process on the nanoparticle surface from the measured final momenta.

As a first step, we tested our retrieval algorithm on very basic charge distributions which could be described by spherical harmonics up to order $L = 2$. In this case, the algorithm converges reliably and is able to reconstruct the surface charges. A more detailed explanation of this reconstruction is given in Chapter A.1.4.

In the next step, the performance of the algorithm is tested in cases that do not allow a perfect retrieval. The surface charge distribution is chosen to contain higher order moments that are described by $L = [0; 4]$. There are high charge densities under an angle of 45° caused by the $L = 4$ contribution (Fig. 3.9a). Since the projected final H^+ distribution suppresses some of the higher order features (Fig. 3.9b), the algorithm manages to find a good agreement in the H^+ distributions – even if restricted to a maximum of $L = 2$ multipole orders (Fig. 3.9c). Accordingly, the retrieved charge distribution (Fig. 3.9d) resembles the overall reference distribution, but misses some of the higher order features. Since the electric fields around the investigated nanoparticles and the measured ion distributions show no such higher order contributions, the following analysis is performed with $l = [0; 2]$ spherical harmonics.

As a last step, the method was tested on the measured momentum distribution in Fig. 3.5 and enables the extraction of charges generated on the SiO_2 nanoparticle. The agreement between the measured and fitted momenta is conclusive (see Fig. 3.10a,b).

To summarize, the inversion method facilitates the retrieval of the surface charge distribution represented by a linear combination of spherical harmonics. The optimization algorithm varies the expansion coefficients together with the order of the dissociative ionization process. The retrieved set of optimized parameters is in good agreement with the charge distribution and dissociation rate calculated using full M^3C -simulations (Fig. 3.10c).

3.6 Conclusion

The nanoTRIMS is designed to investigate molecular reactions on nanoparticles and utilized for an experimental study in the strong-field regime. The results show that protons from the dissociation of molecular adsorbates on nanoparticle surfaces can serve as a probe for both the surface charge distribution induced by the near-field of nanospheres and the

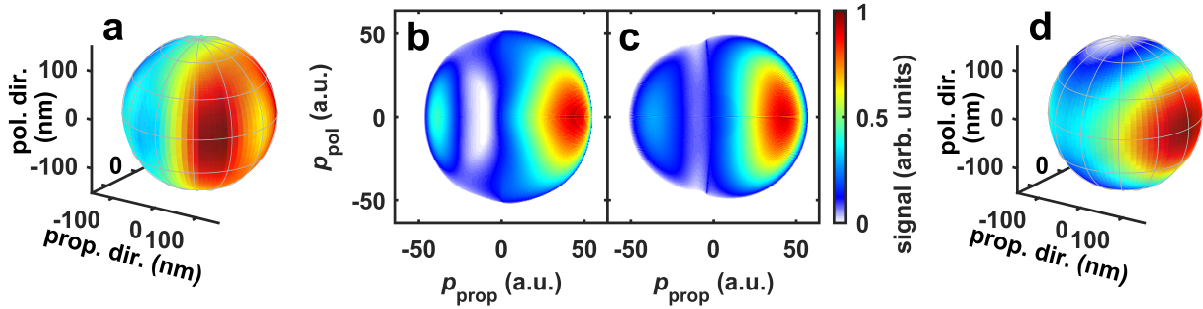


Figure 3.9: Inversion method. a) The initial surface charge distribution is described by spherical harmonics of order $L = [0; 4]$. The charge density on a 300 nm particle is encoded in the color scale. b) According to this charge distribution, the protons are generated on the surface and propagated in the static fields. The expected final H^+ momenta is projected onto the polarization and propagation plane. c) The fit is performed with the orders $L = [0; 2]$ and the final H^+ momenta are shown in projection. d) The retrieved initial charge distribution is shown on the surface of the nanosphere.

resulting spatially-dependent dissociative ionization yield. On the one hand, these results confirm the asymmetric, laser-induced shape of the electric field around spherical particles. On the other hand, they show that the size-dependent distributions can be utilized to control surface charge formation and ion propagation on sub-wavelength scales.

Quantitative agreement with the experimental data is obtained from semi-classical Monte-Carlo-simulations that incorporate the near-field, the rate of the dissociative ionization, and many-particle charge interactions. The employed simulations give deep insight into the several time scales that govern the dynamic behaviour. The fast electron emission is disentangled from the observed proton propagation. The detailed fully dynamical calculations help to extract the important aspects of the proton emission and to establish a mapping between the laser-induced surface charges and the measured momenta. This basic mechanism and the overall momentum gain are also accessible with a much simpler model based on charge repulsion in an electrostatic field, which enables the reconstruction of the charge distribution and dissociation probability from the measured data.

In the future, reaction nanoscopy opens the door for the spatially resolved study of nanoparticle photochemistry. Specially designed molecules might serve as wavelength-sensitive target for chemical reactions or tailored nanoscale geometries determine the local surface charge distribution. Additionally, the temporal resolution of chemical reactions may be realized by time-resolved pump-probe implementations.

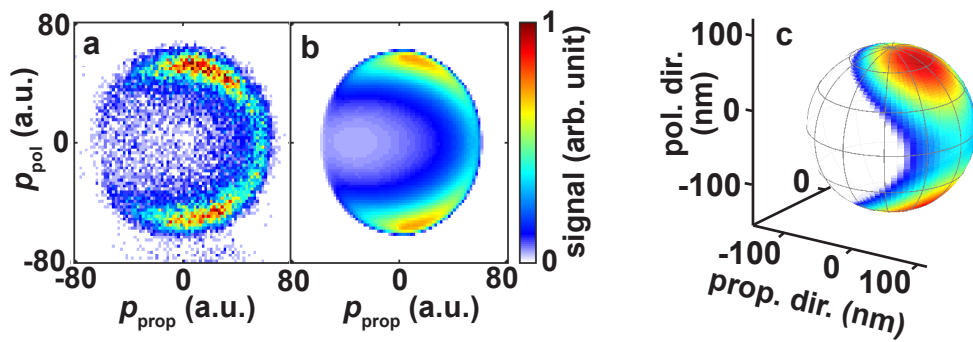


Figure 3.10: Fitting of dissociation yield to experimental data. a) The proton momentum distribution of the experiment with 300 nm SiO_2 particle is projected onto the polarization and propagation plane. b) The momentum distribution of a) is fitted by a simple model ($L = 2$, description see text) and the retrieved projected distribution is shown. c) The retrieved surface charge density for the parameters of the best fit is visualized on the surface of a nanoparticle.

4 Plasma expansion of nanoparticles

4.1 Introduction to x-ray free-electron laser experiments

The emergence of XFEL facilities has established a whole new field of imaging ultrafast processes on nanometer scales during the last decades. The combination of a femtosecond sub-nanometer wavelength pulse with the high photon flux allows the investigation of effects that have not been accessible experimentally yet. The ultra-intense pulses are capable of highly ionizing atoms and molecules [193], for example completely ionizing neon [194]. Furthermore, XFEL pulses enable one-photon pump-probe experiments in XUV range [195]. In recent studies the ablation from substrates [196], phonons in nanocrystals [197], and the microscopic response to elastic stress in metals [198] were all sampled with picosecond resolution. Another application of XFEL lasers is the observation of structural changes in proteins [199], or changes in the molecular order during phase transitions of liquid water [200].

Strong laser pulses with intensities above 10^{15} W/cm² deposit large amounts of energy in nanoparticles. They are capable of ionizing even materials with low absorption cross sections multiple times and form a dense plasma. The observation of such dense plasmas is challenging and mostly relies on indirect methods such as the detection of the released charges after expansion [174] or emitted radiation. Gorkhover et al. [201] demonstrated that it is possible to track structural changes in Xe-clusters upon ionization with intense laser pulses. The clusters with sizes between 15 nm and 30 nm clearly show a change in scattering images from the XFEL laser pulse, depending on the delay relative to the IR pump pulse. The quantitative analysis reveals that the density profile of the induced plasma is modified over time starting from the surface of the cluster. A comparison to theoretical one-dimensional models confirms the expansion of the surface plasma layer into the vacuum. However, a quantitative analysis of the plasma dynamics on the femtosecond scale is difficult due to the hardly known initial cluster shape and size.

The present study was conducted within a collaboration between the groups of Thomas Fennel, Matthias Kling, Artem Rudenko, Christoph Bostedt, Daniel Rolles, Carlos Trallero, Eckart Rühl and Markus Gallei. In this framework, an XFEL diffractive imaging technique is applied to a system with well-defined conditions. The comparison to time-dependent three-dimensional numerical simulations allows to track the plasma expansion in real time.

4.2 Interaction of strong fields with nanoparticles

4.2.1 Previous theoretical work

The plasma dynamics was modelled theoretically prior to the experiments [202]. The corresponding model for the plasma expansion uses a special microscopic particle-in-cell (MicPIC) technique [203, 204], which is able to treat both the atomic-scale plasma fluctuations and the interaction of electric fields with the plasma, i.e. the IR pulse propagation. The efficient numerical calculation of the MicPIC model is achieved by limiting the particle interaction distance. This numerical constraint ensures that the computational time scales linear with the particle number. At the same time, the electric fields can be propagated on a relatively coarse grid which is much larger than atomic distances. The model system investigated in the present work is implemented by a hydrogen cluster with a 50 nm diameter. The cluster is ionized by a 10 fs 800 nm IR pulse with an intensity of 10^{15} W/cm². The model includes both tunnel and impact ionization which lead to a fully ionized plasma.

Right after the ionization by the laser pulse, the plasma begins to expand radially. On average the expanding plasma contains about 80 eV of kinetic energy per atom. During this expansion the plasma is imaged by a second 10 fs 10 nm XFEL pulse with an intensity of 10^{16} W/cm². MicPIC simulations confirm that the interaction of the probe pulse with the plasma is negligible since it does not disturb the dynamics. The scattered light from the XFEL pulse is recorded on a detector behind the interaction region. The wavelength of the inelastically scattered light is a good measure for the plasmon energy $\hbar\omega_{\text{pl}}$ and consequently the electron density [205, 206]. Since the inelastic signal is not sensitive to spatial changes of the plasma, the following analysis focuses on the elastically scattered fields that are several orders of magnitude higher in signal. The elastic signal exhibits regular fringes with decaying strength for higher scattering angles. For negative delays, i.e. an unpumped particle, the scattered signal follows exactly the Mie-solution of a spherical particle. In the present work, a clear connection between the observed fringes and the charge density in the plasma is established.

During the interaction with the ionizing IR pulse, the electrons follow the oscillations of the laser field along the polarization direction. The oscillations leave the surface ions around the particle poles unscreened and allow them to escape the plasma quickly due to Coulomb repulsion. After the plasma-IR interaction, electrons and ions screen each other and expand on the same timescale, which is called hydrodynamic cluster expansion [207, 208]. The evolution for different delays is shown in Fig. 4.1. In the upper subfigure, the rapid ion repulsion is clearly visible while for later delays the ion and electron profiles match each other. Most importantly the electron densities of all delays and directions can be described by a modified Fermi distribution

$$n_e(r) = \frac{n_c}{\left(\exp\left(\frac{r-r_c}{ds}\right) + 1\right)^s} \quad (4.1)$$

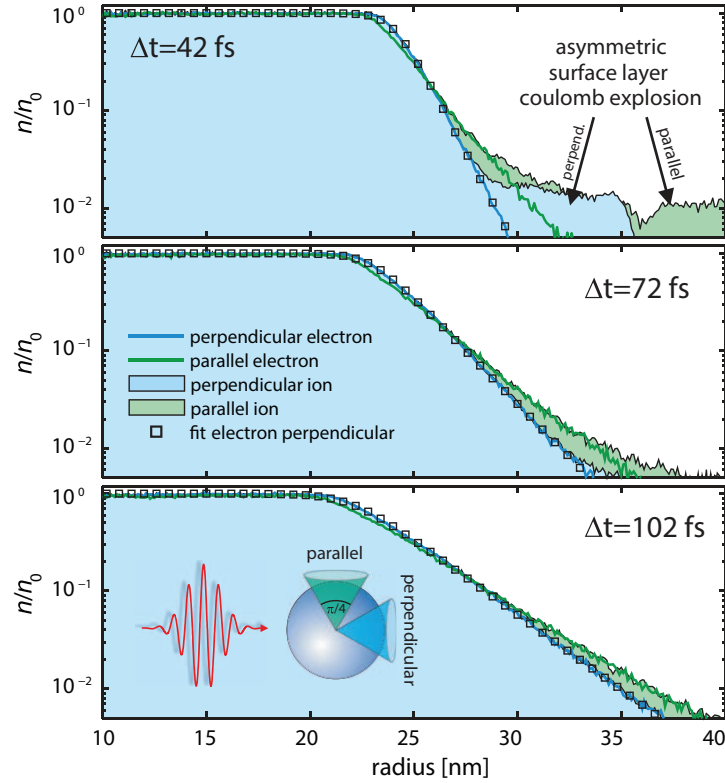


Figure 4.1: Radial density profile. The graphs show the radial density profile of ions (area) and electrons (solid line) for three time delays as indicated. The direction parallel to the laser polarization is illustrated in green, the perpendicular direction is illustrated in blue. The data is retrieved from MicPIC simulations. As an example the perpendicular electron density is fitted with Eq. 4.1. Figure is taken from Ref. [202].

with the constant core density n_c , the core radius r_c , the surface decay length d and the factor s , which describes the sharpness around the core radius. A fit of this function shows that s converges to a constant value for all delays. It is possible to describe the complete dynamics with two time-dependent parameters, r_c and d .

4.2.2 Elastic scattering

The angular resolved scattered XFEL light from the dense plasma is a practical observable, which is accessible not only in simulations but also experimental measurements (see Chapter 4.3.1). The MicPIC model calculates the scattered fractions for all delays and shows two noticeable features:

- a) The intensity of the higher order fringes drops with increasing delay. This is a result of the slope in radial plasma density, which becomes less steep. In other words, the surface layer of the nanoparticle plasma softens with time.

- b) The spacing of the fringes increases with delay. This change in spacing corresponds to the radius of the sphere that is getting smaller with time. This observation seems to contradict the expected plasma expansion.

Fig. 4.1 shows that a simple analytical function is sufficient to approximate the electron density. The density profile from eq. 4.1 can be used to calculate the scattering signal in Born approximation, i.e. small scattering intensities. Peltz et al. [202] confirm that the MicPIC scattering signal is in excellent agreement with the Born approximation results. Thus, it is possible to use the parameters r_c and d given by the fitted density profile to explain the two effects mentioned above. The drop in signal strength of higher order peaks is related to a more shallow density profile, expressed by an increase of the decay length d (see Fig. 4.2b). The larger fringe spacing is a consequence of a decreasing core radius r_c (see Fig. 4.2a). While the outer edge of the plasma is driven away from the center, the XFEL pulse images the intact core with unchanged initial density n_c which shrinks in size after plasma creation. The sharpness parameter s is set to 0 without any loss of information.

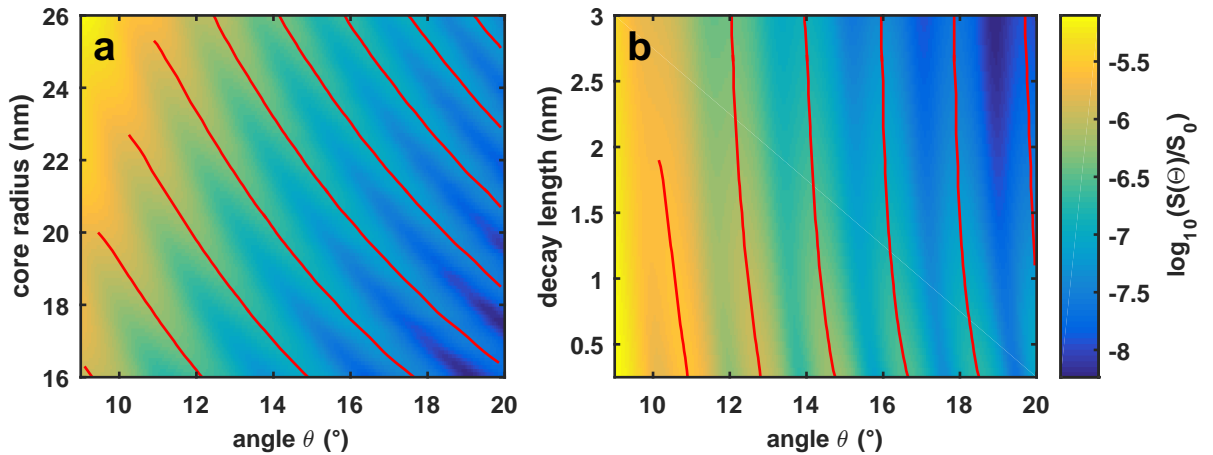


Figure 4.2: Scattering patterns. The elastically scattered 1.5 nm light is calculated for a set of fit parameters r_c and d that describe the electron density function in Eq. 4.1 with $s = 0$. The scattered signal is evaluated in Born approximation and plotted over the scattering angle θ . In a) the core radius r_c varies between 16 nm and 26 nm whereas the delay length d is kept constant at 2 nm. The spacing of the fringes strongly depends on the core radius. In b) the delay length d varies between 0.25 nm and 3 nm whereas the core radius r_c is set to 23 nm. The spacing in this plot only changes weakly with d . The graph is modified for larger spheres and smaller wavelengths after [202].

The scattering fringes are calculated in Born approximation for a set of parameters that are sufficient to describe the plasma density profile. In the following sections, a fit to experimental results establishes the important link between the scattering images and the plasma density.

4.3 Experimental Results

4.3.1 Setup

The experiment was performed at the Linac Coherent Light Source (LCLS) at the SLAC National Accelerator Laboratory (SLAC) at Stanford University in Menlo Park, California. The working principle of XFEL is based on the single pass amplification of x-ray radiation and delivers beams of unprecedented brightness [209–211]. The first step of a free-electron laser (FEL) is based on the acceleration of a ~ 250 pC electron bunch in linear accelerators up to electron energies of a few GeV. Behind this stage, an undulator creates a spatially varying magnetic field with a periodicity on the centimeter range. The magnetic field created in the undulator with strengths of around 1 T forces the electrons on a sinusoidal path. The electrons emit electromagnetic radiation due to the acceleration during each half cycle [212]. Second order effects in the equations of motion lead to a microbunching of the electrons in the undulator. They are grouped together in a periodic order which ensures the spatial coherence of the emitted radiation. Due to the start of the amplification process from spontaneous emission, this unseeded operating principle is called self-amplified spontaneous emission (SASE) [213–215]. Since the SASE process is based on statistical noise that is further amplified, it is prone to intrinsic fluctuations of wavelength and pulse energy. Furthermore, the temporal coherence is usually limited to less than the temporal pulse duration [216, 217]. In order to overcome these limitations, other techniques that involve the seeding of an XFEL have been demonstrated. The HHG of an optical laser may act as a seed pulse for the amplification in an FEL [218, 219], which is limited by the wavelengths that can be generated efficiently in the HHG process. Alternatively, a first undulator produces radiation at the desired wavelength that is filtered in a monochromator afterwards and is used as a seed in the second main undulator. This method is called "self-seeding" of an FEL [220–222].

While the LCLS facility provides laser beams with photon energies ranging from 280 eV up to 11.2 keV [223], even optical frequency or terahertz FEL's are available [224]. For the experiment of the present work, photon energies of 800 eV are used, which corresponds to a wavelength of around 1.5 nm. The XFEL pulse duration is around 60 fs with pulse energies of a few mJ. The FEL acts as a probe and is focused to a spot size of $5 \mu\text{m}$ ($1/e^2$), see Fig. 4.3.

Propagating collinearly with the XFEL, the 50 fs IR pump laser with 10 mJ pulse energy is focused to a spot size of around $50 \mu\text{m}$ ($1/e^2$) ensuring intensities up to 10^{16} W/cm^2 . The focal width of the IR is kept one order of magnitude larger than the FEL focus, in order to avoid any undesired focal averaging by keeping constant pump conditions for the complete probed volume (Fig. 4.3). The pump laser ionizes isolated 127 nm SiO_2 nanoparticles that are dispersed in H_2O and aerosolized in a gas stream of nitrogen. The nanoparticles exhibit a narrow size distribution (see Chapter 3.2.3 and A.1.3) which ensures controlled and constant initial conditions throughout the scattering experiment. The nanoparticle

source described in Chapter 3.2 was used to inject the particle into the center of the AMO experimental chamber [225].

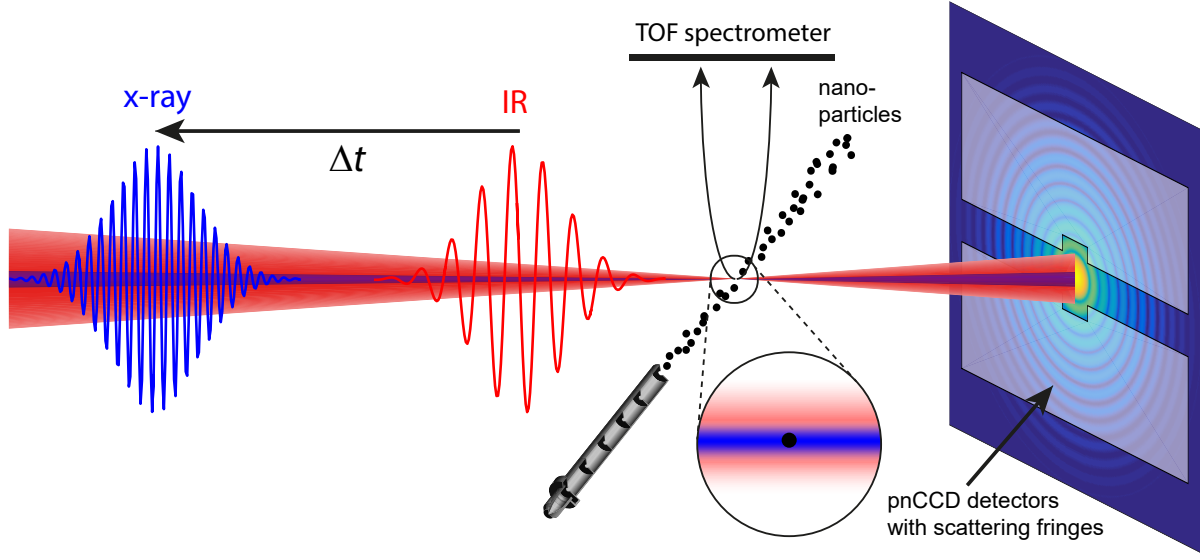


Figure 4.3: Experimental setup of plasma imaging experiment. The IR pump pulse generates a plasma in a SiO_2 nanoparticle which is probed by a delayed XFEL pulse. The scattered light images the plasma distribution at the delay Δt and is recorded on a pn-junction charge-coupled device (pnCCD) detector. The pump focus is much larger than the FEL focus in order to keep a constant pump intensity across the imaged volume. The nanoparticle source delivers a jet of free particles into the interaction region. An ion TOF is placed perpendicular to the laser propagation direction to record the emitted ions from the nanoparticle.

The inherently large jitter of a few hundred femtoseconds between XFEL and IR can be circumvented by measuring the actual time delay shot-to-shot. The Time-Tool (TT) placed after the endstation exploits transient reflectivity changes in silicon nitride thin films and is able to determine the time delay on a femtosecond scale [226]. The TT itself is calibrated measuring the ratio between $\text{N}_2^{2+}/\text{N}^{2+}$ for several delays between the two pulses [227]. As a conclusion, our temporal resolution is limited by the pulse lengths. The scattered x-rays are recorded with a 1 Megapixel pnCCD detector (two halves with $76.8 \text{ mm} \times 38.4 \text{ mm}$ each) at a position 20 cm behind the interaction point [228]. Since the central part is cut out to let both pulses pass through undisturbed, the detector does not cover angles below $\sim 1.5^\circ$.

4.3.2 Comparison with MicPIC model

By using SiO_2 with about 5 times the size of the modelled hydrogen clusters, the generated plasma is not fully ionized and still contains bound electrons. However, the laser intensity

used in the experiment was at least as high as considered in the model calculations. The high intensity ensures efficient tunnel ionization and creates enough free electrons driving the hydrodynamic expansion. It is viable to use the same analytic density profile from Eq. 4.1, since the initial geometry is spherical in both cases and the expansion dynamics is driven by the same forces. Due to the higher mass of SiO_2 compared to H, we expect the same plasma behaviour on a slower time scale. For this reason, 50 fs pulses are sufficient to resolve the dynamics. The smaller wavelength of the probing beam compared to the model study results in a better resolution of the imaged plasma and increases the number of fringes observed on the detector. The pixel size is small compared to the width of a single fringe, which ensures a clear separation of scattering maxima.

4.3.3 Analysis of scattering images

The target density in the interaction is limited by the working principle of the nanoparticle source leading to about one nanoparticle hit every ten shots. A higher count rate leads to an undesired increase of laser shots with two or more particles at the same time. The two dimensional scattering images make it possible to easily separate single nanoparticles with a rotational symmetric signal from nanoparticle clusters with additional non-symmetric fringes imprinted onto the single-particle image (see Fig. A.4). All single particle hits are binned according to the delay measured in the time tool and analyzed as follows: Since both halves of the detector can be moved separately, the scattering image itself is analyzed in order to retrieve the alignment of the upper half with respect to the lower half (see Fig. 4.4a). Overall the detectors cover a scattering angle from 1.7° to 9° . For each image the the signal is averaged over all angles. The radial distribution is fitted by the calculated scattering fraction in Born approximation (see Fig. 4.4b). The fit retrieves the two essential parameters, core radius r_c and delay length d , describing the electron density (Eq. 4.1) in the plasma. In Fig. 4.4c we compare the radial scattering fits for three delays, showing the difference between an intact particle, the plasma right after ionization and an expanded plasma right before the complete disintegration. All signals are normalized to 1 and show a clear decay for higher scattering orders with increasing delay. Following the same trend the spacing between the fringes is increased for the yellow curve.

The single shot detection scheme allows us to track the plasma expansion with femtosecond resolution. For each time bin, the electron density can be approximated by the averaged retrieved fit parameters. The delay-dependent parameters $r_c(\tau)$ and $d(\tau)$ describe the temporal evolution of the plasma expansion. Triggered by the ionization of the nanoparticle, the decay length gets larger indicating the "softening" of the surface. The outermost layer of ions gets ejected and thereafter the electrons as well as the surface ions follow flattening out the edge around the core. While this expulsion increases the outer radius defined by the fastest charges it also decreases the inner core radius. Shortly after the ionization the increasing fringe spacing indicates a shrinking core, visualized as a melting of the surface layer.

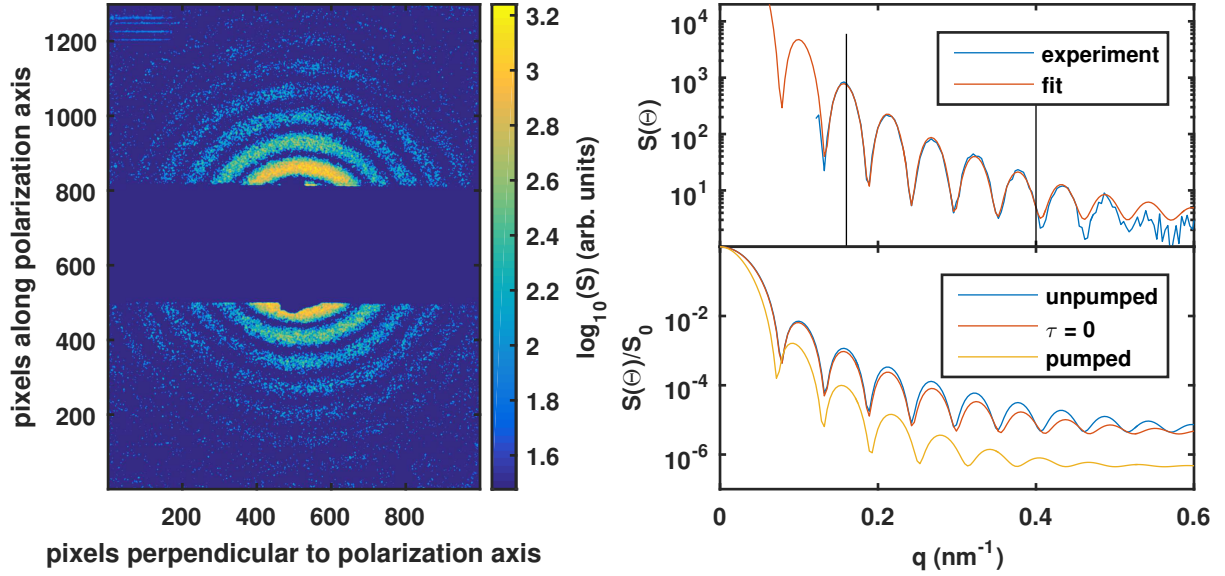


Figure 4.4: Analysis of experimental scattering images. a) The scattering image was recorded at LCLS with 1.55 nm XFEL pulses. The targets were 127 nm SiO_2 nanoparticles. This image shows an unpumped particle for a clear demonstration of the retrieval steps. The detector is placed about 200 mm behind the interaction region and has a gap in the center in order to let both laser pulses travel through and to avoid the most intense stray light at small angles. The two half-planes are aligned with respect to each other to get a good radial overlap. b) The radial signal is averaged over all angles (blue) and plotted over the scattering vector q . Eq. 4.1 is used to fit the calculated scattering signal to the experimental value (red). c) The fitted scattering curves are normalized to the maximum value at $q = 0$ and compared to each other. The three plots refer to three different delays: One unpumped particle (blue), one particle right at the interaction with the IR pulse (red) and one particle a few hundred femtoseconds after plasma creation (yellow).

4.4 Conclusion

The imaging of plasma expansion proves that XFEL lasers are of major importance for the investigation of ultrafast dynamics with nanometer resolution. The possibility to confine high intensity x-ray pulses enables the imaging of a non-equilibrium state with a single shot. The corresponding nanoplasma expansion experiment is performed under well-defined conditions, which include the exact initial size and spherical shape of the plasma, the reproducible ionization intensity, and the delay between pump and probe pulse. Due to this prerequisite in the measurement, we are able to quantitatively compare the retrieved experimental results to advanced MicPIC simulations. The convincing agreement with the theoretical model verifies that the predictions apply to the experimentally observed plasma

dynamics. Due to the generality of the model our results can be transferred to other cases of plasma dynamics that occur on different timescales or in other geometries.

5

Photoemission time delays of C_{60}

5.1 Introduction

Although the C_{60} molecule consists of 60 atoms of the same element, it exhibits a few very remarkable properties that are linked to the specific size and shape of this system [229]. The interaction of light with C_{60} answers many questions about the inner dynamics and reveals insight into its molecular structure. C_{60} possesses many symmetry axes and planes that cause a high energetic degeneration in the electronic ground state. In many theoretical approaches these manifold symmetries are exploited and C_{60} is approximated by a spherical molecule simplifying numerical calculations [230].

The 240 valence electrons of C_{60} can be excited resonantly by an external electric field and undergo plasmonic motion. The existence of this giant plasmon resonance was predicted almost 30 years ago [132] and shortly after confirmed experimentally [133]. A more detailed theoretical description of this plasmonic behaviour is given in Chapter 2.5. Here, a time-resolved experimental study on the excitation of this plasmon is presented.

5.2 Experimental setup for attosecond streaking measurements

An 800 nm, 6 mJ, 25 fs Femtopower 1 kHz amplifier is used as a laser source for the attosecond streaking experiments in collaboration with the group of Prof. Francesca Calegari at the Politecnico di Milano. The pulses are CEP-stabilized with residual fluctuations of ~ 200 mrad (rms) and sent into a hollow-core fiber with a pressure gradient along the propagation direction [231]. The spectrum is broadened to support 5 fs, 2.5 mJ pulses centered around 720 nm.

The XUV pulses are created by polarization gated HHG in krypton (Fig. 5.1) [232]. An aluminum filter behind the gas cell blocks the low frequency components up to 17 eV, including the fundamental IR frequency. Upstream of the HHG target, a fraction of the IR pulse is separated by a beamsplitter into a second arm that serves as the probe pulse. The temporal delay between the pump and probe pulse is controlled by a delay stage in the IR arm of the interferometer. To compensate for long term thermal drifts, the two arms are stabilized interferometrically by a continuous wave (CW) helium-neon laser. Both arms

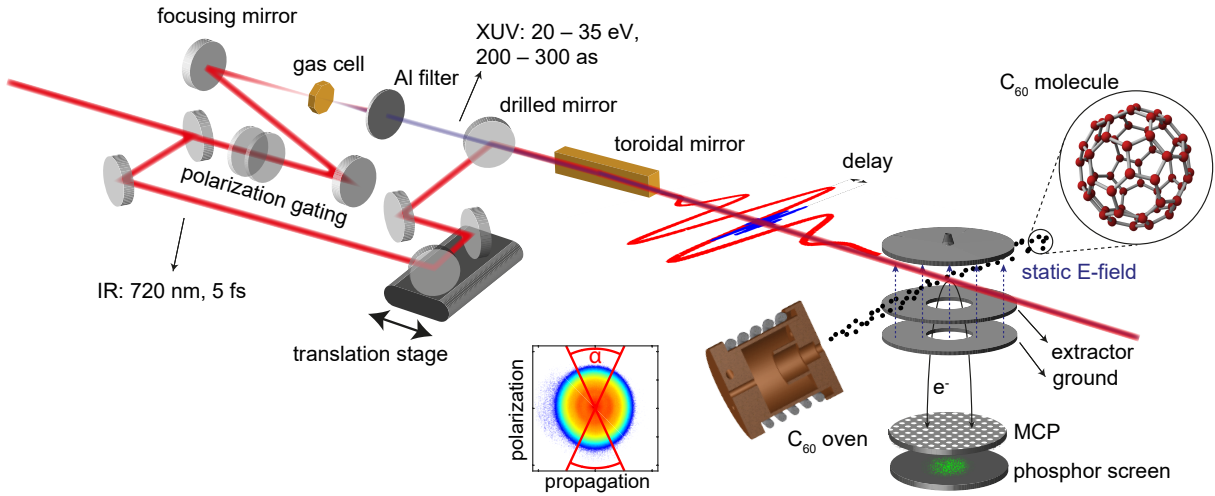


Figure 5.1: Experimental Setup. The IR pulse is split up into two arms: the probe pulse travels through a delay stage, the XUV pump pulse is generated in a HHG gas cell using polarization gating. Behind an aluminum filter the XUV pulse is recombined with the IR pulse on a drilled mirror and both are focused into the experimental chamber by a toroidal mirror at grazing incidence angle. The target C_{60} is provided by an oven filled with C_{60} powder and operated at $550\text{ }^{\circ}\text{C}$. The emitted electrons are recorded in a velocity map imaging (VMI) spectrometer (inset at bottom). The full angle for spectra recovery is indicated as $\alpha = 50^{\circ}$.

are recombined on a drilled mirror and a toroidal mirror in grazing incidence focuses the IR and XUV pulses into the experimental chamber with a focal length of 80 cm. Downstream of the interaction chamber the XUV spectrum is recorded in a spectrometer consisting of a grating, micro-channel plates and a phosphor screen. During each measurement, this spectrum is monitored in real time (Fig. 5.2a).

The C_{60} oven is located about 10 cm away from the interaction region perpendicular to the laser propagation direction. It is placed inside a heater element on an insulating ceramic and is heated up to $550\text{ }^{\circ}\text{C}$. A cooled housing encloses the oven and also acts as a 2 mm skimmer. The opening of the skimmer can be closed by a motorized steel plate which enables a fast switching between targets without cooling down the oven. Neon is filled into the chamber through a needle valve allowing the fine adjustment of gas pressure in the interaction volume. An electronically controlled valve allows to switch the gas target on and off within seconds.

The photoelectrons are detected in a VMI [233] spectrometer projecting the electron momenta onto the laser polarization (p_{pol}) and propagation (p_{prop}) plane. Further analysis is performed with spectra angularly integrated over a full opening angle of 50° along the laser polarization axis (inset in Fig. 5.1). In the current work, the VMI images are not inverted (as in Ref. [234]), in order to avoid additional noise and artifacts on the data. Due

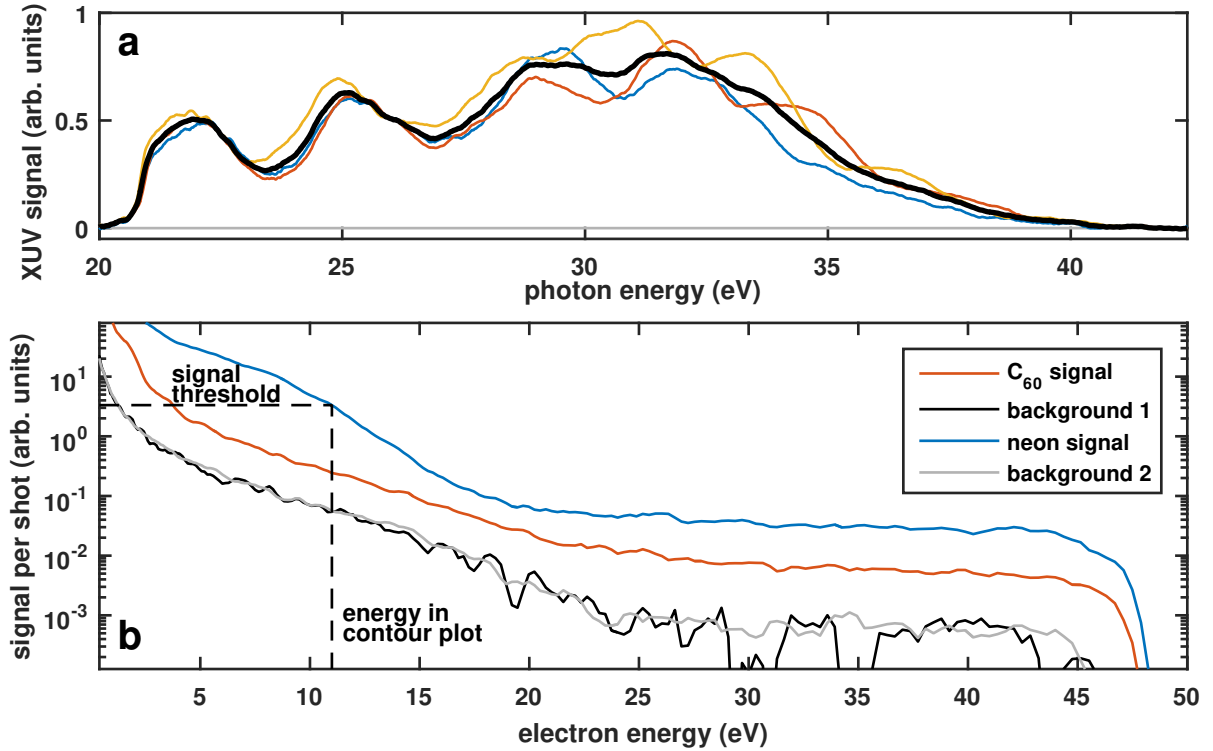


Figure 5.2: XUV spectrum and electron spectra of C_{60} and neon. a) The XUV spectra for three separate measurements are shown in blue, red and yellow. The average spectrum (black) reaches from 20 eV to 40 eV. b) Contrast between signal and background. The measurements for C_{60} (red) and neon (blue) are performed with the respective source switched on, solely. Each measurement is taken in alternation with a background recording where both sources are switched off for a few seconds. Background 1 (black) and 2 (gray) refer to the signal in between C_{60} and neon measurements, respectively. The difference between the two background measurements is the waiting time after the deactivation of the respective source.

to the XUV chirp as well as the broad XUV intensity and the C_{60} absorption spectrum, a direct conversion of the streaking delay from kinetic energies to photon energies would induce additional errors. The goal of this study is the comparison with numerical calculations, which can easily calculate the projected energy $E = (p_{\text{pol}}^2 + p_{\text{prop}}^2)/(2m)$, referred to as *electron energy*, unless otherwise stated. The maximum detectable kinetic energy amounts to about 50 eV.

In order to determine an absolute delay of C_{60} , a known reference target has to be streaked under the same experimental conditions, which include the CEP and the XUV spectrum. In previous experiments the electron emission from different states (Chapter 2.3) or a single-shot analysis [22, 234] is used to relate the investigated process to a well-determined reference. Since the ionization potential of C_{60} with 7.54 eV is comparably

low and the photoionization cross section is several electronvolts broad [133], it is almost impossible to spectrally separate the desired C₆₀ signal from any reference signal. Therefore, two separate measurements with each target are necessary to retrieve both a clear C₆₀ signal and the neon reference.

However, measuring attosecond delays with an interferometric setup is challenging, even with active stabilization of the two arms. Since the long-term drift of the interferometer may easily exceed a few attoseconds over the measurements time of around 100 min, an alternative to consecutive measurements is crucial for the success of the experiment. For this study, the implemented measurement scheme alternates between the two targets every ~60 s of measurement time. A single measurement consists of several delay steps with a separate neon and C₆₀ recording at each step. With this novel approach, the signals can be easily distinguished while the neon measurements provides a reliable reference for an absolute timing. Long-term drifts in the interferometer would be detected by a modulation of the streaking trace periodicity and could be used to correct the retrieved delay.

The choice for neon as a reference gas is partly based on the feasibility to perform accurate theoretical calculations for this noble gas and partly due to the ionization potential. If the ionization potential was too low, the ATI background from the IR laser increases and overlaps with the XUV photoelectron signal at low kinetic energies. The use of neon avoids this issue by suppressing the ATI background due to the high ionization potential. The cross section of helium with even higher ionization energies is lower compared to neon and would deteriorate the signal-to-noise ratio.

Thorough testing ensures that both targets are not detectable after closing the respective source (Fig. 5.2b). The good agreement between the two background traces (black and gray) leads to the conclusion that the residual signal is not influenced by neon or C₆₀. Krypton from the HHG process is assumed to be the main component in the background signal. Both C₆₀ (red) and neon (blue) show a signal that is at least one order of magnitude higher than the background over the full energy range.

5.3 Extraction of time delays

5.3.1 Spectrograms

For each delay step of 150 as, two measurements are recorded: one with the reference gas neon with at least 15000 shots and one with the sample C₆₀ with at least 60000 shots each (compare blue and red curves in Fig. 5.2). A complete run covers at least three optical cycles (~10 fs) and requires a stable CEP for more than one hour. Each measurement contains the two-dimensional electron momenta spectra that are angularly integrated (see Fig. 5.1) and further processed in the streaking analysis. In total, one run yields two delay-dependent photoelectron spectra for each target, that are referred to as *up* and *down* spectrograms (Fig. 5.3a,b).

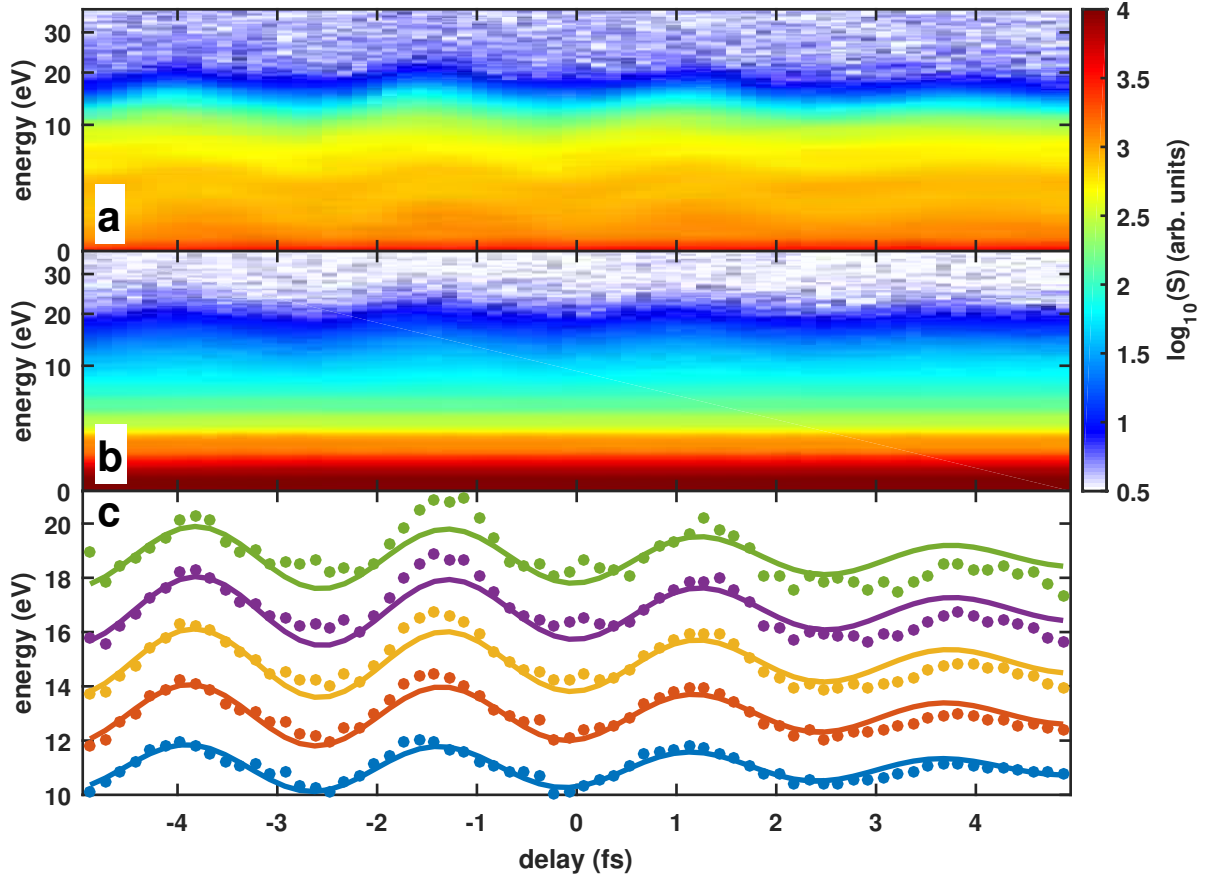


Figure 5.3: Spectrograms and contour lines. a) Spectrogram for neon measurement with 15000 shots for each of the 150 as delay steps. Full opening angle is 50° in one polarization direction. b) The same run as in a) for C_{60} and 60000 shots per delay. Both spectrograms show the up direction. c) An example of experimental contour points is retrieved from a) and plotted between 10 eV and 20 eV. The lines are fit functions to the points as explained in the text.

The spectrograms show the oscillations of the electron momenta with the vector potential of the streaking IR laser field. Due to the better contrast, the delay scans focus on the central part of the few-cycle laser pulse in our measurements. In Fig. 5.3a,b the IR laser pulse is centered at a delay around -1.5 fs with the three main peaks clearly visible. For larger delays, i.e. the XUV pulse is arriving before the IR pulse, the oscillations vanish. All measurements contain several oscillations to ensure a proper retrieval of the investigated delay.

Both the ionization process itself and the propagation of the photoelectrons cause deviations from the ideal streaking described by Eq. 2.7. In order to quantify those deviations and to gain insight into the polarizability of C_{60} , the oscillations are comprehensively evaluated by the extraction of contour lines at different energy ranges. A constant signal

threshold is matched at a certain energy for each delay (see visualization by the dashed line in Fig. 5.2). The resulting energy values are plotted as dots in Fig. 5.3 for five exemplary signal thresholds. This analysis is performed for both samples (neon and C₆₀) and both polarization directions (up and down). All contour points are fitted by the function

$$E(\tau) = A \exp \left(- \left(\frac{\tau - t_0}{\sigma} \right)^2 \right) \sin(\omega\tau - \phi) + E_0. \quad (5.1)$$

Because of their relation to the IR laser pulse, the fit parameters t_0 , σ and ω are assumed to be the same throughout one run. The parameters A , E_0 and ϕ are fitted individually for each contour line. For further analysis, the energy dependent streaking delay $\tau_S(E_0) = \phi/\omega$ is used.

In Fig. 5.4a the experimental streaking delay for neon is shown for an energy range from 8 eV up to 23 eV. The lower limit is given by the spectral overlap with the constant IR background, while the highest energy is defined by the XUV cutoff minus the ionization potential of neon ($I_{p,\text{Ne}} = 21.6$ eV). The error bars indicate the confidence interval of ϕ in the fitting function, the confidence interval of ω is small in comparison. Parts of the streaking delay in neon can be attributed to the interaction of the atom with the IR or XUV light, i.e. the intrinsic EWS delay is associated with the ionization process itself, while CLC and DLC are related to the influence of the streaking field. In addition to the latter effects, the chirp of the XUV pulse causes a delay in streaking, which is purely determined by the properties of the pump pulse. Due to the generation process, the XUV pulses are positively chirped and a 100 μm aluminum filter with negative group delay dispersion (GDD) does not fully compensate the dispersion [68]. A zero-dispersion pulse is not feasible because the required thickness of aluminum does not transmit a sufficient amount of XUV light for the streaking experiments.

The analysis of the neon reference measurement determines all laser related effects (performed in Chapter 5.4.4) and separates them from the mentioned intrinsic EWS delays. Fig. 5.4b shows the delays of the C₆₀ measurement (Fig. 5.3b) that was recorded together with neon in one run. Especially at high energies, the C₆₀ streaking delay seems to follow the trend of the neon delay. However, some prominent differences in the delay are visible at lower energies. Furthermore, the delay extraction for C₆₀ shows smaller error bars above 20 eV due to the lower ionization potential compared to neon.

While the absolute timing of both measurements is not known individually, the alternation between the targets ensures that they share the same time zero. Any shift cancels out in a differential plot of streaking delays (Fig. 5.4c). The difference between C₆₀ and neon delay is calculated for four different runs with two directions each, i.e. eight spectrograms in total. The average delay of all eight spectrograms is calculated as the arithmetic mean weighted with the inverse error value of each curve. This experimental delay curve forms the basis for a further comparison with theoretical calculations.

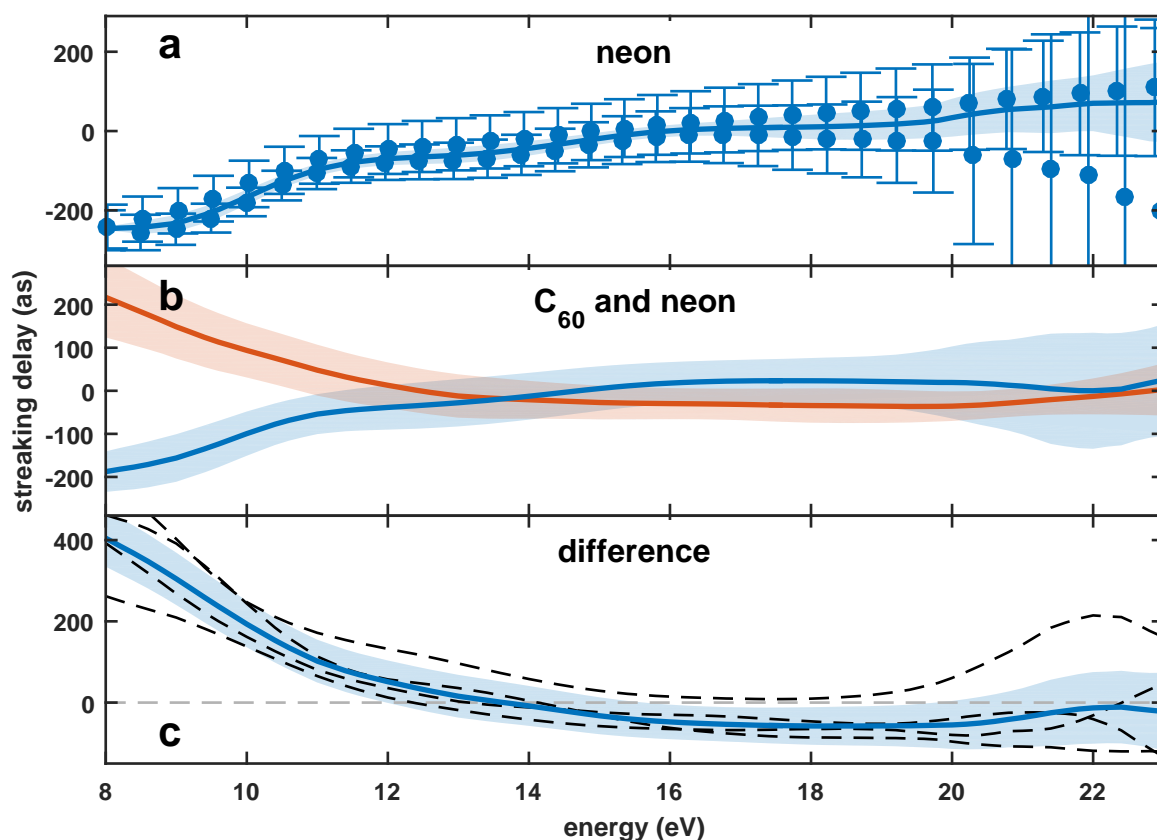


Figure 5.4: Experimental streaking delays. a) Streaking delays are shown for one neon measurement. The circles with the error bars indicate the obtained delays for both directions including the fitting confidence interval. The solid line with the shaded area shows the weighted average and standard deviation. b) Neon (blue) and C_{60} (red) are retrieved separately from one measurement. c) For each measurement the difference between the two samples is calculated (black dashed lines). The weighted average and standard deviation of the four considered measurements is shown in blue.

5.4 Theoretical model of C_{60}

5.4.1 TDLDA calculations

The TDLDA calculations in this section are performed in collaboration with Prof. Himadri Chakraborty and Prof. Maia Magrakvelidze and follow the description given in Chapter 2.5 delivering the EWS delay and the cross section of $k = 11$ C_{60} states with ionization energies $I_{p,k}$ between $I_{p,1} = 28.5$ eV and $I_{p,11} = 7.6$ eV corresponding to the highest occupied molecular orbital (HOMO).

5.4.2 Monte Carlo simulation

The interaction of the XUV pump pulse with C_{60} is treated by the TDLDA calculations that include all delays arising from plasmonic effects or short-ranged potentials. In order to compare the theoretical model with the experimental results, CTMC simulations are performed. They cover the effects associated with the XUV chirp and spectral bandwidth, IR laser interaction, long-range potentials and the detection scheme that projects the final momenta.

Basic neon simulation

In order to visualize the mentioned effects separately, a very fundamental simulation illustrates the effect of the CLC term of Eq. 2.10 on the streaking delay. This exemplary simulation is performed for neon with a Gaussian spectrum centred at 40 eV and without additional EWS delay. In order to avoid additional convolutions due to the projection, the spectrum here is plotted as the kinetic energy measured in a small opening angle TOF along the polarization axis for once (Fig. 5.5a). In this case, the electron energy is equivalent to the photon energy shifted by the ionization potential. The streaking delay is straight-forward to retrieve and is compared to analytical calculations.

The retrieval of the streaking delay from spectrograms uses the same algorithms as already introduced for the experimental analysis (Chapter 5.3) and results in a smooth curve for the streaking delay (blue line in Fig. 5.5c). This result does not depend on the actual target or spectrum and is fully attributed to the Coulomb field and its interaction with the streaking laser field (black dashed line from Eq. 2.10). In all delay plots the shaded area visualizes the confidence interval of the fit and gives an estimate of the accuracy of the plotted lines. Importantly, the deviation between the retrieved delay from the CTMC simulations and the analytical function is around 5 as, which is well below the estimated error in the experiment.

The spectrogram in Fig. 5.5b is retrieved from the same simulation as in Fig. 5.5a, yet the projected energy is plotted as measured in a VMI detector. The retrieved streaking delay is shown in Fig. 5.5c (red line). Comparing the two lines, the TOF and VMI results are almost identical at high energies, since the projection in the VMI has no effect for high energy electrons. At projected energies close to the cutoff, there is only one possible direction of emission, which is parallel to the polarization. Below this region, electrons with different kinetic energies – and thus different streaking delays – may get projected onto the same detector position, which distorts the final delay curve. Moreover, the contour determination gets difficult around energy ranges with a flat spectrum, which increases the uncertainty of the final fit. To a small extent this artifact is also observed in the TOF calculation around the electron spectral peak (18.4 eV).

In addition to the projection of kinetic energies in the VMI detection, the final electron kinetic energy distribution depends on the initial XUV spectrum. Fig. 5.6 demonstrates the effect of the experimental spectrum from Fig. 5.2a on the final delay. Here, the EWS

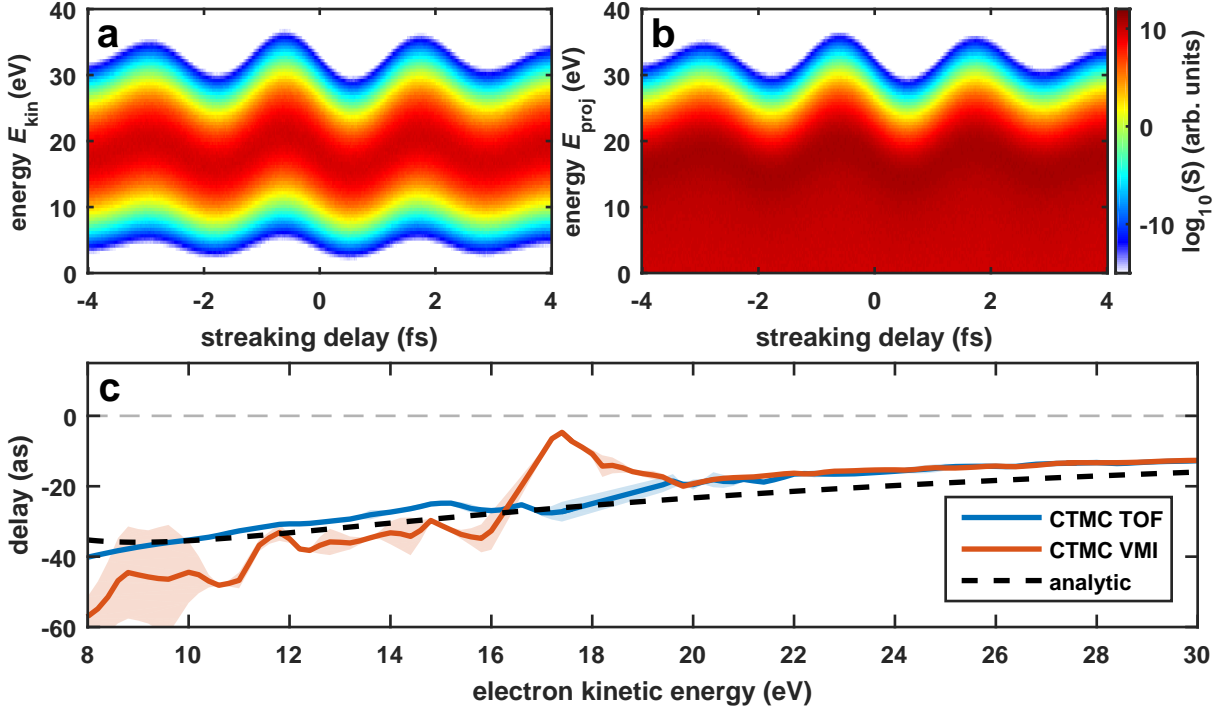


Figure 5.5: Simulated streaking delay of neon. a) Spectrogram of neon streaking with a Gaussian XUV spectrum centered at 40 eV. The emitted electrons are recorded in polarization direction by a TOF detector and plotted as kinetic energy $E_{\text{kin}} = p^2/(2m)$. The EWS delay is set to zero here. b) The same simulation as in a) is plotted for a VMI detection with a 50° full opening angle for integration with the projected energy $E_{\text{proj}} = (p_{\text{pol}}^2 + p_{\text{prop}}^2)/(2m)$. c) The retrieved energy dependent delays from a) and b) are plotted in blue and red. As reference the analytical delay for CLC is plotted in black (dashed).

delay and the GDD of the XUV pulse are set to zero. Due to the XUV cutoff around 40 eV, the delay extraction is only possible for kinetic energies up to around 20 eV. Below 10 eV photoelectron energy, the spectrogram is modulated by the peak structure in the XUV spectrum (see Fig. 5.2). In the experimental spectra this part is superimposed by neon ATI features.

To summarize, the effect of the projection in the VMI emerges only at lower energies and is not present close to the cutoff. Due to the same treatment of data in experiment and simulations this influence can be neglected. The broad XUV spectrum leads to a *mixture* of different photon energies on the final photoelectron energy scale. This entanglement complicates the interpretation of energy dependent delays, but is completely considered in the theoretical analysis.

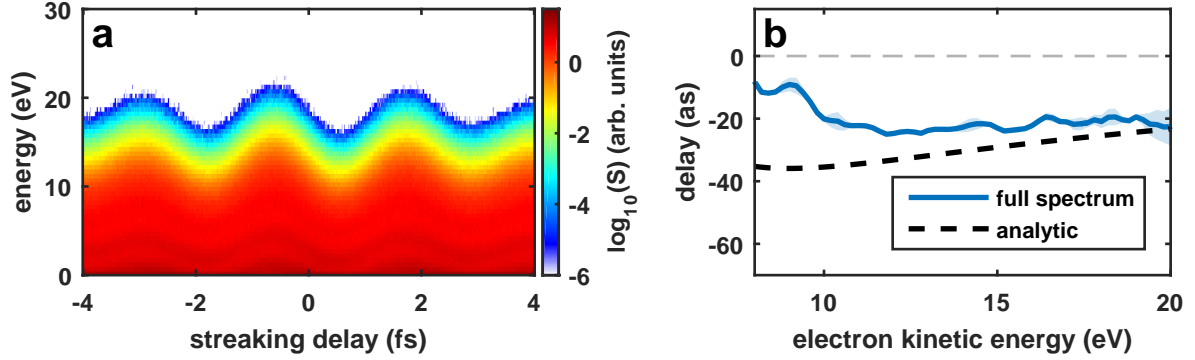


Figure 5.6: Effect of XUV spectrum on neon delay. a) The spectrogram is calculated for a streaking experiment that uses the XUV spectrum from Fig. 5.2a and an electron detection in a VMI spectrometer. To support a straightforward comparison with Fig. 5.5, the XUV chirp and the EWS delay is neglected here. b) The energy-dependent delay is retrieved by fitting of contour lines from a). The analytical delay due to CLC is shown in black (dashed).

Ionization step

After the short comparison of different detection methods (TOF and VMI) and the influence of the XUV spectrum on the delay extraction, the fundamental steps in the Monte-Carlo simulations will be explained in more detail.

Independent of the temporal delay between pump and probe pulse, the ionization probability for each photon energy is proportional to the spectral XUV intensity and the absorption cross section of the investigated target. Consequently, the ionization from the different electronic states is sampled according to their partial cross section at this photon energy. The electron birth time of the ionization from one state is sampled by a Gaussian XUV pulse with a temporal pulse length of 250 as. Moreover, both the XUV chirp and the EWS delay of the respective state induce an additional temporal shift of the electron birth time. Initially, the electron has a kinetic energy of $E_{\text{kin},0} = \hbar\omega_{\text{XUV}} - I_{p,k}$ with an isotropic initial velocity distribution. The starting point of all electrons is sampled by the density of the electronic ground state wave function. For neon, the atomic 2p ground state density is used, while for C_{60} the ground state is calculated by the jellium model in LDA.

The spherically symmetric density function is approximated by a Gaussian distribution centered at the radius of the carbon atoms (Fig. 5.7a). The radial potential (red) is formed by 60 C^{4+} atoms positioned at the radius $R = 3.52 \text{ \AA}$. This description treats all 120 electrons in the 1s state as localized and considers the remaining $60 \times 4 = 240$ valence electrons as a negatively charged electron cloud. For each carbon atom, three valence electrons form a σ ($n = 1$) bond between each other by sp^2 hybridization. The remaining electrons form a π ($n = 2$) bond directed out of the shell surface. The radius of this shell is close to the carbon cage radius and behaves similar to a metallic hollow sphere (detailed

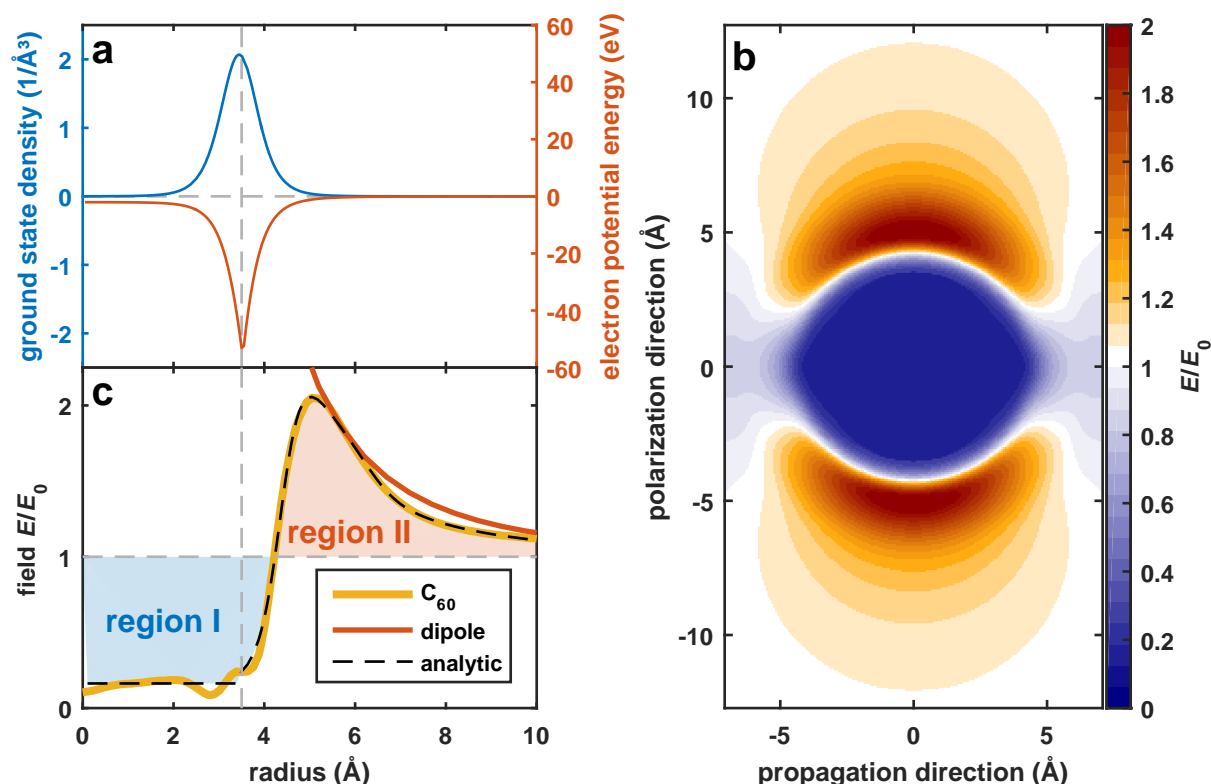


Figure 5.7: Electric field distribution around C_{60} molecule. a) The radial electric potential is formed by the carbon atoms (red). The ground state density function of the electrons is centered around the carbon shell radius $R = 3.54 \text{\AA}$ (grey dashed line). b) The electric field around a C_{60} molecule in units of the incoming field is linear for wavelengths in the visible range. c) The radial field is shown for a cut along the polarization axis (yellow) and approximated by an analytical function (dashed in black). For reference the dipole limit is plotted in red. The shaded areas I and II indicate the influence of the plasmonic near-field with a screened and enhanced laser field, respectively.

explanation in Chapter 2.5.2).

Propagation step

Following the ionization step, all electrons are propagated in the electric fields using the Cash-Karp method for integrating the differential equations of motion [235]. This numerical procedure is a special fourth order Runge-Kutta-Method [236, 237], that contains an estimate for the error and enables the use of an adaptive step size algorithm. Thus, the first steps that involve strong field strengths are calculated with smaller time steps compared to later times with almost free particle propagation. During propagation, three classes of electric fields contribute to the dynamics affecting the measured streaking delay.

First, a constant Coulomb field is present after ionization, which is screened inside the C₆₀ cage. Within this formalism, it is assumed that the electron hole delocalizes instantly after ionization. The resulting Coulomb field is responsible for a significant fraction of the final delay by CLC. Due to the general relevance of the CLC, the observed effect has to be considered in the CTMC simulations of both neon and C₆₀.

Second, the 10¹² W/cm² IR streaking field is responsible for the momentum shift of the final electron distribution. Due to the large IR focus, this driving field is described by a plane wave with a Fourier-limited temporal evolution (Eq. 2.1). Even though the laser field in free space does not induce delays, the interactions of the field with electronic states and induced potentials in the system have to be considered and give rise to additional delays.

Third, in vicinity of the C₆₀ molecule, the plane wave of the streaking field gets distorted and induces an enhanced near-field. In first approximation, the C₆₀ electrons are treated as for a hollow metallic sphere with a finite thickness. Similar to the model in Chapter 2.5 that was used to describe the plasmonic behaviour at XUV frequencies, the electrons are driven by the IR fields. In this frequency range, all valence electrons are weakly bound and follow the driving forces instantaneously. As a result, the imaginary part of the dielectric function vanishes and thus the inside of the molecular cage is almost perfectly screened. On the outside of the carbon cage, the fields are more complicated. In the far field, the field distribution converges to the field of an induced dipole, since the C₆₀ size is small compared to the wavelength [230]. Around the carbon atom shell radius, the field follows a smooth transition between the screened part on the inside and the decaying dipole distribution on the outside (Fig. 5.7b). At a radius of 4.2 Å the near-field strength equals the field of the incoming laser E_0 (Fig. 5.7c). For a fast numerical calculation, the exact field is described by an analytical function:

$$\vec{E}(\vec{r}) = \begin{cases} c_0 \vec{E}_0, & r < R \\ c_0 \vec{E}_0 + \left[\sum_{i=1}^2 \frac{a_i}{\exp\left(\frac{r-b_i}{c_i}\right) + 1} \right] \left(\vec{E}_0 + \frac{\alpha}{4\pi\epsilon_0} \frac{3(\vec{E}_0 \times \vec{r})\vec{r}/r^2 - \vec{E}_0}{r^3} \right), & r \geq R. \end{cases} \quad (5.2)$$

The inner field is reduced to a factor of $c_0 = 0.16$ and the far field is dominated by the dipole with a polarizability of $\alpha \approx 8.9 \times 10^{-39}$ C m²/V (80 Å³ in atomic units). In between the two regions, a sum of two Fermi functions ensures a smooth transition (Tab. 5.1). The maximum field enhancement of ~ 2.1 occurs on the polarization axis about 1.5 Å outside the C₆₀ shell.

5.4.3 Implementation of intrinsic ionization delay

In the previous chapter, the Monte Carlo simulations assumed an instantaneous ionization by the XUV pulse. However, as explained in Chapter 2.4, intrinsic EWS delays occur

i	1	2
a_i	1.01	-0.17
b_i	4.43 Å	6.38 Å
c_i	-0.24 Å	-0.31 Å

Table 5.1: Parameters of Fermi fit. The parameters are retrieved by fitting a sum of two Fermi functions according to Equation 5.2 to the electric field of a C₆₀ molecule. The best fit is visualized in Fig. 5.7c.

depending on the initial state and the photon energy of the investigated system. Since the neon bound states are well separated in energy, it is sufficient to consider the 2p state in the current simulations. The corresponding ionization potential is 21.6 eV with a relatively flat cross section (blue line in Fig. 5.8a), which is described in more detail in Section A.3.1 [238].

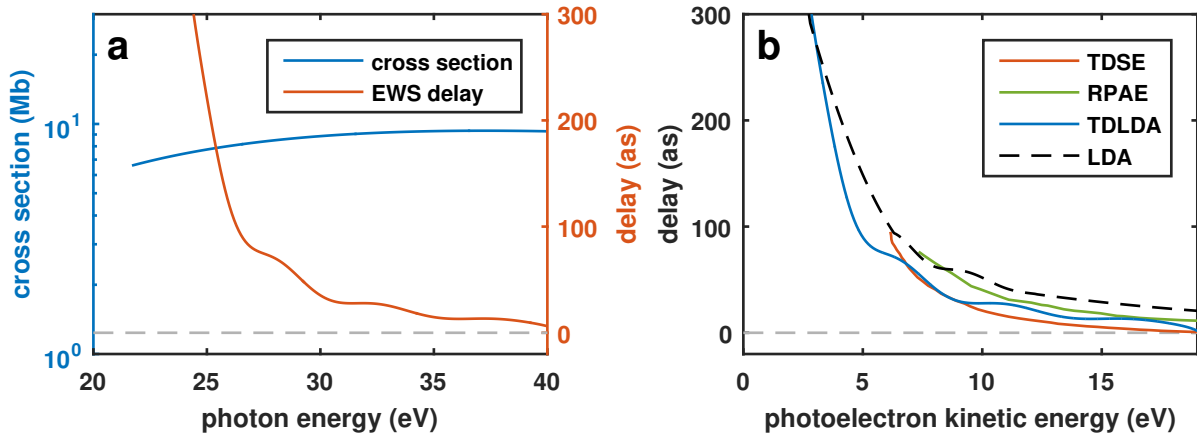


Figure 5.8: Ionization properties of neon. a) The cross section of neon is shown in dependence of the photon energy (blue) above the ionization potential $I_p = 21.6$ eV (plotted after Ref. [238]). The EWS delay is calculated theoretically by a TDLDA approach (red). Both lines correspond to the ionization from the 2p state. b) The overall EWS delay is shown as a function of the photoelectron kinetic energy (blue). For comparison the LDA result (black dashed line) is shown besides a TDSE single-active electron [239] and a random-phase approximation with exchange (RPAE) [145] calculation.

The EWS delay (red line in Fig. 5.8a) vanishes for high energies and increases as the photon energy approaches the ionization potential. Both the smooth behaviour of this curve and the single ionized state contributing in our energy range confirm that neon is a well suited reference target in the presented experiments. Since the delays in neon are well known experimentally and theoretically [240], the measured delays in C₆₀ can be determined with great accuracy.

Fig. 5.8b shows the expected streaking delay for neon on the photoelectron kinetic energy axis. This line is shifted from the photon energy axis by the ionization potential and shows the additional streaking delay in the case of a flat XUV spectrum. Compared to the TDLDA simulations, LDA calculations give very similar results with an increased delay by up to ~ 20 as. The experimentally accessible energy range lies above 8 eV for the present streaking experiments, where both delays stay below an absolute value of 60 as.

The same description employed for neon simulations is used in the C₆₀ CTMC. Eleven states in total are considered in the ionization process. The five lowest lying σ states (1s to 1g) with ionization energies between 31.6 eV and 37.9 eV are neglected due to the cutoff of the XUV spectrum. The five occupied σ states above (1h to 1l) have ionization energies ranging from 11.2 eV to 28.5 eV while the six occupied π states (2s to 2h) have ionization energies between 7.6 eV and 17.4 eV. Fig. 5.9a shows the cross section of three states as an example.

The cross section of the HOMO (blue) and the orbital below (HOMO-1, red) show a pronounced peak around 16.5 eV that is apparent in all π states. This peak is caused by a collective plasmonic oscillation that is degenerate for all π electrons [125]. An additional peak in the cross section appears at ~ 39 eV indicating a faster mode of an oscillatory excitation. The HOMO-2 as the weakest bound σ state barely contributes to the 16.5 eV plasmonic peak (green). All other σ states are bound too strongly in order to play a role in this peak. However, all of the σ states exhibit a strong peak around 38 eV and amount to a total cross section that comparable to the π cross section in this energy range.

The total theoretical cross section (red line in Fig. 5.9b) is compared to experimental data of photoionization cross sections [241, 242]. As reported before [124, 125, 138] and explained in Chapter 2.5, the calculated cross section is red-shifted by 4.3 eV compared to experimental data. In the region above 25 eV the TDLDA calculations underestimate the total cross section, which suggests that the atomic potential is well suited for covering the plasmonic region but might not perfectly represent the high energy atomic behaviour.

The single state EWS delays in Fig. 5.9c correspond to the cross section in Fig. 5.9a. It is obvious that the states with the same n follow a similar trend in the EWS delay (π states in blue and red), while the σ state shows a different behaviour. Large delays towards low photon energies indicate the resonant excitation, although this behaviour is suppressed in the emitted electron spectrum due to the low partial cross section for these energies.

For a first estimate of the final streaking delay, the single state delays $\tau_k(E)$ are summed up weighted by their transition matrix element $\sqrt{\sigma_k(E)}$ to get an averaged EWS delay

$$\bar{\tau}(E) = \frac{\sum_k \sqrt{\sigma_k(E)} \tau_k(E)}{\sum_k \sqrt{\sigma_k(E)}}. \quad (5.3)$$

The averaged delay is shown for TDLDA and LDA calculations in Fig. 5.9d.

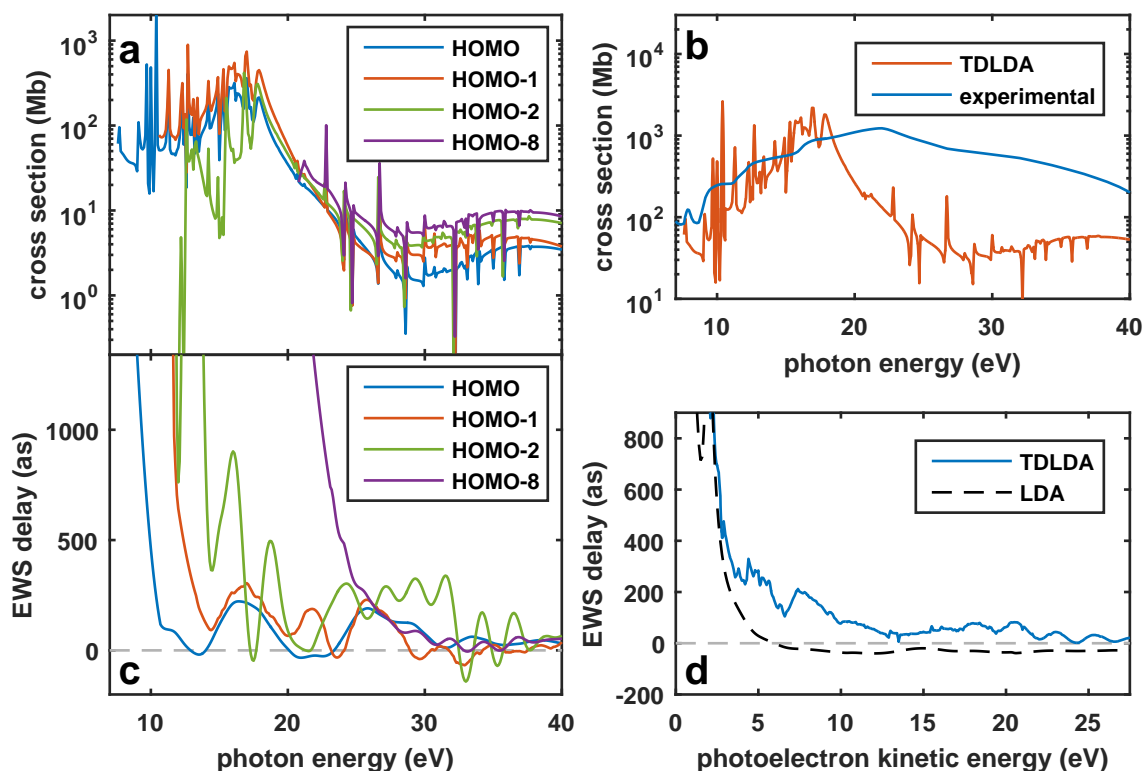


Figure 5.9: C_{60} properties. a) The cross section is shown for the three highest lying states and the 1j-state with ionization potentials of 7.6 eV, 10.6 eV, 11.1 eV and 20.8 eV. In total 11 states are considered in the TDLDA calculations. b) The total calculated cross section (red) is compared to experimental values (blue) [241, 242]. c) The EWS delay for the same states is shown as a function of the photon energy. d) The total delay averaged over all states is shown for LDA and TDLDA calculations. A detailed description of the averaging procedure is given in the text.

5.4.4 Simulation results of neon

The simulations of neon streaking delays are used to retrieve the unknown second order dispersion of the XUV pulse. Simulations are performed for a GDD between 0 as^2 and $24\,000 \text{ as}^2$ and compared to the experimental results (black dashed line in Fig. 5.10). Each of the simulated streaking delay curves (colored lines) is shifted vertically for an optimal agreement with the experiment in the energy range from 11 eV to 19 eV. The vertical shift is used as a free parameter since the absolute time zero is unknown in the experiment. Strictly speaking, the experiment would have to be shifted towards the simulations, but the reversed approach is applied for a better visualization in the Figure and does not change the result.

Each GDD value results in an average deviation of the streaking delay that is plotted

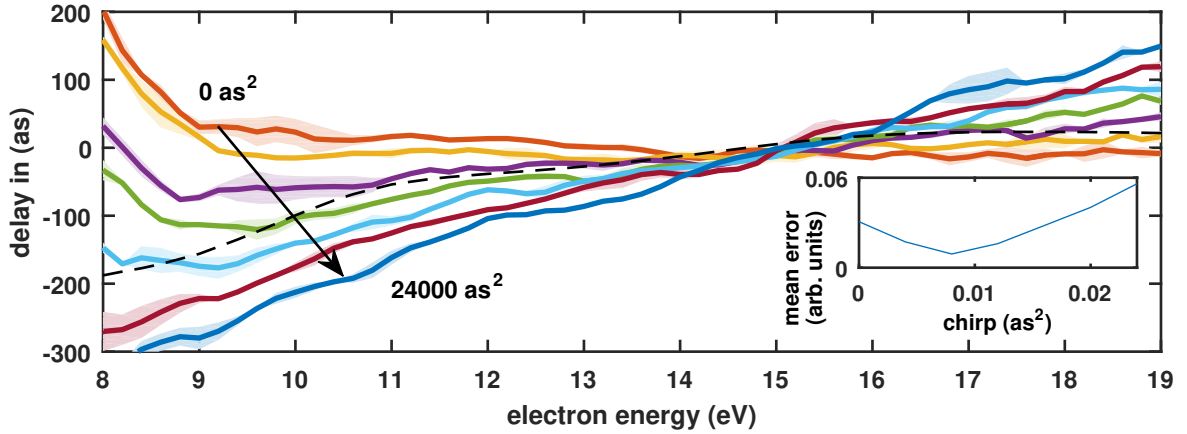


Figure 5.10: Effect of XUV chirp. The measured neon streaking delay (Fig. 5.4) is shown as a dashed line. Neon streaking simulations are performed with a range of XUV second order dispersion values and the simulated delay is compared to the experimental plot. The best agreement in the range of 11 eV to 19 eV is achieved for a chirp of 8000 as^2 (see inset).

in the small inset. For a GDD of about $\varphi_2 = 8000 \text{ as}^2$, the deviation is minimal. This value is in good agreement with previous measurements [22, 68] and is used for the C_{60} simulations as well¹.

5.4.5 Results C_{60}

The retrieved GDD of the XUV pulse and the EWS delay for each state fully characterize the conditions of the C_{60} photoionization process. Subsequently, CTMC simulations of C_{60} streaking are performed. The XUV-IR delay in typical C_{60} calculations is scanned in steps of 50 as from -4 fs to $+4 \text{ fs}$ to cover at least three full optical cycles, while each delay step contains 500 000 particle trajectories. The simulation uses the measured XUV spectrum and propagates the electron with an adaptive step size Runge-Kutta algorithm.

The final photoelectron kinetic spectrum possesses a higher cutoff energy compared to neon due to the ionization potential of 7.6 eV for C_{60} (Fig. 5.11a). The retrieval of contour lines, the fitting procedure with Gaussian sine functions and the extraction of the streaking delay is done in the same manner as for the neon simulations (Fig. 5.11b). To summarize, the C_{60} delay curves contain contributions from CLC, the plasmonic near-fields, the EWS delay, the XUV spectrum and the projection in the VMI spectrometer. The following analysis and discussion aim to clarify the influence of the plasmon on the photoionization process.

¹In the framework of this work, the GDD is described by the variable φ_2 instead of β , which has an opposite sign (Eq. 2.4, compare for example Ref. [41] and Ref. [42]). In both cases the XUV pulse is *positively chirped*.

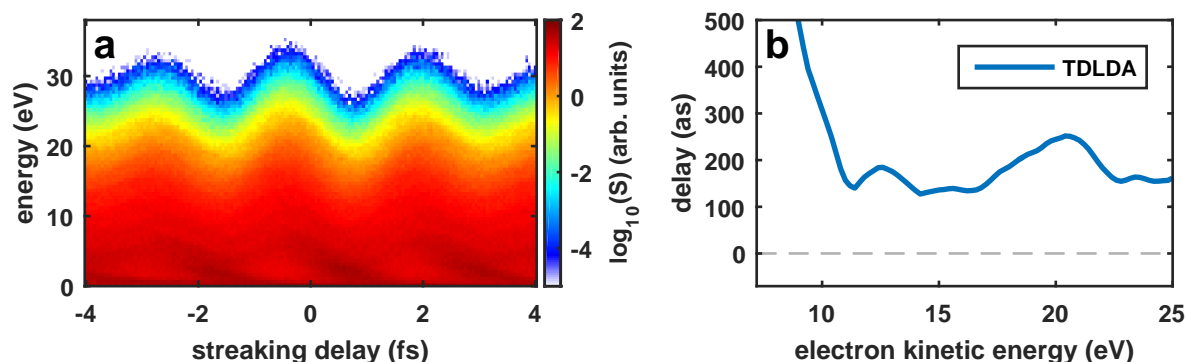


Figure 5.11: Simulated C_{60} streaking. a) This spectrogram shows the simulation of C_{60} streaking with the XUV spectrum of Fig. 5.2 and an 700 nm, 5 fs IR pulse with an intensity of 10^{12} W/cm² and a chirp of 8 000 as². The initial position is sampled with the ground state density and the initial velocity vector is isotropic. TDLDA calculations are used to determine the intrinsic EWS delay. The final electron spectrum is evaluated 15 fs after the laser peak for a full opening angle of 50° along the polarization axis on the VMI detector. b) The energy-dependent streaking delay is retrieved by fitting Gaussian sine waves to contour lines.

5.5 Discussion

5.5.1 Plasmonic near-field

The streaking of C_{60} reveals a characteristic plasmonic near-field effect, which is caused by the formation of an induced dipolar field for frequencies in the visible range (Fig. 5.7). This near-field corresponds to a distortion of the streaking IR laser field compared to atomic or molecular streaking, where the IR field is assumed to be a plane wave. To illustrate the influence of the plasmonic near-field on the final streaking delay in Fig. 5.12, the plasmonic contribution of the XUV pulse to the EWS delay is neglected at this point.

The black line in Fig. 5.12 corresponds to the atomic case without the consideration of the plasmonic near-field at all. The IR field is treated as a plane wave and the final delay is mainly governed by the CLC and the XUV chirp responsible for the increasing delay with energy. The absolute position of the zero delay is arbitrary and manually chosen for this comparison.

In order to understand the influence of the IR-induced near-field, certain contributions of the near-field are included separately. Region I (Fig. 5.7c) refers to the inner part of the C_{60} cage up to the radius where the field strength equals the incoming field E_0 . Since the field at the inside is reduced to about 16% of E_0 , the ionized electrons are barely affected by the streaking field until they leave the carbon cage. In the final spectrum they behave as if they have been ionized at the time they escaped the screened volume of

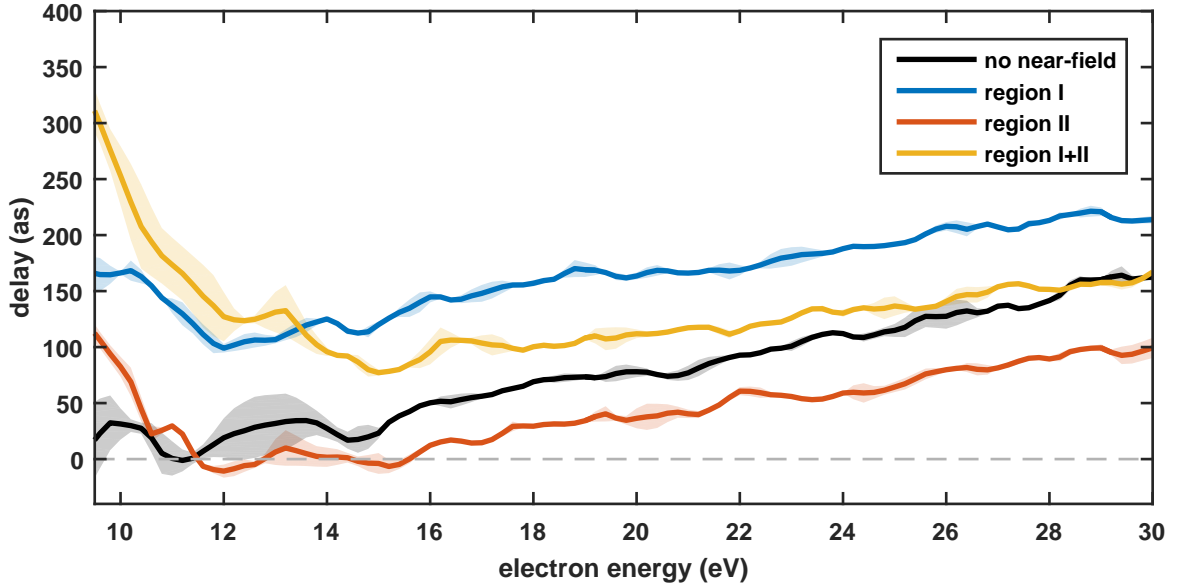


Figure 5.12: Streaking delay for different field conditions. All lines correspond to the simulated streaking delay in C_{60} for a chirp of $8\,000\text{ as}^2$ and no EWS delay. No near-field means that the IR laser field is undisturbed as in atomic or molecular streaking (black line). Region I (blue) and region II (red) refer to radial intervals indicated in Fig. 5.7c. The details about the incorporated fields are explained in the text.

the C_{60} molecule. This escape time is delayed with respect to the real birth time by the propagation time taken by the electron to travel from its ionization site to the escape point (blue line). This observation is in line with previous experiments on streaking with SiO_2 nanoparticles [22, 234] or from metallic surfaces [11, 243].

On the contrary, the increased plasmonic field in region II amplifies the influence of the streaking field on the electrons. The near-field with a field strength of up to $2 E_0$ accelerates the emission process and leads to a negative delay compared to the atomic case (red line). This effect may be understood as the opposite to a screened field as in region I.

The combination of regions I+II is equivalent to the full C_{60} simulations. As expected, it is a mixture of the two individual regions and results in an average delay (yellow line). However, the influence of the screened part inside the cage is obviously stronger than the counteracting enhanced part outside. The effective delay of the plasmonic near-field remains positive compared to plane wave reference.

5.5.2 Comparison between experiment and simulation

In order to gain insight into the interaction of C_{60} -molecules with light, the theoretical calculations is compared to experimental streaking delay data. In this comparison the neon

reference is subtracted from the C_{60} delays for both the experimental and the theoretical analysis. The experimental data shown in Fig. 5.4 is averaged over four different measurements with two streaking traces in polarization direction each (blue dots in Fig. 5.13) and the error bars indicate the standard deviation of the retrieved delays.

The theoretical delay curves in black and yellow correspond to the curves in Fig. 5.12, but with a neon reference in this case. The effect of the positive delay due to the plasmonic near-field is clearly visible especially at lower energies.

The experimental data shows a zero crossing in the measured streaking delays at around 13.4 eV, where the influence of the plasmonic resonance on the EWS delay is approximately expected to emerge, even though the broad resonance affects large portions of the energy-dependent delay. In the resulting theoretical delay curves (red line), that include the plasmonic near-field and the EWS delay, two major changes are observed. Firstly, at low energies the experimental trend towards large delays is reproduced, which is attributed to the short-range Coulomb fields causing a large EWS delay. Secondly, in the electron energy range between 17 eV and 21 eV minor discrepancies are present, which corresponds to the region where the theoretical and experimental cross sections start to differ (see Fig. 5.9). In the photon energy range above the 20 eV-plasmon, the TDLDA calculations seem to underestimate the cross section by at least one order of magnitude.

A possible reason for this behaviour is found in the theoretical modelling of the C_{60} potentials. On large length scales, the spherical model fits the actual C_{60} profile very well. The jellium model utilizes a uniform ionic background and the valence electrons for a suitable description of the molecule's shape. In analogy to a particle in a box, the features over large distances correspond to the electronic states at low energies. Accordingly, our model resembles the low lying π and σ states, reproduces the IR response of the system and gives a good description of the collective electron plasmon at around 20 eV. However, on the short length scales below one ångström the atomic nature of the C_{60} potentials is not considered well enough. The tightly bound inner electrons are not included in the TDLDA calculations but are absorbed in the shell consisting of 60 C^{4+} ions. Consequently, both the calculated cross sections and the EWS delays at higher energies may be missing the atomic contribution from the single carbon atoms.

Around the cutoff energies, the EWS contribution vanishes, since this energy range is well above the position of the significant plasmon resonances (Fig. 5.9d). In addition, the CLC term converges to zero and has no considerable contribution to the streaking delay. In a first order approximation the high energy streaking delay converges to a negative delay of

$$\varphi_2 \cdot \frac{\overline{I_{p,C_{60}}} - I_{p,Ne}}{\hbar} = 8000 \text{ as}^2 \cdot \frac{16.0 \text{ eV} - 21.6 \text{ eV}}{\hbar} = -68 \text{ as}. \quad (5.4)$$

Here, $\overline{I_{p,C_{60}}}$ denotes the spectrally average ionization potential of C_{60} which is significantly higher than $I_p = 7.6 \text{ eV}$. In this regime the resulting streaking delay is determined by the positive chirp of the XUV pulse and the differences between the ionization potentials [244]. A detailed explanation of this effect is given in Chapter A.3.3. Although this behaviour is

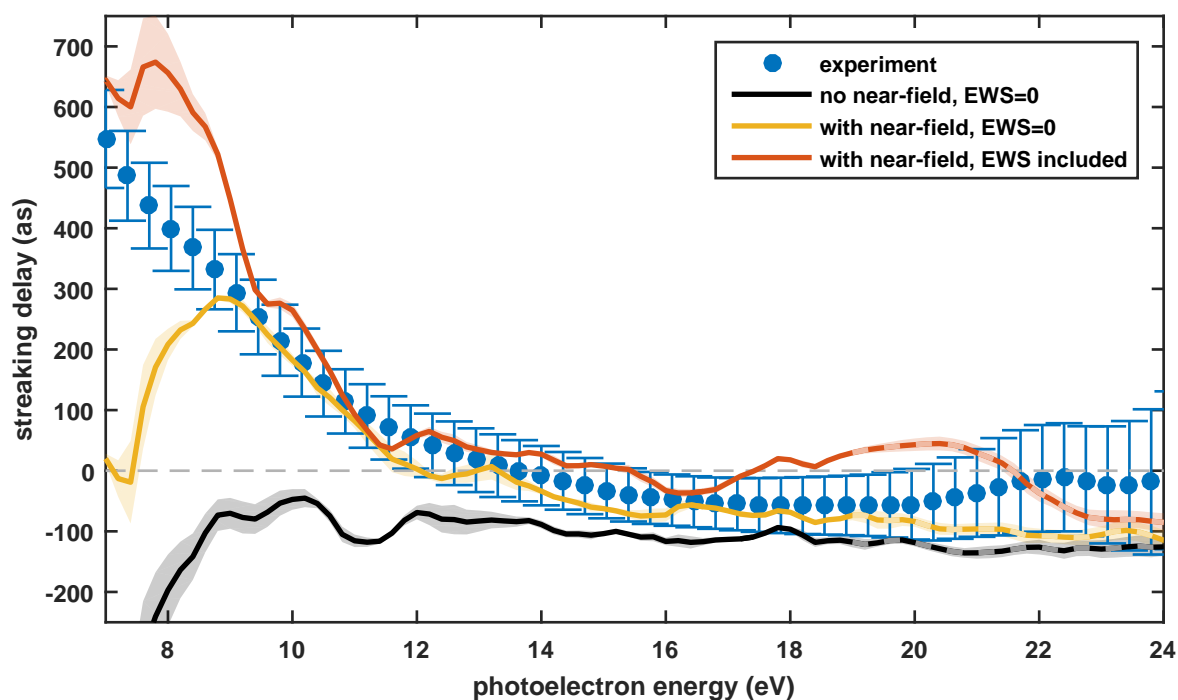


Figure 5.13: C_{60} streaking delay with neon reference. The experimental delay is obtained by subtracting the neon reference from the target C_{60} (blue). The standard deviation of four sets of measurements determines the error bars. The XUV spectrum ranges from 20–35 eV and the few-cycle streaking field is centered around 720 nm. The theoretical results are obtained with the same conditions and utilize TDLDA for the EWS calculations (red). The curves without EWS contribution (black and yellow) refer to the corresponding lines in Fig. 5.12. The dashed parts of the lines indicate regions where the neon data is extrapolated (explanation in Chapter A.3.2).

difficult to observe in the experimental data due to a limited signal level, it indicates the expected trends close to the cutoff energies.

To summarize, the theoretical model considers the following features and effects:

- experimental IR streaking laser field conditions, including wavelength and intensity (Chapter 5.4.2: Propagation step)
- experimental XUV attosecond pulse properties, including spectrum and chirp (Chapters 5.4.2: Ionization step and 5.4.4)
- the ground state configuration of C_{60} , calculated by a jellium model in LDA (Chapter 2.5.2)

- time-dependent response to external excitations for neon and C_{60} , calculated in TDLDA (Figs. 5.8 and 5.9)
- the interaction of the Coulomb field with the streaking laser field (CLC) and the plasmonic near-field distribution (Fig. 5.7)
- analysis according to the experimental detection methods, including VMI, spectrogram generation, determination of contour lines and fitting procedure (Chapter 5.3).

5.6 Conclusion

The experimental determination of the photoionization delay in C_{60} is the first successful time-domain measurement of plasmons. The extensively characterized neon gas as reference for the streaking guarantees a precise control over the delay and ensures absolute timing information. The extracted delay is confirmed in several sets of repeated measurements.

Subsequently, all results are compared to numerical TDLDA calculations, which are able to reproduce the electronic ground states as well as the dynamic response of the molecular system to external electric fields. The simulations help to disentangle different contributions to the final streaking delay. The plasmonic near-field modifies the streaking IR laser field and causes an additional photoionization delay for all kinetic energies. Firstly, the inner part of the molecule is screened by the electron cloud, which results in a positive delay of the emitted electrons. Secondly, the outer volume close to the C_{60} poles provides an enhanced field that leads to an accelerated emission process. This plasmonic contribution is essential to capture the full photoionization dynamics in C_{60} . Furthermore, the XUV electric fields resonantly excite modes of collective electron plasmons which strongly affect the photoabsorption cross sections. Such giant resonances appear in many fields and always offer a path to access the inner structure of objects like atomic nuclei, single atoms or large molecules as C_{60} [245]. Besides the appearance in absorption spectra, these excitations influence the EWS delay, accessible by attosecond streaking.

The presented experiments and simulations form the basis for manifold future research. Possible measurement with higher XUV energies may explore additional regions of the C_{60} absorption spectrum with potential probing of the higher energy plasmon. If technically available, endohedral fullerenes may offer advantageous conditions for probing influences of a closed shell environment on emission delays [149, 246, 247]. With a single atom in the very center of the C_{60} molecule a very narrow absorption line can be addressed which simplifies the streaking spectrogram. Moreover, the localized central atom gives a well-defined starting position of the streaked electron, which supports the trajectory analysis.

Another extension of the presented streaking method includes the investigation of other systems with plasmonic behaviour. Nanosystems are capable of enhancing the in-

coming electric fields similar to C_{60} molecules [170, 172, 248–250].

6 Conclusion and Outlook

In the framework of this thesis, three different experiments on light-matter interaction are presented, which are promising examples for future imaging applications, controlling biomolecular or chemical reactions [157, 251–255] and manipulations in semiconductor electronics [256, 257]. All presented experiments are based on ultrafast dynamics on the femtosecond or attosecond time scale. In order to resolve such ultrafast processes, few-cycle laser pulses are utilized in order to extend the established knowledge to new frontiers and to achieve progress in fundamental research of light-matter interactions.

Firstly, nanoTRIMS is introduced as a novel method to investigate molecular reactions. The presented setup provides deep insight into the interaction of few-cycle laser pulses with spherical nanoparticles. In short, the laser-induced enhanced near-fields create inhomogeneous surface charges on the nanoparticle, whose distribution depends on the ratio between the particle diameter and the wavelength. Simultaneously, protons are generated from molecular residues on the surface, propagate in the near-fields and are detected in the spectrometer. To gain a thorough understanding of the charge interactions during the photoionization and deprotonation process, additional Monte-Carlo simulations are performed. The convincing agreement between theory and experiment confirms that the numerical model is suitable to track the proton dynamics. A simple electrostatic model generalizes the findings of the nanoparticle experiment and establishes a clear relation between the spatial surface charge distribution and the measured proton momentum distribution. The latter model lays the foundation for imaging charges of more complex shapes and environments. Ultimately, this scheme may be used to probe time-dependent chemical surface reactions.

Secondly, the dynamics of a spherical nanoscopic plasma is observed which is generated by strong-field laser pulses. A delayed x-ray free-electron laser pulse probes the radial expansion of the plasma density on a femtosecond scale. The measured diffraction patterns reveal that the outer diameter of the plasma sphere is increasing driven by the repelling charges. Simultaneously, this expanding layer of ions and electrons leaves a core of almost undisturbed plasma density behind shrinking over time. This counter-intuitive twofold dynamics was predicted by specialized MicPIC simulations designed for the modelling of nanoscale plasma dynamics. The presented experiment already serves as an excellent benchmark for the corresponding theoretical model and helps to transfer the gained knowledge to other plasma expansion experiments. Future studies on this topic could aim towards novel materials forming a plasma upon the interaction with strong-field

laser pulses. Especially metallic particles offer unique properties due to their screening effect and possible resonant excitations.

Thirdly, the photoionization delay from C_{60} molecules is investigated by attosecond streaking spectroscopy. Briefly, an XUV pulse ionizes the molecule and releases an electron that gets probed by a delayed IR few-cycle laser pulse. The timing of the emitted electron is affected by resonant plasmonic excitations and linear near-fields induced by the streaking electric field. For an absolute timing delay in the streaking measurements, a neon measurement, which is recorded in addition to the C_{60} target, ensures the timing with respect to a reliable reference. As a result, an absolute timing delay is extracted from the streaking measurements. Finally, the experimental data is successfully modelled by a TDLDA and CTMC approach. The theoretical calculations are able to disentangle the influence of the plasmonic excitation from the effect due to local near-fields and the delays related to Coulomb-laser coupling and XUV chirp.

The three presented topics share the commonality to be located in a challenging regime of sub-wavelength scales and ultrafast dynamics on the femtosecond scale and below. Furthermore, the high number of involved particles and their interactions with each other and electric fields demand for innovative theoretical models. On the one hand, those models have to consider quantum mechanical aspects. On the other hand, they have to efficiently handle the macroscopic effects caused by the high number of interacting particles. In this thesis, this conflict is solved by suitable approximations resulting in good agreement with the experimental results. The theoretical description of the experiments helps to observe and – most importantly – to control motions on attosecond times, which may support the extension towards faster dynamics and more complex nanosized systems.

A

Appendix

A.1 nanoTRIMS

A.1.1 Resolution of spectrometer

The theoretical resolution of the spectrometer in Fig. 3.2 is estimated from trajectory calculations. The initial momentum is varied along each dimension and the change in time-of-flight is used to retrieve the initial momentum by applying analytical formulas¹. The difference between the input momentum and the calculated momentum is taken as a measure for the linearity of the spectrometer and its practicability for recording ion spectra (Fig. A.1a). If needed, the remaining error can be reduced by refining the analytical formula by the use of effective voltages and distances, since the error function is almost perfectly linear. One can detect a small non-linearity in z -direction around $p_z = 0$ which is probably due to the distortion of the grounded nanoparticle source close to the electrodes. However, the deviation is on the order of 10^{-3} a.u., which is well below the experimental resolution.

The size of the focal volume induces a distribution of starting points that gets convoluted with the momentum distribution on the detector. Fig. A.1b illustrates how broad the retrieved distribution appears for certain momentum values caused by the finite focal volume. In fact, the uncertainty in the determined momentum does not depend on the absolute initial momentum but is a function of the initial focus size. Along laser propagation, a FWHM of $200\ \mu\text{m}$ is assumed, perpendicular to the propagation axis the FWHM is $40\ \mu\text{m}$. The resulting FWHM of the retrieved momentum distribution is about 0.5 a.u. and 0.1 a.u., respectively. For clarity, the linear dependence on focus size is shown in Fig. A.1c. All values are calculated for the voltages and dimensions in Fig. 3.2. Lower voltages could for example improve the resolution on the cost of the measurement range and a clear separation between the species.

A.1.2 Focal averaging

Focal averaging has to be considered under experimental conditions where not only the highest intensity in the center of the focus is relevant but also regions with lower intensities.

¹In this case a constant acceleration is assumed in two separate regions.

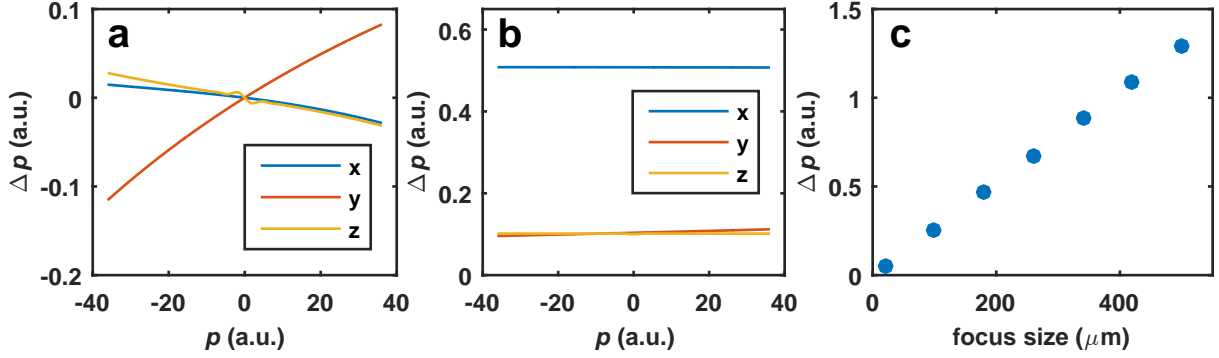


Figure A.1: Spectrometer resolution. a) H^+ ions are started in the center of the spectrometer with a distribution of initial momenta in each dimension. The lines show the deviation of the momentum calculated by an analytical formula from the real momentum. b) H^+ ions are started in the center of the spectrometer with a spatial distribution corresponding to a laser focus. For each value of initial momentum the uncertainty is given by the momentum spread due to a finite interaction region. c) The expected uncertainty is shown for a few selected focus sizes and does not depend on the axis of interest.

In this thesis, a Gaussian intensity distribution in the focal plane is assumed and a constant intensity along the propagation direction due to the limited target size along the latter axis. A spatial integral in the focal plane reveals that the integral over the intensity has to be weighted with the inverse of the intensity.

$$\begin{aligned}
 I(r) &= I_0 \exp\left(-\frac{r^2}{\sigma^2}\right) \\
 \frac{dI}{dr} &= I_0 \exp\left(-\frac{r^2}{\sigma^2}\right) \left(-\frac{2r}{\sigma^2}\right) = I(r) \left(-\frac{2r}{\sigma^2}\right) \\
 V &= \int \int r \, d\varphi \, dr = 2\pi \int \frac{dI}{I(r) \left(-\frac{2}{\sigma^2}\right)} = -\pi\sigma^2 \int dI \frac{1}{I(r)}
 \end{aligned} \tag{A.1}$$

A.1.3 Nanoparticle preparation

The SiO_2 nanoparticles are prepared as described in Chapter 3.2.3 in the group of Dr. Markus Gallei at TU Darmstadt. The transmission electron microscopy (TEM) images (Fig. A.2) show the shape and size distribution of the particles. These images verify the results from dynamic light scattering measurements and confirm the low polydispersity of the samples.

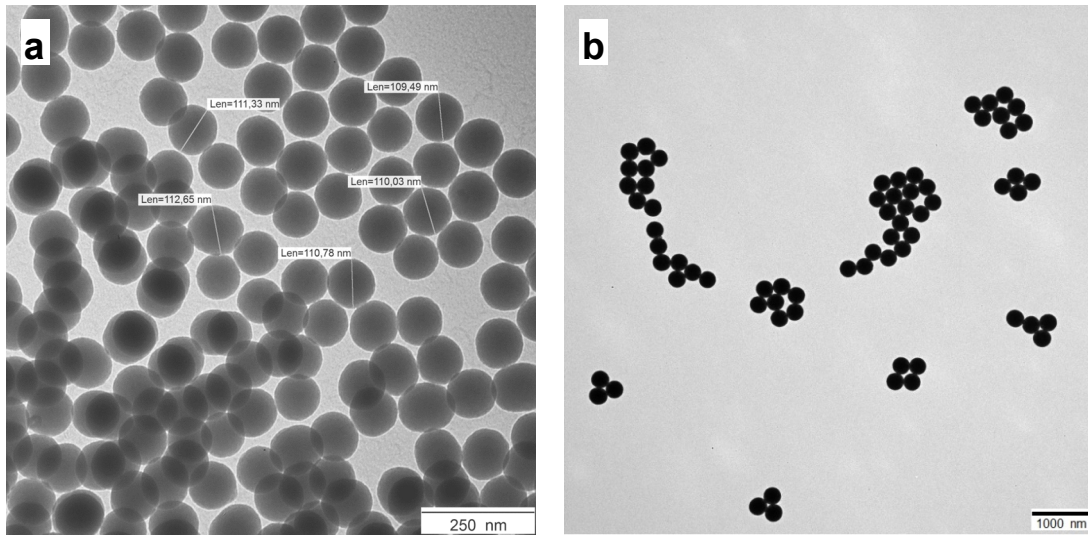


Figure A.2: TEM images of silica nanoparticles. The images of spherical a) 110 nm and b) 300 nm SiO_2 nanoparticles were recorded in the group of Dr. Markus Gallei at TU Darmstadt.

A.1.4 Iterative optimization algorithm

The working principle of the iterative optimization algorithm is presented in Chapter 3.5.3. Here, the fitting procedure for a simple surface charge distribution is elucidated in more detail.

The starting point is a charge distribution that is centered in two quadrants of the 300 nm sphere (Fig. A.3a). To check the feasibility of the presented algorithm, a first test is done with a charge distribution that is expanded into spherical harmonics with $L = 2$. The initial H^+ distribution is proportional to $|E(\theta, \varphi)|^k$ with $k = 10$ in this case. In the electrostatic field the H^+ propagation is calculated and the final momentum distribution is projected onto the polarization and propagation plane, which acts as a symmetry plane in this model (Fig. A.3b). The optimization algorithm varies the coefficients of the spherical harmonics and the exponent k describing the nonlinear dissociation process. For the simple test case with a low-order charge distribution, the agreement between the reference and the fitted projected momenta is almost perfect (Fig. A.3c) and accordingly, the retrieved surface charges match the originally assumed distribution (compare subfigures a and d in Fig. A.3).

A comparison between the retrieved fitted coefficients and the reference numbers shows only small deviations that do not influence the overall distribution (Table A.1).

This exemplary $L = 2$ case shows that the inversion algorithm is able to retrieve the surface charge distributions in simple cases. An advanced example proves that even more complicated distributions (Fig. 3.9) can be resolved to a satisfactory extent. The method is suitable to reveal the surface conditions in nanoparticles and invert the measured

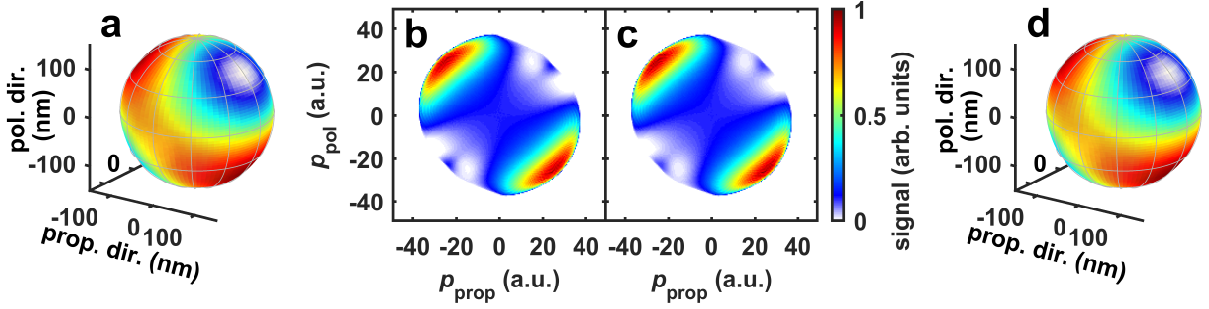


Figure A.3: Inversion method. a) An arbitrary initial surface charge distribution is described with spherical harmonics up to order $L = 2$. The charge density on a 300 nm particle is encoded in the color scale. b) According to this charge distribution, the protons are generated on the surface and propagated in the static fields. The expected final H^+ momenta is projected onto the polarization and propagation plane. c) The final H^+ momenta for the best fit are shown in projection. d) The retrieved initial charge distribution is shown on the surface of the nanosphere.

momentum distributions in an faster alternative way to full M^3C -simulations.

A.2 Plasma expansion of nanoparticles

A.2.1 Scattering images of nanoparticles

The scattering images of nanoparticles are obtained by illumination with an 800 eV XFEL beam and reveal detailed insight into the structure of the nanoparticles and possible formations of nanoparticle clusters. Fig.A.4 presumably shows a dimer of two nanoparticles

$ m $	0	1	2
Y_0^m	1000/1007	-	-
Y_1^m	0.0/0.27	0.0/-0.18	-
Y_2^m	-13.4/-11.5	105.6/96.6	-22.6/-18.8
k	10.0/10.2		

Table A.1: Fit parameters of inversion method. The upper part shows the coefficients of the spherical harmonics up to the order $L = 2$. Although $m = [-l; l]$ the symmetry plane causes the coefficients for the positive and negative m to be the same. The last line shows the exponent k for the description of the nonlinear behaviour. The blue color describes the reference values, while the orange color represent the fitted values.

that induce stripes in the scattering image in addition to the circular rings. Such cluster images are neglected in the analysis of plasma dynamics.

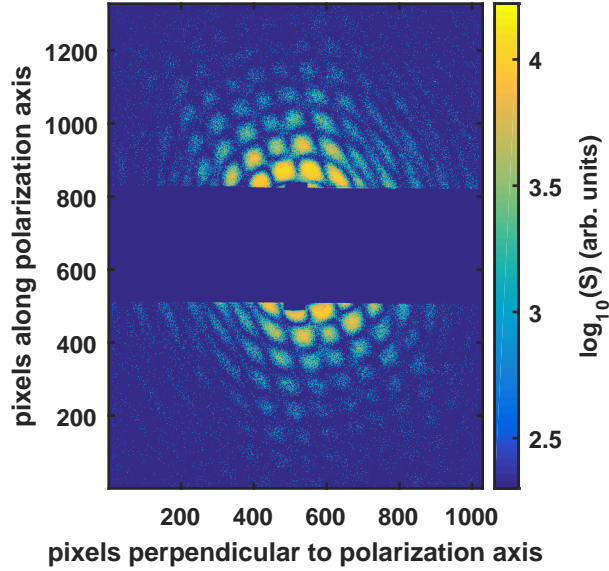


Figure A.4: Scattering image of nanoparticle cluster. The rotational symmetric ring corresponds to the spherical nature of the single particles. The overlying "stripes" from the upper left corner towards the lower right edge refer to a cluster of two nanoparticles.

A.3 Photoemission time delays of C₆₀

A.3.1 Analytical formula for neon cross section

The photoionization cross section σ of neon in dependence of the photon energy E can be approximated by an empirical function [238]:

$$\begin{aligned}
 \sigma(E) &= \sigma_0 F(y), \\
 x &= \frac{E}{E_0} - y_0, \\
 y &= \sqrt{x^2 + y_1^2}, \\
 F(y) &= [(x-1)^2 + y_w^2] y^{0.5P-5.5} \left(1 + \sqrt{\frac{y}{y_a}}\right)^{-P}.
 \end{aligned} \tag{A.2}$$

The fit parameters E_0 , σ_0 , y_a , P , y_w , y_0 and y_1 for neon are given in Tab. A.2. The curve is plotted up to 40 eV in Fig. 5.8a.

Parameter	Value
E_0	4.870 eV
σ_0	4287.0 Mb
y_a	5.798
P	8.355
y_w	0.2434
y_0	0.04236
y_1	5.873

Table A.2: Parameters for neon photoionization cross section. The table lists all 9 parameters in Eq. A.2 to calculate the photoionization cross section in neon. Taken from Ref. [238].

A.3.2 Linear extrapolation in neon

Due to the large ionization potential of neon, the photo electron cutoff is higher than for C_{60} . Since CLC and the EWS delay vanish for higher energies, the neon streaking delay is extrapolated towards this energy range (Fig. A.5). First, a linear fit is applied in the region from 15 eV to 19 eV (red line), which is used as an linear extrapolation for the energies above 19 eV. This analysis method is applied in Fig. 5.13.

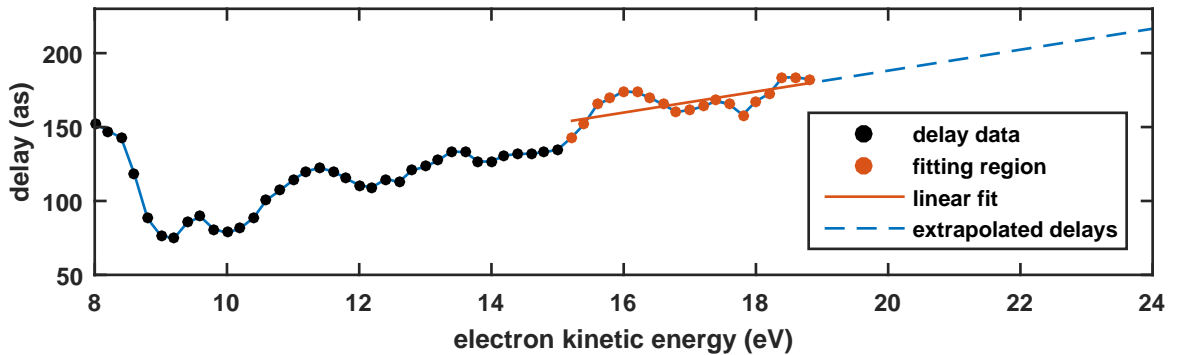


Figure A.5: Linear extrapolation of neon streaking delays. This exemplary neon simulation utilizes the experimental XUV spectrum, the EWS delay calculated by TDLDA and an XUV chirp of 8000 as^2 . The streaking delay is shown as black and red dots and the linear fit as a red line. The resulting delay curve is shown as a blue line, which is dashed in the region of extrapolation.

A.3.3 Effect of linear chirp on streaking delay

The XUV chirp induces a streaking delay in dependence of the photon energy. The expected delay in dependence of the photoelectron kinetic energy depends on the ionization potential

of the investigated target. For neon, the observed shift is the ionization potential of 21 eV. However, C₆₀ contains many states with the corresponding ionization potentials, which have to be considered in the delay analysis. To approximate the effective shift, the ionization potential $I_{p,k}$ of each state is weighted with the overlap between the cross section $\sigma_k(E)$ and the XUV spectrum $S(E)$:

$$\overline{I_{p,C_{60}}} = \frac{\sum_k I_{p,k} \int_0^\infty \sigma_k(E) \cdot S(E) dE}{\sum_k \int_0^\infty \sigma_k(E) \cdot S(E) dE} = 16.0 \text{ eV}. \quad (\text{A.3})$$

In case differential delays between two targets are considered, the different effective ionization potentials result in a residual delay. This behaviour is expressed in Eq. 5.4.

Bibliography

- [1] T. H. Maiman. Stimulated Optical Radiation in Ruby. *Nature*, **187**:493–494, 1960.
- [2] F. J. McClung and R. W. Hellwarth. Giant Optical Pulsations from Ruby. *J. Appl. Phys.*, **33**:828–829, 1962.
- [3] W. E. Lamb. Theory of an Optical Maser. *Phys. Rev.*, **134**:A1429–A1450, 1964.
- [4] L. E. Hargrove, R. L. Fork, and M. A. Pollack. Locking of He-Ne Laser Modes induced by synchronous intracavity Modulation. *Appl. Phys. Lett.*, **5**:4–5, 1964.
- [5] E. P. Ippen, C. V. Shank, and A. Dienes. Passive mode locking of the cw dye laser. *Appl. Phys. Lett.*, **21**:348–350, 1972.
- [6] P. F. Moulton. Spectroscopic and laser characteristics of $\text{Ti:Al}_2\text{O}_3$. *J. Opt. Soc. Am. B*, **3**:125, 1986.
- [7] D. Strickland and G. Mourou. Compression of amplified chirped optical pulses. *Opt. Commun.*, **55**:447–449, 1985.
- [8] T. Brabec and F. Krausz. Intense few-cycle laser fields: Frontiers of nonlinear optics. *Rev. Mod. Phys.*, **72**:545–591, 2000.
- [9] A. Wirth, M. T. Hassan, I. Grguraš, J. Gagnon, A. Moulet, T. T. Luu, S. Pabst, R. Santra, Z. A. Alahmed, A. M. Azzeer, V. S. Yakovlev, V. Pervak, F. Krausz, and E. Goulielmakis. Synthesized light transients. *Science*, **334**:195–200, 2011.
- [10] M. F. Kling, C. Siedschlag, A. J. Verhoef, J. I. Khan, M. Schultze, T. Uphues, Y. Ni, M. Uiberacker, M. Drescher, F. Krausz, and M. J. Vrakking. Control of electron localization in molecular dissociation. *Science*, **312**:246–248, 2006.
- [11] A. L. Cavalieri, N. Müller, T. Uphues, V. S. Yakovlev, A. Baltuška, B. Horvath, B. Schmidt, L. Blümel, R. Holzwarth, S. Hendel, M. Drescher, U. Kleineberg, P. M. Echenique, R. Kienberger, F. Krausz, and U. Heinzmann. Attosecond spectroscopy in condensed matter. *Nature*, **449**:1029–1032, 2007.
- [12] S. Zherebtsov, T. Fennel, J. Plenge, E. Antonsson, I. Znakovskaya, A. Wirth, O. Herrwerth, F. Süßmann, C. Peltz, I. Ahmad, S. A. Trushin, V. Pervak, S. Karsch, M. J. J. Vrakking, B. Langer, C. Graf, M. I. Stockman, F. Krausz, E. Rühl, and M. F. Kling.

- Controlled near-field enhanced electron acceleration from dielectric nanospheres with intense few-cycle laser fields. *Nat. Phys.*, **7**:656–662, 2011.
- [13] F. Calegari, D. Ayuso, A. Trabattoni, L. Belshaw, S. De Camillis, S. Anumula, F. Frassetto, L. Poletto, A. Palacios, P. Decleva, J. B. Greenwood, F. Martín, and M. Nisoli. Ultrafast electron dynamics in phenylalanine initiated by attosecond pulses. *Science*, **346**:336–339, 2014.
- [14] M. Kübel, R. Siemering, C. Burger, N. G. Kling, H. Li, A. S. Alnaser, B. Bergues, S. Zherebtsov, A. M. Azzeer, I. Ben-Itzhak, R. Moshhammer, R. de Vivie-Riedle, and M. F. Kling. Steering Proton Migration in Hydrocarbons Using Intense Few-Cycle Laser Fields. *Phys. Rev. Lett.*, **116**:193001, 2016.
- [15] M. Uiberacker, T. Uphues, M. Schultze, A. J. Verhoef, V. Yakovlev, M. F. Kling, J. Rauschenberger, N. M. Kabachnik, H. Schröder, M. Lezius, K. L. Kompa, H. G. Muller, M. J. Vrakking, S. Hendel, U. Kleineberg, U. Heinzmann, M. Drescher, and F. Krausz. Attosecond real-time observation of electron tunnelling in atoms. *Nature*, **446**:627–632, 2007.
- [16] X. Xie, S. Roither, D. Kartashov, E. Persson, D. G. Arbó, L. Zhang, S. Gräfe, M. S. Schöffler, J. Burgdörfer, A. Baltuška, and M. Kitzler. Attosecond probe of valence-electron wave packets by subcycle sculpted laser fields. *Phys. Rev. Lett.*, **108**:193004, 2012.
- [17] M. Ferray, A. L’Huillier, X. F. Li, L. A. Lompre, G. Mainfray, and C. Manus. Multiple-harmonic conversion of 1064 nm radiation in rare gases. *J. Phys. B: At., Mol. Opt. Phys.*, **21**:L31, 1988.
- [18] A. McPherson, G. Gibson, H. Jara, U. Johann, Ting S. Luk, I. A. McIntyre, K. Boyer, and C. K. Rhodes. Studies of multiphoton production of vacuum-ultraviolet radiation in the rare gases. *J. Opt. Soc. Am. B*, **4**:595–601, 1987.
- [19] C. Neidel, J. Klei, C. H. Yang, A. Rouzée, M. J. Vrakking, K. Klünder, M. Miranda, C. L. Arnold, T. Fordell, A. L’Huillier, M. Gisselbrecht, P. Johnsson, M. P. Dinh, E. Suraud, P. G. Reinhard, V. Despré, M. A. Marques, and F. Lépine. Probing time-dependent molecular dipoles on the attosecond time scale. *Phys. Rev. Lett.*, **111**:033001, 2013.
- [20] M. Drescher, M. Hentschel, R. Kienberger, M. Uiberacker, V. Yakovlev, A. Scrinzi, T. Westerwalbesloh, U. Kleineberg, U. Heinzmann, and F. Krausz. Time-resolved atomic inner-shell spectroscopy. *Nature*, **419**:803–807, 2002.
- [21] M. Schultze, M. Fiess, N. Karpowicz, J. Gagnon, M. Korbman, M. Hofstetter, S. Neppl, A. L. Cavalieri, Y. Komninos, T. Mercouris, C. A. Nicolaides, R. Pa-

- zourek, S. Nagele, J. Feist, J. Burgdörfer, A. M. Azzeer, R. Ernstorfer, R. Kienberger, U. Kleineberg, E. Goulielmakis, F. Krausz, and V. S. Yakovlev. Delay in photoemission. *Science*, **328**:1658–1662, 2010.
- [22] L. Seiffert, Q. Liu, S. Zherebtsov, A. Trabattoni, P. Rupp, M. C. Castrovilli, M. Galli, F. Süßmann, K. Wintersperger, J. Stierle, G. Sansone, L. Poletto, F. Frassetto, I. Halfpap, V. Mondes, C. Graf, E. Rühl, F. Krausz, M. Nisoli, T. Fennel, F. Calegari, and M. F. Kling. Attosecond chronoscopy of electron scattering in dielectric nanoparticles. *Nat. Phys.*, **13**:766–770, 2017.
- [23] M. Ossiander, J. Riemensberger, S. Neppl, M. Mittermair, M. Schäffer, A. Duensing, M. S. Wagner, R. Heider, M. Wurzer, M. Gerl, M. Schnitzenbaumer, J. V. Barth, F. Libisch, C. Lemell, J. Burgdörfer, P. Feulner, and R. Kienberger. Absolute timing of the photoelectric effect. *Nature*, **561**:374–377, 2018.
- [24] S. Arslanagic and R. W. Ziolkowski. Highly Subwavelength, Superdirective Cylindrical Nanoantenna. *Phys. Rev. Lett.*, **120**:237401, 2018.
- [25] J. A. Schuller, E. S. Barnard, W. Cai, Y. C. Jun, J. S. White, and M. L. Brongersma. Plasmonics for extreme light concentration and manipulation. *Nat. Mater.*, **9**:193–204, 2010.
- [26] D. M. Koller, A. Hohenau, H. Ditlbacher, N. Galler, F. Reil, F. R. Aussenegg, A. Leitner, E. J. W. List, and J. R. Krenn. Organic plasmon-emitting diode. *Nat. Photonics*, **2**:684–687, 2008.
- [27] A. L. Falk, F. H. L. Koppens, C. L. Yu, K. Kang, N. de Leon Snapp, Alexey V. Akimov, M.-H. Jo, M. D. Lukin, and H. Park. Near-field electrical detection of optical plasmons and single-plasmon sources. *Nat. Phys.*, **5**:475–479, 2009.
- [28] J. N. Anker, W. P. Hall, O. Lyandres, N. C. Shah, J. Zhao, and R. P. Van Duyne. Biosensing with plasmonic nanosensors. *Nat. Mater.*, **7**:442–53, 2008.
- [29] V. E. Ferry, L. A. Sweatlock, D. Pacifici, and H. A. Atwater. Plasmonic nanostructure design for efficient light coupling into solar cells. *Nano Lett.*, **8**:4391–4397, 2008.
- [30] M. Krüger, M. Schenk, and P. Hommelhoff. Attosecond control of electrons emitted from a nanoscale metal tip. *Nature*, **475**:78–81, 2011.
- [31] J. Hoffrogge, J. P. Stein, M. Krüger, M. Förster, J. Hammer, D. Ehberger, P. Baum, and P. Hommelhoff. Tip-based source of femtosecond electron pulses at 30 keV. *J. Appl. Phys.*, **115**:094506, 2014.

- [32] M. Gulde, S. Schweda, G. Storeck, M. Maiti, H. K. Yu, A. M. Wodtke, S. Schäfer, and C. Ropers. Imaging techniques. Ultrafast low-energy electron diffraction in transmission resolves polymer/graphene superstructure dynamics. *Science*, **345**:200–204, 2014.
- [33] P. Baum, D. S. Yang, and A. H. Zewail. 4D visualization of transitional structures in phase transformations by electron diffraction. *Science*, **318**:788–792, 2007.
- [34] Q. Xiang, J. Yu, and M. Jaroniec. Synergetic effect of MoS₂ and graphene as cocatalysts for enhanced photocatalytic H₂ production activity of TiO₂ nanoparticles. *J. Am. Chem. Soc.*, **134**:6575–6578, 2012.
- [35] C. Clavero. Plasmon-induced hot-electron generation at nanoparticle/metal-oxide interfaces for photovoltaic and photocatalytic devices. *Nat. Photonics*, **8**:95–103, 2014.
- [36] J. M. Shull and C. F. McKee. Theoretical models of interstellar shocks. I. Radiative transfer and UV precursors. *Astrophys. J.*, **227**:131, 1979.
- [37] M. I. Boulos, P. Fauchais, and E. Pfender. *Thermal plasmas: fundamentals and applications*. Springer Science + Business Media, 2013.
- [38] M. C. M. van de Sanden, J. M. de Regt, and D. C. Schram. The behaviour of heavy particles in the expanding plasma jet in argon. *Plasma Sources Sci. Technol.*, **3**:501–510, 1994.
- [39] V. S. Mukhovatov and V. D. Shafranov. Plasma Equilibrium in a Tokamak. *Nucl. Fusion*, **11**:605, 1971.
- [40] Y. P. Raizer. Optical discharges. *Sov. Phys. Usp.*, **23**:789–806, 1980.
- [41] R. Trebino. *Frequency-Resolved Optical Gating The Measurement of Ultrashort Laser Pulses*. Springer Science+Business Media, New York, 2000.
- [42] K. H. Hong, J. H. Kim, Y. H. Kang, and C. H. Nam. Time–frequency analysis of chirped femtosecond pulses using Wigner distribution function. *Appl. Phys. B*, **74**:S231–S236, 2014.
- [43] F. Lépine, M. Y. Ivanov, and M. J. J. Vrakking. Attosecond molecular dynamics: fact or fiction? *Nat. Photonics*, **8**:195–204, 2014.
- [44] L. V. Keldysh. Ionization in the field of a strong electromagnetic wave. *Zh. Eksp. Teor. Fiz.*, **47**:1945, 1964.
- [45] L. D. Landau and E. M. Lifshitz. *Quantum Mechanics, Nonrelativistic Theory*. Fizmatgiz, Moscow, 1963.

- [46] J. R. Oppenheimer. Three Notes on the Quantum Theory of Aperiodic Effects. *Phys. Rev.*, **31**:66–81, 1928.
- [47] F. H. M. Faisal. Collision of electrons with laser photons in a background potential. *J. Phys. B: At. Mol. Phys.*, **6**:L312–L315, 1973.
- [48] H. R. Reiss. Effect of an intense electromagnetic field on a weakly bound system. *Phys. Rev. A*, **22**:1786–1813, 1980.
- [49] M. V. Ammosov, N. B. Delone, and V. P. Krainov. Tunnelling ionization of complex atoms and of atomic ions in an alternating electromagnetic field. *Sov. Phys. JETP*, **64**:1191–1194, 1986.
- [50] J. Muth-Bohm, A. Becker, and F. H. Faisal. Suppressed molecular ionization for a class of diatomics in intense femtosecond laser fields. *Phys. Rev. Lett.*, **85**:2280–3, 2000.
- [51] T. K. Kjeldsen and L. B. Madsen. Strong-field ionization of N₂: length and velocity gauge strong-field approximation and tunnelling theory. *J. Phys. B: At., Mol. Opt. Phys.*, **37**:2033–2044, 2004.
- [52] X. M. Tong, Z. X. Zhao, and C. D. Lin. Theory of molecular tunneling ionization. *Phys. Rev. A*, **66**:033402, 2002.
- [53] S.-F. Zhao, C. Jin, A.-T. Le, T. F. Jiang, and C. D. Lin. Determination of structure parameters in strong-field tunneling ionization theory of molecules. *Phys. Rev. A*, **81**:033423, 2010.
- [54] S.-F. Zhao, J. L. Xu, C. Jin, A.-T. Le, and C. D. Lin. Effect of orbital symmetry on the orientation dependence of strong field tunnelling ionization of nonlinear polyatomic molecules. *J. Phys. B: At., Mol. Opt. Phys.*, **44**:035601, 2011.
- [55] J.-P. Wang, W. Li, and S.-F. Zhao. Structure parameters in molecular tunneling ionization theory. *Journal of Physics: Conference Series*, **488**:032028, 2014.
- [56] S.-F. Zhao, J.-K. Li, G.-L. Wang, P.-C. Li, and X.-X. Zhou. Accurate Structure Parameters for Tunneling Ionization Rates of Gas-Phase Linear Molecules. *Communications in Theoretical Physics*, **67**:289, 2017.
- [57] A. M. Perelomov, V. S. Popov, and M. V. Terent'ev. Ionization of Atoms in an Alternating Electric Field. *Sov. Phys. JETP*, **23**:924, 1966.
- [58] A. M. Perelomov, V. S. Popov, and M. V. Terent'ev. Ionization of Atoms in an Alternating Electric Field: II. *Sov. Phys. JETP*, **24**:207, 1967.

- [59] P. B. Corkum. Plasma perspective on strong field multiphoton ionization. *Phys. Rev. Lett.*, **71**:1994–1997, 1993.
- [60] F. Krausz and M. Ivanov. Attosecond physics. *Rev. Mod. Phys.*, **81**:163–234, 2009.
- [61] P. M. Paul, E. S. Toma, P. Breger, G. Mullot, F. Augé, P. Balcou, H. G. Muller, and P. Agostini. Observation of a train of attosecond pulses from high harmonic generation. *Science*, **292**:1689–1692, 2001.
- [62] J. L. Krause, K. J. Schafer, and K. C. Kulander. High-order harmonic generation from atoms and ions in the high intensity regime. *Phys. Rev. Lett.*, **68**:3535–3538, 1992.
- [63] J. J. Macklin, J. D. Kmetec, and C. L. Gordon III. High-order harmonic generation using intense femtosecond pulses. *Phys. Rev. Lett.*, **70**:766, 1993.
- [64] T. Popmintchev, M.-C. Chen, P. Arpin, M. M. Murnane, and H. C. Kapteyn. The attosecond nonlinear optics of bright coherent X-ray generation. *Nat. Photonics*, **4**:822–832, 2010.
- [65] M. Hentschel, R. Kienberger, C. Spielmann, G. A. Reider, N. Milosevic, T. Brabec, P. Corkum, U. Heinzmann, M. Drescher, and F. Krausz. Attosecond metrology. *Nature*, **414**:509–513, 2001.
- [66] E. Goulielmakis, M. Schultze, M. Hofstetter, V. S. Yakovlev, J. Gagnon, M. Uiberacker, A. L. Aquila, E. M. Gullikson, D. T. Attwood, R. Kienberger, F. Krausz, and U. Kleineberg. Single-cycle nonlinear optics. *Science*, **320**:1614–1617, 2008.
- [67] T. Gaumnitz, A. Jain, Y. Pertot, M. Huppert, I. Jordan, F. Ardana-Lamas, and H. J. Worner. Streaking of 43-attosecond soft-X-ray pulses generated by a passively CEP-stable mid-infrared driver. *Opt. Express*, **25**:27506–27518, 2017.
- [68] G. Sansone, E. Benedetti, F. Calegari, C. Vozzi, L. Avaldi, R. Flammini, L. Poletto, P. Villoresi, C. Altucci, R. Velotta, S. Stagira, S. De Silvestri, and M. Nisoli. Isolated single-cycle attosecond pulses. *Science*, **314**:443–446, 2006.
- [69] K. Zhao, Q. Zhang, M. Chini, Y. Wu, X. Wang, and Z. Chang. Tailoring a 67 attosecond pulse through advantageous phase-mismatch. *Opt. Lett.*, **37**:3891, 2012.
- [70] F. Ferrari, F. Calegari, M. Lucchini, C. Vozzi, S. Stagira, G. Sansone, and M. Nisoli. High-energy isolated attosecond pulses generated by above-saturation few-cycle fields. *Nat. Photonics*, **4**:875–879, 2010.
- [71] K. T. Kim, C. Zhang, T. Ruchon, J-F. Hergott, T. Augustine, D. M. Villeneuve, P. B. Corkum, and F. Quéré. Photonic streaking of attosecond pulse trains. *Nat. Photonics*, **7**:651–656, 2013.

- [72] T. J. Hammond, G. G. Brown, K. T. Kim, D. M. Villeneuve, and P. B. Corkum. Attosecond pulses measured from the attosecond lighthouse. *Nat. Photonics*, **10**: 171–175, 2016.
- [73] C. M. Heyl, S. N. Bengtsson, S. Carlström, J. Mauritsson, C. L. Arnold, and A. L’Huillier. Noncollinear optical gating. *New J. Phys.*, **16**:109501, 2014.
- [74] M. Busuladžić, A. Gazibegović-Busuladžić, and D. B. Milošević. High-order above-threshold ionization in a laser field: Influence of the ionization potential on the high-energy cutoff. *Laser Phys.*, **16**:289–293, 2006.
- [75] V. V. Suran and I. P. Zapesochnyi. Observation of Sr^{2+} in multiple-photon ionization of strontium. *Sov. Tech. Phys. Lett.*, **1**:420–425, 1975.
- [76] A. L’Huillier, L. A. Lompre, G. Mainfray, and C. Manus. Multiply Charged Ions Formed by Multiphoton Absorption Processes in the Continuum. *Phys. Rev. Lett.*, **48**:1814–1817, 1982.
- [77] A. l’Huillier, L. A. Lompre, G. Mainfray, and C. Manus. Multiply charged ions induced by multiphoton absorption in rare gases at 0.53 μm . *Phys. Rev. A*, **27**: 2503–2512, 1983.
- [78] B. Walker, B. Sheehy, L. F. DiMauro, P. Agostini, K. J. Schafer, and K. C. Kulander. Precision measurement of strong field double ionization of helium. *Phys. Rev. Lett.*, **73**:1227–1230, 1994.
- [79] H. Niikura, F. Légaré, R. Hasbani, A. D. Bandrauk, M. Y. Ivanov, D. M. Villeneuve, and P. B. Corkum. Sub-laser-cycle electron pulses for probing molecular dynamics. *Nature*, **417**:917–922, 2002.
- [80] S. Gräfe and M. Y. Ivanov. Effective fields in laser-driven electron recollision and charge localization. *Phys. Rev. Lett.*, **99**:163603, 2007.
- [81] P. Agostini, F. Fabre, G. Mainfray, G. Petite, and N. K. Rahman. Free-free transitions following six-photon ionization of xenon atoms. *Phys. Rev. Lett.*, **42**:1127, 1979.
- [82] M. Drescher, M. Hentschel, R. Kienberger, G. Tempea, C. Spielmann, G. A. Reider, P. B. Corkum, and F. Krausz. X-ray pulses approaching the attosecond frontier. *Science*, **291**:1923–1927, 2001.
- [83] J. Itatani, F. Quere, G. L. Yudin, M. Y. Ivanov, F. Krausz, and P. B. Corkum. Attosecond streak camera. *Phys. Rev. Lett.*, **88**:173903, 2002.

- [84] M. Kitzler, N. Milosevic, A. Scrinzi, F. Krausz, and T. Brabec. Quantum theory of attosecond XUV pulse measurement by laser dressed photoionization. *Phys. Rev. Lett.*, **88**:173904, 2002.
- [85] Y. Mairesse and F. Quéré. Frequency-resolved optical gating for complete reconstruction of attosecond bursts. *Phys. Rev. A*, **71**:011401, 2005.
- [86] E. Goulielmakis, M. Uiberacker, R. Kienberger, A. Baltuska, V. Yakovlev, A. Scrinzi, T. Westerwalbesloh, U. Kleineberg, U. Heinzmann, M. Drescher, and F. Krausz. Direct measurement of light waves. *Science*, **305**:1267–1269, 2004.
- [87] M. Wickenhauser, J. Burgdörfer, F. Krausz, and M. Drescher. Time resolved Fano resonances. *Phys. Rev. Lett.*, **94**:023002, 2005.
- [88] V. Véliard, R. Taïeb, and A. Maquet. Phase dependence of (N+1)-color (N>1) ir-uv photoionization of atoms with higher harmonics. *Phys. Rev. A*, **54**:721–728, 1996.
- [89] E. S. Toma and H. G. Muller. Calculation of matrix elements for mixed extreme-ultraviolet–infrared two-photon above-threshold ionization of argon. *J. Phys. B: At., Mol. Opt. Phys.*, **35**:3435–3442, 2002.
- [90] K. Klünder, J. M. Dahlström, M. Gisselbrecht, T. Fordell, M. Swoboda, D. Guenot, P. Johnsson, J. Caillat, J. Mauritsson, A. Maquet, R. Taïeb, and A. L’Huillier. Probing single-photon ionization on the attosecond time scale. *Phys. Rev. Lett.*, **106**:143002, 2011.
- [91] D. Guénot, K. Klünder, C. L. Arnold, D. Kroon, J. M. Dahlström, M. Miranda, T. Fordell, M. Gisselbrecht, P. Johnsson, J. Mauritsson, E. Lindroth, A. Maquet, R. Taïeb, A. L’Huillier, and A. S. Kheifets. Photoemission-time-delay measurements and calculations close to the 3s-ionization-cross-section minimum in Ar. *Phys. Rev. A*, **85**:053424, 2012.
- [92] F. Calegari, G. Sansone, S. Stagira, C. Vozzi, and M. Nisoli. Advances in attosecond science. *J. Phys. B: At., Mol. Opt. Phys.*, **49**:062001, 2016.
- [93] P. Eckle, M. Smolarski, P. Schlup, J. Biegert, A. Staudte, M. Schöffler, H.G. Muller, R. Dörner, and U. Keller. Attosecond angular streaking. *Nat. Phys.*, **4**:565–570, 2008.
- [94] A. N. Pfeiffer, C. Cirelli, M. Smolarski, R. Dörner, and U. Keller. Timing the release in sequential double ionization. *Nat. Phys.*, **7**:428–433, 2011.
- [95] P. H. Bucksbaum. The future of attosecond spectroscopy. *Science*, **317**:766–769, 2007.

- [96] P. B. Corkum and Ferenc Krausz. Attosecond science. *Nat. Phys.*, **3**:381–387, 2007.
- [97] M. F. Kling and M. J. J. Vrakking. Attosecond electron dynamics. *Annu Rev Phys Chem*, **59**:463–492, 2008.
- [98] L. Eisenbud. *Formal properties of nuclear collisions PhD Thesis Princeton University*. PhD thesis, Princeton, 1948.
- [99] E. P. Wigner. Lower Limit for the Energy Derivative of the Scattering Phase Shift. *Phys. Rev.*, **98**:145–147, 1955.
- [100] F. T. Smith. Lifetime Matrix in Collision Theory. *Phys. Rev.*, **118**:349–356, 1960.
- [101] W. Brenig and R. Haag. Allgemeine Quantentheorie der Stoßprozesse. *Fortschr. Phys.*, **7**:183–242, 1959.
- [102] D. Bollé, F. Gesztesy, and H. Grosse. Time delay for long-range interactions. *J. Math. Phys.*, **24**:1529–1541, 1983.
- [103] R. Pazourek, S. Nagele, and J. Burgdörfer. Time-resolved photoemission on the attosecond scale: opportunities and challenges. *Faraday Discussions*, **163**:353, 2013.
- [104] C. W. Clark. Coulomb phase shift. *Am. J. Phys.*, **47**:683–684, 1979.
- [105] R. Abrines and I. C. Percival. Classical Theory of Charge Transfer and Ionization of Hydrogen Atoms by Protons. *Proc. Phys. Soc.*, **88**:861–872, 1966.
- [106] K. I. Dimitriou, D. G. Arbó, S. Yoshida, E. Persson, and J. Burgdörfer. Origin of the double-peak structure in the momentum distribution of ionization of hydrogen atoms driven by strong laser fields. *Phys. Rev. A*, **70**:061401, 2004.
- [107] J. M. Dahlström, D. Guénot, K. Klünder, M. Gisselbrecht, J. Mauritsson, A. L’Huillier, A. Maquet, and R. Taïeb. Theory of attosecond delays in laser-assisted photoionization. *Chem. Phys.*, **414**:53–64, 2013.
- [108] S. Nagele, R. Pazourek, J. Feist, K. Doblhoff-Dier, C. Lemell, K. Tókési, and J. Burgdörfer. Time-resolved photoemission by attosecond streaking: extraction of time information. *J. Phys. B: At., Mol. Opt. Phys.*, **44**:081001, 2011.
- [109] C. H. Zhang and U. Thumm. Electron-ion interaction effects in attosecond time-resolved photoelectron spectra. *Phys. Rev. A*, **82**:043405, 2010.
- [110] M. Ivanov and O. Smirnova. How accurate is the attosecond streak camera? *Phys. Rev. Lett.*, **107**:213605, 2011.
- [111] J. C. Baggesen and L. B. Madsen. Polarization effects in attosecond photoelectron spectroscopy. *Phys. Rev. Lett.*, **104**:043602, 2010.

- [112] J. C. Baggesen and L. B. Madsen. Erratum: Polarization Effects in Attosecond Photoelectron Spectroscopy. *Phys. Rev. Lett.*, **104**:209903, 2010.
- [113] E. S. Smyth, J. S. Parker, and K. T. Taylor. Numerical integration of the time-dependent Schrödinger equation for laser-driven helium. *Comput. Phys. Commun.*, **114**:1–14, 1998.
- [114] B. I. Schneider, J. Feist, S. Nagele, R. Pazourek, S. Hu, L. A. Collins, and J. Burgdörfer. Recent Advances in Computational Methods for the Solution of the Time-Dependent Schrödinger Equation for the Interaction of Short, Intense Radiation with One and Two Electron Systems. In *Quantum Dynamic Imaging*, pages 149–208. Springer, 2011.
- [115] J. Feist, S. Nagele, R. Pazourek, E. Persson, B. I. Schneider, L. A. Collins, and J. Burgdörfer. Nonsequential two-photon double ionization of helium. *Phys. Rev. A*, **77**:043420, 2008.
- [116] S. Nagele, R. Pazourek, J. Feist, and J. Burgdörfer. Time shifts in photoemission from a fully correlated two-electron model system. *Phys. Rev. A*, **85**:033401, 2012.
- [117] M. Y. Amusia, A. Z. Msezane, and V. R. Shaginyan. Density Functional Theory versus the Hartree–Fock Method: Comparative Assessment. *Phys. Scr.*, **68**:C133–C140, 2003.
- [118] P. Hohenberg and W. Kohn. Inhomogeneous Electron Gas. *Phys. Rev. B*, **136**:B864–B871, 1964.
- [119] W. Kohn and L. J. Sham. Self-Consistent Equations Including Exchange and Correlation Effects. *Phys. Rev.*, **140**:A1133–A1138, 1965.
- [120] E. Runge and E. K. U. Gross. Density-Functional Theory for Time-Dependent Systems. *Phys. Rev. Lett.*, **52**:997–1000, 1984.
- [121] E. K. U. Gross and W. Kohn. Time-Dependent Density-Functional Theory. *Adv. Quantum Chem.*, **21**:255–291, 1990.
- [122] J. Hafner. Ab-initio simulations of materials using VASP: Density-functional theory and beyond. *J. Comput. Chem.*, **29**:2044–2078, 2008.
- [123] F. Calvayrac, P.-G. Reinhard, E. Suraud, and C. A. Ullrich. Nonlinear electron dynamics in metal clusters. *Phys. Rep.*, **337**:493–578, 2000.
- [124] S. W. Scully, E. D. Emmons, M. F. Gharaibeh, R. A. Phaneuf, A. L. Kilcoyne, A. S. Schlachter, S. Schippers, A. Müller, H. S. Chakraborty, M. E. Madjet, and J. M. Rost. Photoexcitation of a volume plasmon in C_{60} ions. *Phys. Rev. Lett.*, **94**:065503, 2005.

- [125] M. E. Madjet, H. S. Chakraborty, J. M. Rost, and S. T. Manson. Photoionization of C_{60} : a model study. *J. Phys. B: At., Mol. Opt. Phys.*, **41**:105101, 2008.
- [126] H. W. Kroto, J. R. Heath, S. C. O'Brien, R. F. Curl, and R. E. Smalley. C_{60} : Buckminsterfullerene. *Nature*, **318**:162–163, 1985.
- [127] D. Bohm and D. Pines. A Collective Description of Electron Interactions. I. Magnetic Interactions. *Phys. Rev.*, **82**:625–634, 1951.
- [128] D. Pines and D. Bohm. A Collective Description of Electron Interactions: II. Collective *vs* Individual Particle Aspects of the Interactions. *Phys. Rev.*, **85**:338–353, 1952.
- [129] D. Bohm and D. Pines. A Collective Description of Electron Interactions: III. Coulomb Interactions in a Degenerate Electron Gas. *Phys. Rev.*, **92**:609–625, 1953.
- [130] C. J. Powell and J. B. Swan. Origin of the Characteristic Electron Energy Losses in Aluminum. *Phys. Rev.*, **115**:869–875, 1959.
- [131] R. A. Phaneuf. Plasmons in Fullerene Molecules. In K. D. Sattler, editor, *Handbook of Nanophysics*, Volume 2. CRC Press, 2011.
- [132] G. F. Bertsch, A. Bulgac, D. Tomanek, and Y. Wang. Collective plasmon excitations in C_{60} clusters. *Phys. Rev. Lett.*, **67**:2690–2693, 1991.
- [133] I. V. Hertel, H. Steger, J. de Vries, B. Weisser, C. Menzel, B. Kamke, and W. Kamke. Giant plasmon excitation in free C_{60} and C_{70} molecules studied by photoionization. *Phys. Rev. Lett.*, **68**:784–787, 1992.
- [134] M. Brack. The physics of simple metal clusters: self-consistent jellium model and semiclassical approaches. *Rev. Mod. Phys.*, **65**:677–732, 1993.
- [135] M. J. Puska and R. M. Nieminen. Photoabsorption of atoms inside C_{60} . *Phys. Rev. A*, **47**:1181–1186, 1993.
- [136] G. Wendin and B. Wästberg. Many-electron effects in BaC_{60} : Collective response and molecular effects in optical conductivity and photoionization. *Phys. Rev. B*, **48**:14764–14767, 1993.
- [137] W. Kohn. Nobel Lecture: Electronic structure of matter—wave functions and density functionals. *Rev. Mod. Phys.*, **71**:1253–1266, 1999.
- [138] A. Rüdél, R. Hentges, U. Becker, H. S. Chakraborty, M. E. Madjet, and J. M. Rost. Imaging delocalized electron clouds: photoionization of C_{60} in Fourier reciprocal space. *Phys. Rev. Lett.*, **89**:125503, 2002.

- [139] A. S. Moskalenko, Y. Pavlyukh, and J. Berakdar. Attosecond tracking of light absorption and refraction in fullerenes. *Phys. Rev. A*, **86**:013202, 2012.
- [140] V. K. Ivanov, G. Y. Kashenock, R. G. Polozkov, and A. V. Solov'yov. Photoionization cross sections of the fullerenes C_{20} and C_{60} calculated in a simple spherical model. *J. Phys. B: At., Mol. Opt. Phys.*, **34**:L669–L677, 2001.
- [141] M. Y. Amusia, N. A. Cherepkov, and L. V. Chernysheva. Cross section for the photoionization of noble-gas atoms with allowance for multielectron correlations. *Zh. Eksp. Teor. Fiz.*, **60**:160–174, 1971.
- [142] C. Yannouleas, R. A. Broglia, M. Brack, and P. F. Bortignon. Fragmentation of the photoabsorption strength in neutral and charged metal microclusters. *Phys. Rev. Lett.*, **63**:255–258, 1989.
- [143] R. G. Polozkov, V. K. Ivanov, and A. V. Solov'yov. Photoionization of the fullerene ion C_{60}^+ . *J. Phys. B: At., Mol. Opt. Phys.*, **38**:4341–4348, 2005.
- [144] A. S. Kheifets and I. A. Ivanov. Delay in atomic photoionization. *Phys. Rev. Lett.*, **105**:233002, 2010.
- [145] A. S. Kheifets. Time delay in valence-shell photoionization of noble-gas atoms. *Phys. Rev. A*, **87**:063404, 2013.
- [146] A. Zangwill and P. Soven. Density-functional approach to local-field effects in finite systems: Photoabsorption in the rare gases. *Phys. Rev. A*, **21**:1561–1572, 1980.
- [147] W. Ekardt. Size-dependent photoabsorption and photoemission of small metal particles. *Phys. Rev. B*, **31**:6360–6370, 1985.
- [148] P. A. Hervieux, M. E. Madjet, and H. Benali. Capture of low-energy electrons by simple closed-shell metal clusters. *Phys. Rev. A*, **65**:023202, 2002.
- [149] G. Dixit, H. S. Chakraborty, and M. E. Madjet. Time delay in the recoiling valence photoemission of an endohedrally confined C_{60} . *Phys. Rev. Lett.*, **111**:203003, 2013.
- [150] G. Onida, L. Reining, and A. Rubio. Electronic excitations: density-functional versus many-body Green's-function approaches. *Rev. Mod. Phys.*, **74**:601–659, 2002.
- [151] P. Lambin, A. A. Lucas, and J.-P. Vigneron. Polarization waves and van der Waals cohesion of C_{60} fullerite. *Phys. Rev. B*, **46**:1794–1803, 1992.
- [152] A. V. Korol and A. V. Solov'yov. Comment on "Photoexcitation of a Volume Plasmon in C_{60} Ions". *Phys. Rev. Lett.*, **98**:179601, 2007.

- [153] S. W. Scully, E. D. Emmons, M. F. Gharaibeh, R. A. Phaneuf, A. L. Kilcoyne, A. S. Schlachter, S. Schippers, A. Müller, H. S. Chakraborty, M. E. Madjet, and J. M. Rost. Scully *et al.* Reply:. *Phys. Rev. Lett.*, **98**:179602, 2007.
- [154] B. M. Reinhard, M. Siu, H. Agarwal, A. P. Alivisatos, and J. Liphardt. Calibration of dynamic molecular rulers based on plasmon coupling between gold nanoparticles. *Nano Lett.*, **5**:2246–2252, 2005.
- [155] C. Sönnichsen, B. M. Reinhard, J. Liphardt, and A. P. Alivisatos. A molecular ruler based on plasmon coupling of single gold and silver nanoparticles. *Nat. Biotechnol.*, **23**:741–745, 2005.
- [156] U. Kreibig. Electronic properties of small silver particles: the optical constants and their temperature dependence. *J. Phys. F: Met. Phys.*, **4**:999–1014, 1974.
- [157] S. Banerjee, J. Das, R. P. Alvarez, and S. Santra. Silicananoparticles as a reusable catalyst: a straightforward route for the synthesis of thioethers, thioesters, vinyl thioethers and thio-Michael adducts under neutral reaction conditions. *New J. Chem.*, **34**:302–306, 2010.
- [158] T. Yatsui, T. Imoto, T. Mochizuki, K. Kitamura, and T. Kawazoe. Dressed-photon-phonon (DPP)-assisted visible- and infrared-light water splitting. *Sci. Rep.*, **4**:4561, 2014.
- [159] T. Novakov and J. E. Penner. Large Contribution of Organic Aerosols to Cloud-Condensation-Nuclei Concentrations. *Nature*, **365**:823–826, 1993.
- [160] V. Ramanathan, P. J. Crutzen, J. T. Kiehl, and D. Rosenfeld. Aerosols, climate, and the hydrological cycle. *Science*, **294**:2119–2124, 2001.
- [161] J. Becker, A. Trügler, A. Jakab, U. Hohenester, and C. Sönnichsen. The Optimal Aspect Ratio of Gold Nanorods for Plasmonic Bio-sensing. *Plasmonics*, **5**:161–167, 2010.
- [162] S. Nie and S. R. Emory. Probing Single Molecules and Single Nanoparticles by Surface-Enhanced Raman Scattering. *Science*, **275**:1102–1106, 1997.
- [163] K. Kneipp, H. Kneipp, I. Itzkan, R. R. Dasari, and M. S. Feld. Surface-enhanced non-linear Raman scattering at the single-molecule level. *Chem. Phys.*, **247**:155–162, 1999.
- [164] T. Yatsui, M. Yamaguchi, and K. Nobusada. Nano-scale chemical reactions based on non-uniform optical near-fields and their applications. *Progress in Quantum Electronics*, **55**:166–194, 2017.

- [165] T. Yatsui, W. Nomura, M. Naruse, and M. Ohtsu. Realization of an atomically flat surface of diamond using dressed photon–phonon etching. *J. Phys. D: Appl. Phys.*, **45**:475302, 2012.
- [166] F. Krausz and M. I. Stockman. Attosecond metrology: from electron capture to future signal processing. *Nat. Photonics*, **8**:205–213, 2014.
- [167] F. Süßmann, L. Seiffert, S. Zherebtsov, V. Mondes, J. Stierle, M. Arbeiter, J. Plenge, P. Rupp, C. Peltz, A. Kessel, S. A. Trushin, B. Ahn, D. Kim, C. Graf, E. Rühl, M. F. Kling, and T. Fennel. Field propagation-induced directionality of carrier-envelope phase-controlled photoemission from nanospheres. *Nat. Commun.*, **6**:7944, 2015.
- [168] L. Seiffert, F. Süßmann, S. Zherebtsov, P. Rupp, C. Peltz, E. Rühl, M. F. Kling, and T. Fennel. Competition of single and double rescattering in the strong-field photoemission from dielectric nanospheres. *Appl. Phys. B*, **122**:1–9, 2016.
- [169] S. Thomas, M. Kruger, M. Forster, M. Schenk, and P. Hommelhoff. Probing of Optical Near-Fields by Electron Rescattering on the 1 nm Scale. *Nano Lett.*, **13**:4790–4794, 2013.
- [170] P. Dombi, A. Hörl, P. Rácz, I. Márton, A. Trügler, J. R. Krenn, and U. Hohenester. Ultrafast Strong-Field Photoemission from Plasmonic Nanoparticles. *Nano Lett.*, **13**:674–678, 2013.
- [171] P. Racz, Z. Papa, I. Marton, J. Budai, P. Wrobel, T. Stefaniuk, C. Prietl, J. R. Krenn, and P. Dombi. Measurement of Nanoplasmonic Field Enhancement with Ultrafast Photoemission. *Nano Lett.*, **17**:1181–1186, 2017.
- [172] B. Förg, J. Schötz, F. Süßmann, M. Förster, M. Krüger, B. Ahn, W. A. Okell, K. Wintersperger, S. Zherebtsov, A. Guggenmos, V. Pervak, A. Kessel, S. A. Trushin, A. M. Azzeer, M. I. Stockman, D. Kim, F. Krausz, P. Hommelhoff, and M. F. Kling. Attosecond nanoscale near-field sampling. *Nat. Commun.*, **7**:11717, 2016.
- [173] R. W. Taylor, R. J. Coulston, F. Biedermann, S. Mahajan, J. J. Baumberg, and O. A. Scherman. In situ SERS monitoring of photochemistry within a nanojunction reactor. *Nano Lett.*, **13**:5985–5990, 2013.
- [174] D. D. Hickstein, F. Dollar, J. L. Ellis, K. J. Schnitzenbaumer, K. E. Keister, G. M. Petrov, C. Ding, B. B. Palm, J. A. Gaffney, M. E. Foord, S. B. Libby, G. Dukovic, J. L. Jimenez, H. C. Kapteyn, M. M. Murnane, and W. Xiong. Mapping nanoscale absorption of femtosecond laser pulses using plasma explosion imaging. *ACS Nano*, **8**:8810–8, 2014.

- [175] W. Kautek, J. Krüger, M. Lenzner, S. Sartania, C. Spielmann, and F. Krausz. Laser ablation of dielectrics with pulse durations between 20 fs and 3 ps. *Appl. Phys. Lett.*, **69**:3146–3148, 1996.
- [176] J. Ullrich, R. Moshhammer, A. Dorn, R. Dörner, L. P. H. Schmidt, and H. Schmidt-Böcking. Recoil-ion and electron momentum spectroscopy: reaction-microscopes. *Rep. Prog. Phys.*, **66**:1463, 2003.
- [177] J. N. Shu, K. R. Wilson, M. Ahmed, and S. R. Leone. Coupling a versatile aerosol apparatus to a synchrotron: Vacuum ultraviolet light scattering, photoelectron imaging, and fragment free mass spectrometry. *Rev. Sci. Instrum.*, **77**:043106, 2006.
- [178] J. N. Shu, K. R. Wilson, M. Ahmed, S. R. Leone, C. Graf, and E. Rühl. Elastic light scattering from nanoparticles by monochromatic vacuum-ultraviolet radiation. *J. Chem. Phys.*, **124**:034707, 2006.
- [179] B. B. Baker Jr. Measuring trace impurities in air by infrared spectroscopy at 20 meters path and 10 atmospheres pressure. *Am. Ind. Hyg. Assoc. J.*, **35**:735–740, 1974.
- [180] N. B. Mears. *Method of forming fine mesh screens*. U.S. Patent Nr. 3,329,541, 1967.
- [181] D. A. Dahl. SIMION for the personal computer in reflection. *International Journal of Mass Spectrometry*, **200**:3–25, 2000.
- [182] D. Manura and D. A Dahl. *SIMION 8.0 User manual*. Scientific Instrument Services, 2007.
- [183] W. Stöber, A. Fink, and E. Bohn. Controlled growth of monodisperse silica spheres in the micron size range. *J. Colloid Interface Sci.*, **26**:62–69, 1968.
- [184] C. Graf and A. van Blaaderen. Metallodielectric colloidal core-shell particles for photonic applications. *Langmuir*, **18**:524–534, 2002.
- [185] A. van Blaaderen and A. P. M. Kentgens. Particle morphology and chemical microstructure of colloidal silica spheres made from alkoxy silanes. *J. Non-Cryst. Solids*, **149**:161–178, 1992.
- [186] M. Kübel, C. Burger, N. G. Kling, T. Pischke, L. Beaufore, I. Ben-Itzhak, G. G. Paulus, J. Ullrich, T. Pfeifer, R. Moshhammer, M. F. Kling, and B. Bergues. Complete characterization of single-cycle double ionization of argon from the nonsequential to the sequential ionization regime. *Phys. Rev. A*, **93**:053422, 2016.
- [187] D. Mathur, F. A. Rajgara, A. K. Dharmadhikari, and J. A. Dharmadhikari. Strong-field ionization of water by intense few-cycle laser pulses. *Phys. Rev. A*, **78**:023414, 2008.

- [188] K. M. A. Refaey and W. A. Chupka. Photoionization of the Lower Aliphatic Alcohols with Mass Analysis. *J. Chem. Phys.*, **48**:5205–5219, 1968.
- [189] P. Rupp, L. Seiffert, Q. Liu, F. Süßmann, B. Ahn, B. Förg, C. G. Schäfer, M. Gallei, V. Mondes, A. Kessel, S. Trushin, C. Graf, E. Rühl, J. Lee, M. S. Kim, D. E. Kim, T. Fennel, M. F. Kling, and S. Zherebtsov. Quenching of material dependence in few-cycle driven electron acceleration from nanoparticles under many-particle charge interaction. *J. Mod. Opt.*, **64**:995–1003, 2016.
- [190] L. Seiffert, P. Henning, P. Rupp, S. Zherebtsov, P. Hommelhoff, M. F. Kling, and T. Fennel. Trapping field assisted backscattering in the strong-field photoemission from dielectric nanospheres. *J. Mod. Opt.*, **64**:1–8, 2016.
- [191] J. A. Nelder and R. Mead. A Simplex Method for Function Minimization. *Comput. J.*, **7**:308–313, 1965.
- [192] J. C. Lagarias, J. A. Reeds, M. H. Wright, and P. E. Wright. Convergence Properties of the Nelder–Mead Simplex Method in Low Dimensions. *SIAM J. Optim.*, **9**:112–147, 1998.
- [193] A. A. Sorokin, S. V. Bobashev, T. Feigl, K. Tiedtke, H. Wabnitz, and M. Richter. Photoelectric effect at ultrahigh intensities. *Phys. Rev. Lett.*, **99**:213002, 2007.
- [194] L. Young, E. P. Kanter, B. Krassig, Y. Li, A. M. March, S. T. Pratt, R. Santra, S. H. Southworth, N. Rohringer, L. F. Dimauro, G. Doumy, C. A. Roedig, N. Berrah, L. Fang, M. Hoener, P. H. Bucksbaum, J. P. Cryan, S. Ghimire, J. M. Glowina, D. A. Reis, J. D. Bozek, C. Bostedt, and M. Messerschmidt. Femtosecond electronic response of atoms to ultra-intense X-rays. *Nature*, **466**:56–61, 2010.
- [195] Y. H. Jiang, A. Rudenko, O. Herrwerth, L. Foucar, M. Kurka, K. U. Kuhnel, M. Lezius, M. F. Kling, J. van Tilborg, A. Belkacem, K. Ueda, S. Dusterer, R. Treusch, C. D. Schroter, R. Moshhammer, and J. Ullrich. Ultrafast extreme ultraviolet induced isomerization of acetylene cations. *Phys. Rev. Lett.*, **105**:263002, 2010.
- [196] A. Barty, S. Boutet, M. J. Bogan, S. Hau-Riege, S. Marchesini, K. Sokolowski-Tinten, N. Stojanovic, R. Tobey, H. Ehrke, A. Cavalleri, S. Düsterer, M. Frank, S. Bajt, B. Woods, M. M. Seibert, J. Hajdu, R. Treusch, and H. N. Chapman. Ultrafast single-shot diffraction imaging of nanoscale dynamics. *Nat. Photonics*, **2**:415–419, 2008.
- [197] J. N. Clark, L. Beitra, G. Xiong, A. Higginbotham, D. M. Fritz, H. T. Lemke, D. Zhu, M. Chollet, G. J. Williams, M. Messerschmidt, B. Abbey, R. J. Harder, A. M. Korsunsky, J. S. Wark, and I. K. Robinson. Ultrafast three-dimensional imaging of lattice dynamics in individual gold nanocrystals. *Science*, **341**:56–59, 2013.

- [198] D. Milathianaki, S. Boutet, G. J. Williams, A. Higginbotham, D. Ratner, A. E. Gleason, M. Messerschmidt, M. M. Seibert, D. C. Swift, P. Hering, J. Robinson, W. E. White, and J. S. Wark. Femtosecond visualization of lattice dynamics in shock-compressed matter. *Science*, **342**:220–223, 2013.
- [199] D. Arnlund, L. C. Johansson, C. Wickstrand, A. Barty, G. J. Williams, E. Malmerberg, J. Davidsson, D. Milathianaki, D. P. DePonte, R. L. Shoeman, D. Wang, D. James, G. Katona, S. Westenhoff, T. A. White, A. Aquila, S. Bari, P. Berntsen, M. Bogan, T. B. van Driel, R. B. Doak, K. S. Kjaer, M. Frank, R. Fromme, I. Grotjohann, R. Henning, M. S. Hunter, R. A. Kirian, I. Kosheleva, C. Kupitz, et al. Visualizing a protein quake with time-resolved X-ray scattering at a free-electron laser. *Nat. Methods*, **11**:923–926, 2014.
- [200] K. R. Beyerlein, H. O. Jonsson, R. Alonso-Mori, A. Aquila, S. Bajt, A. Barty, R. Bean, J. E. Koglin, M. Messerschmidt, D. Ragazzon, D. Sokaras, G. J. Williams, S. Hau-Riege, S. Boutet, H. N. Chapman, N. Timneanu, and C. Caleman. Ultrafast nonthermal heating of water initiated by an X-ray Free-Electron Laser. *Proc. Natl. Acad. Sci. U.S.A.*, **115**:5652–5657, 2018.
- [201] T. Gorkhover, S. Schorb, R. Coffee, M. Adolph, L. Foucar, D. Rupp, A. Aquila, J. D. Bozek, S. W. Epp, B. Erk, L. Gumprecht, L. Holmegaard, A. Hartmann, R. Hartmann, G. Hauser, P. Holl, A. Hömke, P. Johnsson, N. Kimmel, K. Kühnel, M. Messerschmidt, C. Reich, A. Rouzée, B. Rudek, C. Schmidt, J. Schulz, H. Soltau, S. Stern, G. Weidenspointner, B. White, et al. Femtosecond and nanometre visualization of structural dynamics in superheated nanoparticles. *Nat. Photonics*, **10**:93–97, 2016.
- [202] C. Peltz, C. Varin, T. Brabec, and T. Fennel. Time-resolved x-ray imaging of anisotropic nanoplasma expansion. *Phys. Rev. Lett.*, **113**:133401, 2014.
- [203] C. Peltz, C. Varin, T. Brabec, and T. Fennel. Fully microscopic analysis of laser-driven finite plasmas using the example of clusters. *New J. Phys.*, **14**:065011, 2012.
- [204] C. Varin, C. Peltz, T. Brabec, and T. Fennel. Attosecond plasma wave dynamics in laser-driven cluster nanoplasmas. *Phys. Rev. Lett.*, **108**:175007, 2012.
- [205] S. H. Glenzer, O. L. Landen, P. Neumayer, R. W. Lee, K. Widmann, S. W. Pollaine, R. J. Wallace, G. Gregori, A. Holl, T. Bornath, R. Thiele, V. Schwarz, W. D. Kraeft, and R. Redmer. Observations of plasmons in warm dense matter. *Phys. Rev. Lett.*, **98**:065002, 2007.
- [206] S. H. Glenzer and R. Redmer. X-ray Thomson scattering in high energy density plasmas. *Rev. Mod. Phys.*, **81**:1625–1663, 2009.

- [207] A. V. Gurevich, L. V. Pariiskaya, and L. P. Pitaevskii. Self-Similar Motion of Rarefied Plasma. *Sov. Phys. JETP*, **22**:449–454, 1966.
- [208] P. Mora. Plasma expansion into a vacuum. *Phys. Rev. Lett.*, **90**:185002, 2003.
- [209] D. A. G. Deacon, L. R. Elias, J. M. J. Madey, G. J. Ramian, H. A. Schwettman, and T. I. Smith. First Operation of a Free-Electron Laser. *Phys. Rev. Lett.*, **38**:892–894, 1977.
- [210] Z. Huang and K.-J. Kim. Review of x-ray free-electron laser theory. *Physical Review Special Topics - Accelerators and Beams*, **10**:034801, 2007.
- [211] C. Pellegrini, A. Marinelli, and S. Reiche. The physics of x-ray free-electron lasers. *Rev. Mod. Phys.*, **88**:015006, 2016.
- [212] J. M. J. Madey. Stimulated Emission of Bremsstrahlung in a Periodic Magnetic Field. *J. Appl. Phys.*, **42**:1906–1913, 1971.
- [213] A. M. Kondratenko and E. L. Saldin. Generating of coherent radiation by a relativistic electron beam in an undulator. *Part. Accel.*, **10**:207–216, 1980.
- [214] R. Bonifacio, C. Pellegrini, and L. M. Narducci. Collective Instabilities and High-Gain Regime in a Free-Electron Laser. *Opt. Commun.*, **50**:373–378, 1984.
- [215] R. Bonifacio, L. De Salvo, P. Pierini, N. Piovella, and C. Pellegrini. Spectrum, temporal structure, and fluctuations in a high-gain free-electron laser starting from noise. *Phys. Rev. Lett.*, **73**:70–73, 1994.
- [216] A. Singer, F. Sorgenfrei, A. P. Mancuso, N. Gerasimova, O. M. Yefanov, J. Gulden, T. Gorniak, T. Senkbeil, A. Sakdinawat, Y. Liu, D. Attwood, S. Dziarzhytski, D. D. Mai, R. Treusch, E. Weckert, T. Salditt, A. Rosenhahn, W. Wurth, and I. A. Vartanyants. Spatial and temporal coherence properties of single free-electron laser pulses. *Opt. Express*, **20**:17480–17495, 2012.
- [217] W. Helml, A. R. Maier, W. Schweinberger, I. Grguraš, P. Radcliffe, G. Doumy, C. Roedig, J. Gagnon, M. Messerschmidt, S. Schorb, C. Bostedt, F. Grüner, L. F. DiMauro, D. Cubaynes, J. D. Bozek, T. Tschentscher, J. T. Costello, M. Meyer, R. Coffee, S. Düsterer, A. L. Cavalieri, and R. Kienberger. Measuring the temporal structure of few-femtosecond free-electron laser X-ray pulses directly in the time domain. *Nat. Photonics*, **8**:950–957, 2014.
- [218] E. Allaria, R. Appio, L. Badano, W. A. Barletta, S. Bassanese, S. G. Biedron, A. Borga, E. Busetto, D. Castronovo, P. Cinquegrana, S. Cleva, D. Cocco, M. Cornacchia, P. Craievich, I. Cudin, G. D’Auria, M. Dal Forno, M. B. Danailov, R. De Monte, G. De Ninno, P. Delgiusto, A. Demidovich, S. Di Mitri, B. Diviacco, A. Fabris,

- R. Fabris, W. Fawley, M. Ferianis, E. Ferrari, S. Ferry, et al. Highly coherent and stable pulses from the FERMI seeded free-electron laser in the extreme ultraviolet. *Nat. Photonics*, **6**:699–704, 2012.
- [219] L. Giannessi, E. Allaria, L. Badano, F. Bencivenga, C. Callegari, F. Capotondi, F. Cilento, P. Cinquegrana, M. Coreno, I. Cudin, G. D’Auria, M.B. Danailov, R. De Monte, G. De Ninno, P. Delgiusto, A.A. Demidovich, M. Di Fraia, S. Di Mitri, B. Diviacco, A. Fabris, R. Fabris, W.M. Fawley, M. Ferianis, P. Furlan Radivo, G. Gaio, D. Gauthier, F. Gelmetti, F. Iazzourene, S. Krecic, M. Lonza, et al. Status and Perspectives of the FERMI FEL Facility. *38th International Free Electron Laser Conference*, pages 19–23, 2018.
- [220] J. Amann, W. Berg, V. Blank, F.-J. Decker, Y. Ding, P. Emma, Y. Feng, J. Frisch, D. Fritz, J. Hastings, Z. Huang, J. Krzywinski, R. Lindberg, H. Loos, A. Lutman, H.-D. Nuhn, D. Ratner, J. Rzepiela, D. Shu, Y. Shvyd’ko, S. Spampinati, S. Stoupin, S. Terentyev, E. Trakhtenberg, D. Walz, J. Welch, J. Wu, A. Zholents, and D. Zhu. Demonstration of self-seeding in a hard-X-ray free-electron laser. *Nat. Photonics*, **6**: 693–698, 2012.
- [221] D. Ratner, R. Abela, J. Amann, C. Behrens, D. Bohler, G. Bouchard, C. Bostedt, M. Boyes, K. Chow, D. Cocco, F. J. Decker, Y. Ding, C. Eckman, P. Emma, D. Fairley, Y. Feng, C. Field, U. Flehsig, G. Gassner, J. Hastings, P. Heimann, Z. Huang, N. Kelez, J. Krzywinski, H. Loos, A. Lutman, A. Marinelli, G. Marcus, T. Maxwell, P. Montanez, et al. Experimental demonstration of a soft x-ray self-seeded free-electron laser. *Phys. Rev. Lett.*, **114**:054801, 2015.
- [222] C. Lechner, R. W. Assmann, J. Bödewadt, M. Dohlus, N. Ekanayake, B. Faatz, G. Feng, I. Hartl, A. Azima, and M. Drescher. Concept for a seeded fel at flash2. In *8th Int. Particle Accelerator Conf. (IPAC’17)*, pages 2607–2610, Copenhagen, Denmark, 2017.
- [223] P. Emma, R. Akre, J. Arthur, R. Bionta, C. Bostedt, J. Bozek, A. Brachmann, P. Bucksbaum, R. Coffee, F. J. Decker, Y. Ding, D. Dowell, S. Edstrom, A. Fisher, J. Frisch, S. Gilevich, J. Hastings, G. Hays, P. Hering, Z. Huang, R. Iverson, H. Loos, M. Messerschmidt, A. Miahnahri, S. Moeller, H. D. Nuhn, G. Pile, D. Ratner, J. Rzepiela, D. Schultz, et al. First lasing and operation of an ångstrom-wavelength free-electron laser. *Nat. Photonics*, **4**:641–647, 2010.
- [224] K. J. Kim and A. Sessler. Free-electron lasers: present status and future prospects. *Science*, **250**:88–93, 1990.
- [225] K. R. Ferguson, M. Bucher, J. D. Bozek, S. Carron, J. C. Castagna, R. Coffee, G. I. Curiel, M. Holmes, J. Krzywinski, M. Messerschmidt, M. Minitti, A. Mitra, S. Moeller, P. Noonan, T. Osipov, S. Schorb, M. Swiggers, A. Wallace, J. Yin, and

- C. Bostedt. The Atomic, Molecular and Optical Science instrument at the Linac Coherent Light Source. *J. Synchrotron Radiat.*, **22**:492–497, 2015.
- [226] N. Hartmann, W. Helml, A. Galler, M. R. Bionta, J. Grünert, S. L. Molodtsov, K. R. Ferguson, S. Schorb, M. L. Swiggers, S. Carron, C. Bostedt, J. C. Castagna, J. Bozek, J. M. Glownia, D. J. Kane, A. R. Fry, W. E. White, C. P. Hauri, T. Feurer, and R. N. Coffee. Sub-femtosecond precision measurement of relative X-ray arrival time for free-electron lasers. *Nat. Photonics*, **8**:706–709, 2014.
- [227] S. Schorb, T. Gorkhover, J. P. Cryan, J. M. Glownia, M. R. Bionta, R. N. Coffee, B. Erk, R. Boll, C. Schmidt, D. Rolles, A. Rudenko, A. Rouzee, M. Swiggers, S. Carron, J. C. Castagna, J. D. Bozek, M. Messerschmidt, W. F. Schlotter, and C. Bostedt. X-ray–optical cross-correlator for gas-phase experiments at the Linac Coherent Light Source free-electron laser. *Appl. Phys. Lett.*, **100**:121107, 2012.
- [228] L. Strüder, U. Briel, K. Dennerl, R. Hartmann, E. Kendziorra, N. Meidinger, E. Pfeffermann, C. Reppin, B. Aschenbach, W. Bornemann, H. Bräuninger, W. Burkert, M. Elender, M. Freyberg, F. Haberl, G. Hartner, F. Heuschmann, H. Hippmann, E. Kastelic, S. Kemmer, G. Kettenring, W. Kink, N. Krause, S. Müller, A. Oppitz, W. Pietsch, M. Popp, P. Predehl, A. Read, K. H. Stephan, et al. The European Photon Imaging Camera on XMM-Newton: The pn-CCD camera. *Astron. Astrophys.*, **365**:L18–L26, 2001.
- [229] S. Link and M. A. El-Sayed. Shape and size dependence of radiative, non-radiative and photothermal properties of gold nanocrystals. *Int. Rev. Phys. Chem.*, **19**:409–453, 2000.
- [230] G. Mie. Beiträge zur Optik trüber Medien, speziell kolloidaler Metallösungen. *Annalen der Physik*, **330**:377–445, 1908.
- [231] F. Lücking, A. Trabattoni, S. Anumula, G. Sansone, F. Calegari, M. Nisoli, T. Oksenhendler, and G. Tempea. In situ measurement of nonlinear carrier-envelope phase changes in hollow fiber compression. *Opt. Lett.*, **39**:2302–2305, 2014.
- [232] I. J. Sola, E. Mével, L. Elouga, E. Constant, V. Strelkov, L. Poletto, P. Villoresi, E. Benedetti, J. P. Caumes, S. Stagira, C. Vozzi, G. Sansone, and M. Nisoli. Controlling attosecond electron dynamics by phase-stabilized polarization gating. *Nat. Phys.*, **2**:319–322, 2006.
- [233] A. T. J. B. Eppink and D. H. Parker. Velocity map imaging of ions and electrons using electrostatic lenses: Application in photoelectron and photofragment ion imaging of molecular oxygen. *Rev. Sci. Instrum.*, **68**:3477–3484, 1997.

- [234] Q. Liu, L. Seiffert, A. Trabattoni, M. C. Castrovilli, M. Galli, P. Rupp, F. Frassetto, L. Poletto, M. Nisoli, E. Rühl, F. Krausz, T. Fennel, S. Zherebtsov, F. Calegari, and M. F. Kling. Attosecond streaking metrology with isolated nanotargets. *J. Opt.*, **20**:024002, 2018.
- [235] J. R. Cash and A. H. Karp. A variable order Runge-Kutta method for initial value problems with rapidly varying right-hand sides. *ACM Transactions on Mathematical Software*, **16**:201–222, 1990.
- [236] C. Runge. Ueber die numerische Auflösung von Differentialgleichungen. *Mathematische Annalen*, **46**:167–178, 1895.
- [237] W. Kutta. Beitrag zur näherungsweise Integration totaler Differentialgleichungen. *Z. Math. Phys.*, **46**:435–453, 1901.
- [238] D. A. Verner, G. J. Ferland, K. T. Korista, and D. G. Yakovlev. Atomic Data for Astrophysics. II. New Analytic FITS for Photoionization Cross Sections of Atoms and Ions. *Astrophys. J.*, **465**:487, 1996.
- [239] J. Mauritsson, M. B. Gaarde, and K. J. Schafer. Accessing properties of electron wave packets generated by attosecond pulse trains through time-dependent calculations. *Phys. Rev. A*, **72**, 2005.
- [240] C. Palatchi, J. M. Dahlström, A. S. Kheifets, I. A. Ivanov, D. M. Canaday, P. Agostini, and L. F. DiMauro. Atomic delay in helium, neon, argon and krypton. *J. Phys. B: At., Mol. Opt. Phys.*, **47**:245003, 2014.
- [241] N. Sakamoto, H. Tsuchida, and T. Kato. Oscillator strength spectra and related quantities of 9 atoms and 23 molecules over the entire energy region. Technical report, National Inst. for Fusion Science, 2010.
- [242] J. Berkowitz. *Atomic and molecular photoabsorption: absolute total cross sections*. Academic Press, 2002.
- [243] S. Neppl, R. Ernstorfer, A. L. Cavalieri, C. Lemell, G. Wachter, E. Magerl, E. M. Bothschafter, M. Jobst, M. Hofstetter, U. Kleineberg, J. V. Barth, D. Menzel, J. Burgdörfer, P. Feulner, F. Krausz, and R. Kienberger. Direct observation of electron propagation and dielectric screening on the atomic length scale. *Nature*, **517**:342–346, 2015.
- [244] C. Cirelli, M. Sabbar, S. Heuser, R. Boge, M. Lucchini, L. Gallmann, and U. Keller. Energy-Dependent Photoemission Time Delays of Noble Gas Atoms Using Coincidence Attosecond Streaking. *IEEE J. Sel. Top. Quantum Electron.*, **21**:1–7, 2015.

- [245] M. Y. Amusia and J. P. Connerade. The theory of collective motion probed by light. *Rep. Prog. Phys.*, **63**:41–70, 2000.
- [246] G. Wachter, S. Nagele, S. A. Sato, R. Pazourek, M. Wais, C. Lemell, X.-M. Tong, K. Yabana, and J. Burgdörfer. Protocol for observing molecular dipole excitations by attosecond self-streaking. *Phys. Rev. A*, **92**:061403, 2015.
- [247] A. S. Baltenkov, S. T. Manson, and A. Z. Msezane. Jellium model potentials for the C₆₀ molecule and the photoionization of endohedral atoms, A@C₆₀. *J. Phys. B: At., Mol. Opt. Phys.*, **48**:185103, 2015.
- [248] M. I. Stockman, M. F. Kling, U. Kleineberg, and F. Krausz. Attosecond nanoplasmonic-field microscope. *Nat. Photonics*, **1**:539–544, 2007.
- [249] J. Schötz, B. Förg, M. Förster, W. A. Okell, M. I. Stockman, F. Krausz, P. Hommelhoff, and M. F. Kling. Reconstruction of Nanoscale Near Fields by Attosecond Streaking. *IEEE J. Sel. Top. Quantum Electron.*, **23**:8700111, 2017.
- [250] E. Lorek, E. Marsell, A. Losquin, M. Miranda, A. Harth, C. Guo, R. Svard, C. L. Arnold, A. L’Huillier, A. Mikkelsen, and J. Mauritsson. Size and shape dependent few-cycle near-field dynamics of bowtie nanoantennas. *Opt. Express*, **23**:31460–31471, 2015.
- [251] R. S. Judson and H. Rabitz. Teaching lasers to control molecules. *Phys. Rev. Lett.*, **68**:1500–1503, 1992.
- [252] A. Assion, T. Baumert, M. Bergt, T. Brixner, B. Kiefer, V. Seyfried, M. Strehle, and G. Gerber. Control of Chemical Reactions by Feedback-Optimized Phase-Shaped Femtosecond Laser Pulses. *Science*, **282**:919–922, 1998.
- [253] T. Brixner and G. Gerber. Quantum control of gas-phase and liquid-phase femtochemistry. *ChemPhysChem*, **4**:418–438, 2003.
- [254] C. Daniel, J. Full, L. González, C. Lupulescu, J. Manz, A. Merli, S. Vajda, and L. Wöste. Deciphering the reaction dynamics underlying optimal control laser fields. *Science*, **299**:536–539, 2003.
- [255] F. Kelkensberg, W. Siu, J. F. Pérez-Torres, F. Morales, G. Gademann, A. Rouzée, P. Johnsson, M. Lucchini, F. Calegari, J. L. Sanz-Vicario, F. Martín, and M. J. J. Vrakking. Attosecond Control in Photoionization of Hydrogen Molecules. *Phys. Rev. Lett.*, **107**:043002, 2011.
- [256] M. Schultze, E. M. Bothschafter, A. Sommer, S. Holzner, W. Schweinberger, M. Fiess, M. Hofstetter, R. Kienberger, V. Apalkov, V. S. Yakovlev, M. I. Stockman, and F. Krausz. Controlling dielectrics with the electric field of light. *Nature*, **493**:75–78, 2013.

-
- [257] A. Sommer, E. M. Bothschafter, S. A. Sato, C. Jakubeit, T. Latka, O. Razskazovskaya, H. Fattahi, M. Jobst, W. Schweinberger, V. Shirvanyan, V. S. Yakovlev, R. Kienberger, K. Yabana, N. Karpowicz, M. Schultze, and F. Krausz. Attosecond nonlinear polarization and light-matter energy transfer in solids. *Nature*, **534**:86–90, 2016.

List of Figures

2.1	Temporal evolution of the electric field of a few-cycle laser pulse	8
2.2	Illustration of possible ionization mechanisms in strong-field regime	9
2.3	Three step model	10
2.4	RABBITT and attoclock	13
2.5	Electron scattering, Coulomb-laser coupling and EWS-delay	15
2.6	Theoretical delays in atomic hydrogen	16
2.7	Radial potential of C ₆₀ in LDA with ground state energy levels and imaginary part of polarizability	20
3.1	Experimental setup of reaction nanoscope	24
3.2	Electrostatic potentials in the spectrometer calculated by SIMION	25
3.3	Experimental Calibration of channeltron	28
3.4	Experimental histogram of channeltron signal and TOF spectrum	30
3.5	Comparison of measured and simulated angular proton distributions	31
3.6	Simulated electron statistics and expected channeltron histogram from M ³ C simulations	33
3.7	Analysis of proton and electron trajectories in numerical calculations	35
3.8	Simulated delay-dependent dissociation yields on the nanoparticle surface with final proton momentum distribution	37
3.9	Illustration of the working principle of the inversion method	40
3.10	Fitting of dissociation yield to experimental data by the inversion method .	41
4.1	Expansion of plasma illustrated by changes in time-dependent radial density profile	45
4.2	Elastically scattered light for a set of fit parameters r_c and d determining the electron density function	46
4.3	Experimental setup of plasma imaging experiment at LCLS	48
4.4	Analysis of experimental scattering images	50
5.1	Experimental setup for C ₆₀ streaking	54
5.2	XUV spectrum and electron spectra of C ₆₀ and neon to show experimental conditions in interaction region	55
5.3	Spectrograms of neon and C ₆₀ and exemplary contour lines with fit functions	57
5.4	Experimental streaking delays	59

5.5	Simulated streaking delay of neon under simplified conditions	61
5.6	Simulated effect of XUV spectrum on neon delay.	62
5.7	Dipolar electric field distribution around C ₆₀ molecule	63
5.8	Ionization properties of neon	65
5.9	Ionization properties of C ₆₀	67
5.10	Simulated effect of XUV chirp	68
5.11	Simulated C ₆₀ streaking	69
5.12	Influence of induced dipole on streaking delay	70
5.13	Final comparison of C ₆₀ streaking delay between experiment and theory . .	72
A.1	Simulated spectrometer resolution	78
A.2	TEM images of silica nanoparticles	79
A.3	Inversion method for exemplary charge distribution	80
A.4	Scattering image of nanoparticle cluster	81
A.5	Linear extrapolation of delays in neon streaking simulations	82

List of Tables

2.1	General characteristic parameters of C_{60}	19
5.1	Fit parameters of Fermi fit to C_{60} dipole field	65
A.1	Fit parameters of inversion method	80
A.2	Parameters for neon photoionization cross section	82

Acknowledgements

First of all, I would like to thank **Prof. Dr. Matthias Kling** for his excellent mentoring of my dissertation and the corresponding projects. His constant support not only in the project management but also with daily routine concerns around the experimental setup deserves special appreciation. I am also extremely grateful for his prompt and constructive corrections of the manuscript. He is not only an outstanding physicist and researcher but also the perfect host of many entertaining Christmas parties and a reliable participant of exciting skiing excursions and running events. I am more than happy to have the opportunity to work with such a great mentor like him.

I wish to show my deep appreciation to **Prof. Dr. Ferenc Krausz** who gave me the opportunity to work in the group as a PhD student.

I would like to express my special thanks to **Prof. Dr. Francesca Calegari** for sharing her working experience in the field of attosecond physics. From the very beginning of our collaboration, she constantly provided both practical and intellectual assistance. During every single campaign at the Politecnico in Milan she gave us a warm welcome in the lab and introduced me to the “whole world of attosecond streaking”. I gladly think back to Italian pizza, lunch at the cafeteria and challenging vacuum pump complications.

In this context, also many thanks to **Prof. Dr. Mauro Nisoli** for hosting us in his laboratory in Milan. Additionally, I wish to thank the “Milan Crew”, namely **Dr. Andrea Trabattoni**, **Mara Galli**, **Vincent Wanie** and **Dr. Erik Månsson** for the excellent support during the measurements and for including me to their regular after-lunch espresso/gelato breaks.

I am highly grateful to **Prof Dr. Thomas Fennel** from the Institute of Physics of the University of Rostock for many fruitful discussions during our collaboration comprising various nanoparticle projects with corresponding publications and beam times at free-electron laser facilities. His helpful comments and new ideas always improved our corporate manuscripts.

Sincere thanks to **Dr. Lennart Seiffert** and **Dr. Christian Peltz** for steadily complementing my work with their theoretical calculations, teaching me the secrets of numerical simulations and shortening the time of long night shifts during beam times at LCLS in Stanford and FLASH in Hamburg.

I also wish to thank **Prof. Dr. Eckart Rühl**, **Dr. Egill Antonsson**, **Ina Halfpap** and **Dr. Burkhard Langer** from the FU Berlin for providing the expertise on the nanoparticle source and contributing to the corresponding publications.

Special thanks **Dr. Markus Gallei**, **Dr. Christian Schäfer** and **Annika Schlan-**

der from the TU Darmstadt for producing one of the essentials of this thesis: billions of beautiful well-shaped nanoparticles ready to be investigated.

I highly value the productive collaboration with **Prof. Dr. Artem Rudenko**, **Dr. Jeff Powell** and **Adam Summers** from the James R. Macdonald Laboratory at the Kansas State University in Manhattan.

I greatly acknowledge the work and commitment of the beam scientists at LCLS, **Dr. Timur Osipov** and **Dr. Dipanwita Ray**, and at FLASH, **Dr. Benjamin Erk**, **Dr. Dimitrios Rompotis**, **Dr. Cédric Bomme** and **Dr. Christopher Passow**, who were available 24/7 during the measurements and patiently found solutions for unexpected problems with the setup.

Since no experimental result is meaningful without the proper backup from theory, I am very thankful for the support of **Prof. Dr. Himadri Chakraborty** and **Prof. Dr. Maia Magrakvelidze**.

Cordial thanks to **Prof. Dr. Cosmin Blaga** from the Ohio State University, **Prof. Dr. Markus Raschke** from the University of Colorado, Boulder, and **Prof. Dr. Ali Alnaser** from the American University of Sharjah for their contributions to joint projects and manuscripts.

I am very grateful to **Dr. Boris Bergues** not only for his extensive supervision of the experiments and publications but also for his patient revisions of this thesis. Despite the long distance to his present workplace in Canada and the corresponding time shift, he regularly managed to give valuable input by phone.

I would like to thank my longtime office mate **Dr. Christian Burger** who was a constant guarantee for a pleasant working atmosphere at the LMU. He helped with numerous experiments and spent hours discussing the most recent measurement results with me. Furthermore, he taught me how to grow air-filtering moss walls, gave me lessons in appropriate dremel usage and refurbished our office with a collection of lab snacks boxes. It is particularly worth mentioning that he once gave me a ride to our institute by rubber boat.

Many thanks to **Dr. Matthias Kübel**, **Dr. Nora Kling**, **Philipp Rosenberger**, **Thomas Weatherby** and **Sambit Mitra** who played an important role in the development of the nanoTRIMS setup.

I really enjoyed the unique time with my fellow PhD candidates and colleagues at the MPQ and LMU whom I would like to say “thank you”: **Dr. Sergey Zherebtsov**, **Johannes Schötz**, **Dr. Benjamin Förg**, **Johannes Stierle**, **Qingcao (Max) Liu**, **Dr. Pawel Wnuk**, **Dr. Hui Li**, **Dr. Shaohua Sun**, **Marcel Neuhaus**, **Dr. Frederik Süßmann**, **Dr. Harald Fuest**, **Dr. Shubhadeep Biswas**, **Maximilian Seeger**, **Dr. Tobias Saule**, **Stephan Heinrich**, **Maximilian Högner**, **Christina Hofer**, **Dominik Ehberger**, **Sonja Tauchert**, **Johannes Thurner** and **Kathrin Mohler**.

Further acknowledgements go to **Monika Wild** and **Klaus Franke** for the great organization of many events and formalities.

I owe **Rolf Oehm**, **Michael Rogg** and their whole teams a great debt of gratitude

for their prompt and reliable production of many components and equipment which were indispensable for my experiments.

I am extremely thankful to my **whole family** and **all my friends** for advocating the start of this thesis, for their constant encouragement and their great advice during any imaginable circumstances. Without their remarkable support, neither the studies of physics nor the subsequent dissertation would have been possible.

Last but not least, I would like to express my deepest gratitude to **Marie Franziska Sommer** for her continuous support during the last years. Without her trust in my work, her encouragement after setbacks, her patience with a grumpy PhD student and her proof-reading of the thesis I wouldn't have been able to do this.